AN ABSTRACT OF THE THESIS OF

Thomas Charles Lippmann for the degree of Doctor of Philosophy

in Oceanography presented on September 9, 1992

Title: Edge Wave Response to a Modulating Incident Wave Field

Abstract Approved: Redacted for privacy

Robert A. Holman

Modulations in wave height of oceanic sea and swell cause momentum transfer to the water column at group (infragravity) time and space scales, on the order of 10^2-10^3 s and 10^2-10^3 m. In the surf zone, this momentum flux arises principally through dissipation of incident wave energy by breaking. In this thesis, the generation of low frequency waves by the spatial and temporal modulations of breaking incident waves is addressed first, followed by field estimates of the time and space scales of wave breaking distributions. Lastly, nearshore sand bar behavior, linked theoretically to infragravity waves, is investigated over a five year period.

A theoretical forcing mechanism for driving resonant, longshore progressive edge waves is derived from the momentum equations. Forcing within the surf zone is examined through group scale modulations in incident wave dissipation by depth-limited breaking. The nonlinear forcing, provided by the unbalanced temporal variations in radiation stress gradients, is shown to be comparable to previous offshore forcing theory. Initial surf zone growth rates are predicted and found to be rapid, with edge wave amplitudes growing to the size of the incident waves on the order of 10-20 edge wave periods (much faster than other model predictions). However, in nature these

rates will be reduced by the stochastic behavior of real ocean waves. Finally, the total forcing (including surf zone and offshore contributions) introduces structure into the infragravity band of the forcing spectrum, providing an additional frequency selection mechanism necessary for the generation of nearshore sand bars.

The time and space scales of wave breaking across a naturally barred beach are estimated. Field data are obtained on narrow banded (in both frequency and direction) day during the DELILAH experiment. Integral to this work is a new video based sampling technique, which is shown to quantify the modulation scales of wave breaking distributions. The technique is based on the contrast between the lighter intensity of foam and bubbles of actively breaking waves and bores, and the darker unbroken surrounding water. Video image time series are compared with fixed surf zone arrays of sea surface elevation and bi-directional current.

Principal results indicate that the important breaking processes, in terms of temporal and spatial phase, can be quantified. At incident frequencies, the phase speed and incidence angle of breaking waves are in good agreement with *in situ* instrumentation. At lower frequencies, breaking wave distributions seaward of the bar crest are associated with wave groups progressing landward at the group velocity. Analysis of longshore length scales indicate group forcing to be broad-banded across frequency-wavenumber space. Interestingly, no coherence was found between group forcing and the infragravity free wave response, suggesting that the nearshore is a high Q (resonant) system.

Edge Wave Response to a Modulating Incident Wave Field

by

Thomas Charles Lippmann

A THESIS

submitted to

Oregon State University

in partial fulfillment of
the requirements for
the degree of

Doctor of Philosophy

Completed September 9, 1992

Commencement June 1993

APPROVED:

Redacted for privacy

Professor of Oceanography in charge of major

Redacted for privacy

Dean of College of Oceanography

Redacted for privacy

Dean of Graduate School

Date thesis is presented September 9, 1992

Typed by Thomas C. Lippmann

ACKNOWLEDGEMENTS

It has been an honor and a privilege to have been educated under the guidance of "Your Humble Servant", Rob Holman. He has unselfishly (and relentlessly) shared with me his insight into the fundamentals and innovations of nearshore science, provided funding and enthusiastic support, and presented me with countless opportunities to explore many research venues, both theoretically and experimentally. It has without a doubt been an exciting and fun seven years riding on his coattails. I will be forever in his debt.

I am also indebted to the many other people who have contributed to all phases of this research. These include the staff at the FRF for providing unlimited support for field work, most notably Bill Birkemeier and Kent Hathaway. Ed Thornton, Bob Guza, Steve Elgar, Tony Bowen, Peter Howd, Dick Sternberg, Abby Sallenger, Reggie Beach, and Joan Oltman-Shay have all generously shared data, resources, wisdom, and most importantly their time. I also thank my committee for giving their valuable time and effort in overseeing my research program: Rob, Joan, Paul Komar, Chuck Sollitt, Dudley Chelton, and Peter Bottomley. Acknowledgement is extended to Richard Farris for first revealing to me the possibilities of life as a scientist. This work was supported by the Office of Naval Research, Coastal Sciences program, and the Army Corps of Engineers Barrier Island Sedimentation work unit.

I have also benefited tremendously from the friendships and support of the many individuals with whom have made my stay in Corvallis a memorable experience. In particular, endless enthusiasm has come from fellow students Mark Lorang, Pete Howd, Todd Holland, Terri Hagelberg, Leigh Welling, Jim McManus, Diane Foster, Lynn Berkery, Ming Shih, John Marra, and C. Valenti. Outstanding byte-swapping, number-crunching, screen-popping computer support was provided by Paul O'Neill, Chuck Sears, Tom Leach, Mark Johnston, and John Stanley. Thanks to Marcia Turnbull for making my research life much simpler, and for making the workplace an enjoyable place to be.

Thanks: To Bruce Appelgate for many Buffet-wrenching hours of trivia, wit, news reports, and doing San Francisco the right way. To the Deschutes river and fishing animals Bruce F., Terry, Bob, Margaret and Dan , Todd T., Mark, Peter, Dave, and Todd H. To my golfing, skiing, crabbing, running, and mountain biking fools Fish, Upper Lip, Bec, Free, Shoe, Mark, Shaf, Tadman, and the Grimmace. To my many

AGU and e-mail buddies that have spent many hours reading my sometimes pointless letters, most frequently Bruce, Michele, Peter, Andrea, Diane, Kimball, Doug, Brian, and Britt (note: this sentence was typed with only two fingers). To Mary Jo for an unforgettable mindwalk through some wild scenery. And to Diane for lobsters, thumbs, and sympathetic wanderings, and for showing me signs of life I hadn't seen as clearly before. Finally, a special geowd to my beer-drinkin', cuban-smokin', bear-chasin', tree-plantin', philosophizin', beach-talkin', ball-chasin', stick-retrievin', birdie-chasin', fishin' buddies: Mark and Ebony.

The principal engineer for this work was the late Paul Vincent O'Neill. Without his efforts this work would not have been possible. Through his wisdom and friendship I am a better person today, thus it is with great sadness that I am unable to express my gratitude to him for sharing a small part his life with me.

Finally, I would also like to extend my deepest felt gratitude and love to my family for supporting me throughout all aspects of my life. Mike has always been someone to whom I have looked up to, who has taught me more than he will ever know, and has given me someone to whom I can be proud to be called a brother. Becky has shared with me many unique experiences, endearing memories, and has shown me what it means to have a wonderful sister. Without exception the person who has helped me the most has been my mother, Sondra Jane. Without her unconditional love and support I would not be where I am today. She is as true a friend as anyone could ever have. This dissertation is dedicated to them, for they make up the best part of who I am.

TABLE OF CONTENTS

LIST OF FIGURES

LIST OF TABLES

EDGE WAVE RESPONSE TO A MODULATING INCIDENT WAVE FIELD

GENERAL INTRODUCTION

Understanding the physical processes that govern sediment transport on beaches is a primary goal of nearshore researchers worldwide. One aspect of the problem that has received considerable emphasis has been the behavior and evolution of large scale topography, most commonly sand bars. Sand bars are ubiquitous features of nearshore environments, and are important to the total sediment budget since they contain a large volume (reservoir) of sand. Since they can be very dynamic, sand bar behavior is a first order approximation of large movements of beach material, particularly in terms of net transport and erosional or accretional exchange of sediment between the beach face and offshore.

Leading theories suggest that large scale morphologic response is either determined by mean flows associated with incident waves (Dhyr-Nielsen and Sorensen, 1970; Dally and Dean, 1984), or to wave motions with similar spatial scales, such as infragravity edge waves, low frequency motions O(30-300 secs) (Bowen and Inman, 1971; Holman and Bowen, 1982). These sometimes competing models have both met with only limited support from field data (Holman and Sallenger, 1992), largely due to the inherent difficulty in adequately sampling both the fluid and sediment fields simultaneously.

The nearshore problem is complicated, particularly when considering that the fundamentals of sediment transport are explicitly linked to the fluid motion, which in turn is dependent on the topography. This nonlinear interaction between fluid motion

and topography occurs on many time scales, from very high frequency turbulence to mean flows. In recent years, the importance of low frequency motions in controlling beach behavior has become increasingly apparent.

The impetus for the focus on the infragravity band is primarily from two distinct observations. The first is that the dominant spatial scale of major topographical features of beach bathymetry (*i.e.* sand bars) is very large, $O(10^2\text{-}10^3$ m), much greater than scales of typical oceanic sea and swell with spatial scales $O(10^1$ m) (Bowen and Inman, 1971). However, low frequency infragravity waves have very large spatial scales, on the same order of magnitude as naturally occurring sand bars (*e.g.* Holman and Bowen, 1982; Oltman-Shay and Guza, 1987), and have the added benefits of providing a mechanism for generating alongshore periodicities that also match observed morphologic length scales found in nature (Bowen and Inman, 1971; Lippmann and Holman, 1989a).

The second observation is that during high energy storms, when sediment movement is greatest and the most dramatic changes to the beach occur, the power spectra in the inner surf zone (of sea surface elevation and current velocity) and on the beach face (swash motions) is often dominated by the infragravity band (Thornton and Guza, 1982; Sallenger and Holman, 1987). This is not entirely surprising considering that in shallow water incident wave energy is severely limited by breaking. Infragravity waves, with long length scales compared to their amplitudes, stand against the shoreline and therefore do not dissipate energy by breaking. Moreover, infragravity energy in the inner surf zone increases as incoming incident energy increases (*e.g* Thornton and Guza, 1982); that is, energy is transferred nonlinearly through wave shoaling and breaking from sea and swell to lower infragravity frequencies. Thus the first order (linear) effect of increasing offshore sea and swell energy is to increase the surf zone width (bigger

waves simply break further offshore), and hence the principal manifestation of large incoming sea swell is energetic infragravity motions in the inner surf zone and swash.

Field data from the surf zone has convincingly shown the infragravity band to be predominately associated with edge and leaky waves (Bowen and Guza, 1978; Huntley, *et al.*, 1981; Guza and Thornton, 1985; Oltman-Shay and Guza, 1987; Huntley, 1988), although energy at very low frequencies may be due to shear instabilities of the longshore current (Bowen and Holman, 1989; Oltman-Shay, *et al.*, 1989; Howd, *et al.*, 1991). Edge waves are the normal mode solutions of free surface gravity waves in shallow water on a sloping bed (Eckart, 1951). The shoreline acts as a wave guide, where edge wave modes are trapped by refraction since phase speeds are dependent on local depth ($c = \sqrt{gh}$). Leaky waves are those waves that escape the nearshore (*i.e.* propagate into deep water). Very low frequency motions associated with shear instabilities, have celerities that are too slow to be surface gravity waves, and are thus easily distinguished from edge and leaky waves by their frequency-wavenumber dispersion relation.

Despite the growing evidence for the existence of edge waves, the principal forcing mechanism remains unknown, largely due to difficulties in sampling the wave field over large enough spatial scales to both adequately measure the forcing and response simultaneously. Leading theories suggest that edge waves result from either the nonlinear interactions of offshore wind waves (Gallagher, 1971; Bowen and Guza, 1978), or from direct forcing by the time dependent gradients in radiation stresses induced by modulating break point amplitudes (Symonds, et al., 1982; Symonds and Bowen, 1984; Schaffer, 1990).

Field evidence supporting a link between incident and low frequency waves has been limited. In the analysis of Elgar and Guza (1985a), cross-bispectral observations (from field data) between pressure spectra obtained across the width of the surf zone and

shoreline runup showed that nonlinear coupling between surf beat and incident waves increased towards the shore, and further that cross-biphases were consistent with waves which were not phase-locked to the wave groups. More recently, Okihiro, *et al.* (1992) and Elgar, *et al.* (1992) showed that low frequency waves in intermediate water depths were coupled to incident frequencies, providing evidence for nonlinearly generated bound waves phase-locked to wave groups.

Until now, data needed to adequately test, or even address, the surf zone models (*i.e.*, Symonds, *et al.*, 1982) have not existed. The lack of appropriate data stems from the inherent difficulty in measuring time series of break point position over the large spatial scales associated with wide surf zones, sand bars and edge waves. Not surprisingly, previous field measurements of the spatial scales associated with the breaking process have been limited to visual observations in which quantification has been difficult. Some investigators have devised methods by which the breaking waves in a time series record of sea surface elevation are flagged manually for the passing of a breaking wave or bore, allowing for statistical representations of the breaking processes as a function of cross-shore distance (*e.g.* Thornton and Guza, 1983). This data is useful, for example, in describing the potential energy decay of progressive incident waves across the surf zone. However, data collection requires tremendous logistical effort to adequately sample three-dimensional processes.

Lippmann and Holman (1989b) made similar observations utilizing video recordings to identify breaking waves in colocated sea surface elevation time series. Remote sensing techniques are not constrained by surf zone conditions and thus avoid the potential destruction due to wave forces. They also allow for sampling at numerous locations simultaneously over the large spatial scales of natural surf zones.

This thesis has three primary objectives. The first is to formulate the resonant forcing for infragravity edge waves from contributions in the surf zone through temporal

and spatial modulations in break point amplitudes. In Chapter 1, a theoretical model is presented for the initial growth rate of resonant edge waves based on the interaction radiation stress induced by a modulating incident wave field. Comparisons are made with forcing contributions in the offshore region (outside the surf zone) arising from the nonlinear difference interaction of two beating incident waves (essentially the mechanism of Gallagher, 1971).

The second objective is to quantify the temporal and spatial scales of incident wave dissipation in the field, and subsequently compare the forcing modulations with the response in the flow field. Time and space scales of interest are on the order of wave groups, since modulations on these scales potentially give rise to infragravity waves. In Chapter 2, a new technique (based on video image processing) is developed for quantifying the incident band time and space scales of surf zone wave breaking. This work demonstrates the powerful ability of video methods for sampling the phase relationships of breaking waves in the surf zone. In Chapter 3, low frequency modulations in wave breaking patterns are estimated and compared with the infragravity band response observed in the flow field of the inner surf zone and swash.

And finally in Chapter 4, the behavior of a double sand bar system over a five year period is investigated. This work is a continuation of our previous research (Lippmann and Holman, 1990), in which the climatological behavior of sand bars are observed over long time scales, on the order of a few years. The influence of the presence or absence of an outer bar on the behavior of the dynamic inner bar is assessed. Episodic transitions from one-to-two bar configuration are compared with the occurrence of very large storms.

The data used in the Chapters 2 and 3 were collected as part of the DELILAH nearshore processes experiment held at the U.S. Army Corps of Engineers Field Research Facility located on the Outer Banks of North Carolina, near the village of

Duck, in October, 1990. Data from Chapter 4 were also collected at the Duck beach, and consists of daily video derived estimates of bar position and shape obtained from 1986-1991. Chapter 2 has been published in the Proceedings of the Coastal Sediments '91 Specialty Conference (ASCE, pp. 542-556). This and all other chapters will be co-authored by R. A. Holman. Chapter 4 will appear later this year in the Journal of Coastal Research as part of a Special Issue on Beach and Surf Zone Morphodynamics, with K. Hathaway (of the FRF) as co-author. Chapters 1 (with A. J. Bowen of Dalhousie University) and 3 will be submitted for publication in the Journal of Geophysical Research.

CHAPTER 2

Resonant Forcing of Infragravity Edge Waves by Modulations in Break Point Amplitudes

ABSTRACT

A theoretical surf zone mechanism for driving resonant longshore progressive surface gravity waves in the nearshore (edge waves) by a modulating incident wave field is derived from the linearized, shallow water momentum equations for the case of a plane sloping bed. Resonant edge wave forcing is formulated in the surf zone by the time and space dependent modulations in break point positions. Comparisons are made with forcing in the offshore region (outside the surf zone) from the nonlinear interaction of two incident waves (essentially the mechanism of Gallagher, 1971). The nonlinear forcing is provided by the unbalanced temporal variations in radiation stress gradients, $\partial^2 S_{\alpha\beta}/\partial\alpha\partial\beta$. Following Phillips (1977) a general form for the radiation stress due to the difference interaction of two shallow water incident waves (modeled after Stoker, 1947) approaching the beach at some angle to the normal is derived. Using this formulation of the forcing we find that the cross-shore component of onshore directed momentum flux, $\partial^2 S_{xx}/\partial x^2$, dominates over longshore directed fluxes, $2\partial^2 S_{xy}/\partial x\partial y$ and $\partial^2 S_{yy}/\partial y^2$, particularly for small angles of incidence and higher edge wave modes.

The strength of the surf zone generation mechanism is found to be comparable to offshore forcing proposed by Gallagher (1971), who intentionally excluded forcing due to breaking phenomena. Here we show that the surf zone component of the forcing can not be neglected, and under the right conditions can actually dominate. Initial growth rates are predicted and found to be quite rapid, with edge waves amplitudes growing to incident wave amplitudes on the order of 10-20 edge wave periods, much faster than other model predictions (*e.g.*, Foda and Mei, 1981). However in nature the stochastic behavior of real ocean waves will reduce these rates by an unknown amount. In addition, the total forcing mechanism including both offshore and surf zone contributions introduces structure into the infragravity band of the forcing spectra, and with restrictions introduced by discrete resonances of the system, provides a second frequency selection mechanism.

INTRODUCTION

Since the initial observations of Munk (1949) and Tucker (1950) much effort has been aimed at understanding the origin and importance of low frequency (relative to wind waves) surface gravity waves in intermediate and shallow water. Field data obtained on natural beaches have shown that long period ($O(10^2\text{-}10^3$ sec)) infragravity motions often dominate power spectra in the inner surf zone and swash, particularly during storms (Huntley, 1976; Huntley, *et al*, 1981; Holman, 1981; Thornton and Guza, 1982; Holman and Sallenger, 1985; Sallenger and Holman, 1987; and others). These observations are not entirely surprising, especially when considering that incident wave heights in shallow water are severely limited by breaking (*e.g.*, Thornton and Guza, 1982).

Moreover, the data indicates that infragravity energy in the surf zone is predominantly derived from edge waves (longshore progressive surface gravity waves trapped to the shoreline by refraction) and leaky modes (waves which escape the nearshore to deep water) (Suhayda, 1974; Bowen and Guza, 1978; Katoh, 1981; Huntley, *et al.*, 1981; Guza and Thornton, 1985; Elgar and Guza, 1985; Oltman-Shay and Guza, 1987; and others), although some low frequency energy may be due to bound waves (Guza, *et al.*, 1984; List, 1991, 1992) or instabilities of the longshore current called shear waves (Bowen and Holman, 1989; Oltman-Shay, *et al.*, 1989; Dodd and Thornton, 1990; Howd, *et al.*, 1991; Dodd, *et al.*, 1992).

The potential importance of the infragravity band to nearshore sediment dynamics has become increasingly apparent in recent years, partly due to the correspondence of typical nearshore morphologic length scales ($O(10^2\text{-}10^3$ m) and infragravity wave scaling (Bowen and Inman, 1971; Wright and Short, 1984; Lippmann and Holman, 1990; Holman and Sallenger, 1992; and others). Simple models, based on edge wave dynamics, exist for the generation of linear (Bowen, 1980), rhythmic (Bowen and Inman,

1971), and more complicated morphologic features (Holman and Bowen, 1982), and have been the focus of field programs for several decades. Standing wave models such as these have attractive attributes in that they introduce a characteristic cross-shore length scale, and provided that at least some phase locking between edge wave modes occurs, may select preferred alongshore length scales (Huntley, 1988; Haines and Bowen, 1988).

The principal forcing mechanism for edge waves remains unclear. Leading theories suggest that edge waves result from either the nonlinear interactions of offshore wind waves (Gallagher, 1971; Bowen and Guza, 1978), or from time dependent momentum fluxes induced by modulations in break point positions (Symonds, *et al.*, 1982; Symonds and Bowen, 1984; Schaffer, 1990).

The first mechanism (referred to herein as offshore forcing) evolves from the second-order forced (or bound) waves generated by wave groups in intermediate water (Longuet-Higgins and Stewart, 1962, 1964; Hasselmann, 1962). In two dimensions, the bound wave is released at breaking and reflected at the shoreline, thus the incoming and outgoing waves form a standing pattern in the cross-shore, however without any long-shore component necessary for edge wave generation. This mechanism was extended to three dimensions by Gallagher (1971), who showed that nonlinear interactions in deep water between incident wave pairs could produce low-frequency waves with a non-zero alongshore wavenumber, thereby allowing for the possibility for edge wave generation. Bowen and Guza (1978) generalized Gallagher's model and showed with laboratory experiments that resonant response was greater than for forced response. This same conclusion was reached by Foda and Mei (1981) in a lengthy fourth order WKB-expansion of the momentum equations.

The second leading theory also evolves from modulations in incident wave amplitudes, in which forcing is derived from temporal and spatial variations in surf zone wave breaking distributions (herein referred to as surf zone forcing). Modulations in

incident wave amplitudes arise in the same manner as in the offshore mechanism; however, in the surf zone momentum is transferred from incident to lower frequencies through wave breaking. Modulations in incident wave amplitudes lead to fluctuations in the flow field with time and space scales on the order of wave groups. This idea was first explored as a theoretical mechanism for generating long waves by Foda and Mei (1981) and Symonds, *et al.* (1982).

In Foda and Mei, low frequency waves are generated by fixing the break point position of all waves and allowing incident modulations to progress to the shoreline. In nature, however, the initial break point of individual waves is not generally constant through time, nor is the breaker line usually uniform along the beach. In fact, under most conditions temporal and spatial modulations in the width of the surf zone occur on large time and space scales, on the order of infragravity scaling (Symonds, *et al.*, 1982). However, because Foda and Mei consider the case of edge wave resonance, also considered here, a more complete comparison of their results is discussed in section 4.

Symonds, *et al.* (1982) also considered the problem of long wave forcing by time modulations in surf zone width for the case of a plane sloping bed, and later included interactions with barred topography (Symonds, *et al.*, 1984). In contrast to Foda and Mei, they assume constant breaking criteria so that modulations in incident wave heights are manifested in fluctuations in the width of the surf zone. However, their model was limited to only two dimensions (no inclusion of longshore variability), precluding the possibility of edge wave forcing. Nevertheless, the results of Symonds, *et al.* suggest that edge wave generation by temporal variations in the width of the surf zone may be possible.

Subsequent work by other researchers have attempted to expound upon the Foda and Mei and Symonds, *et al.* mechanisms. Schaffer and Svendson (1988) combine the two previous ideas by allowing for fluctuations in both break point positions and incident

wave energy inside the break point, although they also limit their discussion to the two dimensional case. In a numerical model List (1992) extends this mechanism to include arbitrary topography, and further includes incoming bound waves crudely modeled empirically using field data (List, 1991), as does Schaffer and Svendsen (1988). List foregoes a more theoretical approach since it is not clear what the correct bound wave dynamics are in the shoaling and breaking region (*e.g.*, Okihiro, *et al.* 1992). In a recent theoretical work Schaffer (1990) demonstrated the possibility of three dimensional long wave forcing by including alongshore variations in incident wave amplitudes. Although Schaffer did not consider the exact case of resonance (assumed herein), some of his formulations are, in principal, similar to ours and thus a more specific comparison is discussed in section 4.

In this paper we present a theory for resonant forcing of infragravity edge waves through modulations in radiation stress gradients induced by a breaking incident wave field. In this work we consider an interacting bichromatic incident wave field whose difference wavenumbers and frequencies satisfy the exact case of edge wave resonance. The total forcing integral is separated into contributions from outside the break point (essentially the forcing mechanism of Gallagher, 1971) and from inside the fluctuating region of the surf zone. We consider the simplest case of a planar beach profile, where forcing modulations in the surf zone are determined by a time and space (cross-shore and longshore) dependent fluctuations in the width of the surf zone (*e.g.*, Symonds, *et al.*, 1982).

In the next section we present the theory for the existence of free surface gravity waves (edge and leaky modes) on a plane sloping beach (Eckart, 1951; Ursell, 1952) beginning with the forced shallow water (depth integrated), linearized, inviscid equations of motion, and leading to an analytic expression for the initial edge wave growth rate (Bowen and Guza, 1978; Holman, 1981). Model results are then presented, comparing

the relative contributions to the forcing from the components of the radiation stress and also the strength of initial growth rates in the surf zone and offshore regions. Results are then discussed in terms of the validity of model assumptions, parameter sensitivity, and implications in field situations. Comparisons are also made with other relevant theoretical work, in particular Foda and Mei (1981) and Schaffer (1990).

MODEL

Edge Wave Theory

The forced, shallow water (depth-integrated), linearized, inviscid equations of motion are (Phillips, 1977)

$$\frac{\partial u}{\partial t}+g\frac{\partial \eta}{\partial x}=-\frac{1}{\rho h}\left(\frac{\partial S_{xx}}{\partial x}+\frac{\partial S_{xy}}{\partial y}\right) \tag{II.1}$$

$$\frac{\partial v}{\partial t}+g\frac{\partial \eta}{\partial y}=-\frac{1}{\rho h}\left(\frac{\partial S_{yx}}{\partial x}+\frac{\partial S_{yy}}{\partial y}\right) \tag{II.2}$$

and the continuity equation

$$\frac{\partial \eta}{\partial t}+\frac{\partial (hu)}{\partial x}+\frac{\partial (hv)}{\partial y}=0 \tag{II.3}$$

where x and y are the cross-shore and alongshore horizontal Cartesian coordinates with x positive seaward (for a right-hand system with z positive upward), u and v are the corresponding horizontal components of velocity, η represents the sea surface elevation, h is the mean still water level, g is acceleration of gravity, ρ is the density of water, and t is time. The equations have been averaged over an incident wave period so that the time dependence is on infragravity and longer scales. S_{ij} represents the forcing by the radiation stress tensor of short (incident) waves introduced by Longuet-Higgins and Stewart (1962, 1964) and describes the flux of i-th directed momentum in the j-th direction.

Introducing the velocity potential, Φ, so that

$$u=\frac{\partial \Phi}{\partial x} \qquad \text{and} \qquad v=\frac{\partial \Phi}{\partial y} \tag{II.4}$$

and the dynamic free surface boundary condition evaluated at the sea surface ($z = 0$),

$$\eta = -\frac{1}{g}\frac{\partial \Phi}{\partial t}\bigg|_{z=0} \tag{II.5}$$

provides a relation between u, v, and η. Combining (II.1), (II.2), and (II.3) with (II.4) and (II.5), yields a single second order equation in sea surface elevation,

$$\frac{\partial^2 \eta}{\partial t^2} - g\frac{\partial}{\partial x}\left(h\frac{\partial \eta}{\partial x}\right) - g\frac{\partial}{\partial y}\left(h\frac{\partial \eta}{\partial y}\right) = -\frac{1}{\rho}\left(\frac{\partial^2 S_{xx}}{\partial x^2} + 2\frac{\partial^2 S_{xy}}{\partial x \partial y} + \frac{\partial^2 S_{yy}}{\partial y^2}\right) = \mathbf{F} \tag{II.6}$$

For a plane beach, $h = x\tan\beta$, where β is the beach slope, the homogenous (*i.e.*, free wave) case is satisfied by edge waves of the form (Eckart, 1951; Ursell, 1952)

$$\eta_n(x,y,t) = a_n \phi_n(x) e^{-i(k_e y - \sigma_e t)} \tag{II.7}$$

where σ_e and k_e are the edge wave radian frequency ($2\pi/T_e$, where T_e is the edge wave period) and longshore wavenumber ($2\pi/L_e$, where L_e is the edge wave wavelength), n is the edge wave mode number, and a_n are the complex modal amplitudes (which can be resolved into a magnitude and phase).

The cross-shore structure of the edge wave waveform, $\phi_n(x)$, is given by

$$\phi_n(x) = e^{-k_e x} L_n(2k_e x) \tag{II.8}$$

where L_n is the Laguerre polynomial of order n. Figure II.1 shows $\phi_n(x)$ for the lowest five edge wave modes plotted as a function of the nondimensional parameter

$$\chi = \frac{\sigma_e{}^2 x}{g \tan\beta} \tag{II.9}$$

(*e.g.*, Holman, 1981). The zero crossings indicate the nodal points in variance of the edge waves (in χ space). The approximate edge wave dispersion relation is given by (Eckart, 1951)

$$\sigma_e^2 = g k_e (2n+1) \tan\beta \tag{II.10}$$

where for typical low slope beaches $\tan\beta \approx \beta$.

Growth Rates

The r.h.s. of (II.6) describes the forcing that arises through second order interactions of incident waves. If the incident wave field consists of two wave trains, then forcing will consist of mean contributions from each individual wave, which drives mean flows and setup, as well as a modulating contribution arising from the wave-wave interaction that force flows at the (small) difference frequency. For the right conditions, this modulation can resonantly excite edge waves causing modal amplitude growth.

Allowing a_n to be a slowly varying function of time (II.6) becomes

$$\left(\frac{\partial^2 a_n}{\partial t^2}\phi_n + i2\sigma_e \frac{\partial a_n}{\partial t}\phi_n - \sigma_e^2 a_n \phi_n - g\beta a_n \frac{\partial \phi_n}{\partial x} - gh a_n \frac{\partial^2 \phi_n}{\partial x^2} + k_e a_n \phi_n \right) e^{-i\psi_e} = \mathbf{F} \tag{II.11}$$

after temporarily dropping the functional dependencies for simplicity and where $\psi_e = k_e y - \sigma_e t$. The third through sixth terms on the l.h.s. of (II.11) constitute the homogeneous steady state equation for shallow water waves and vanish for the case of

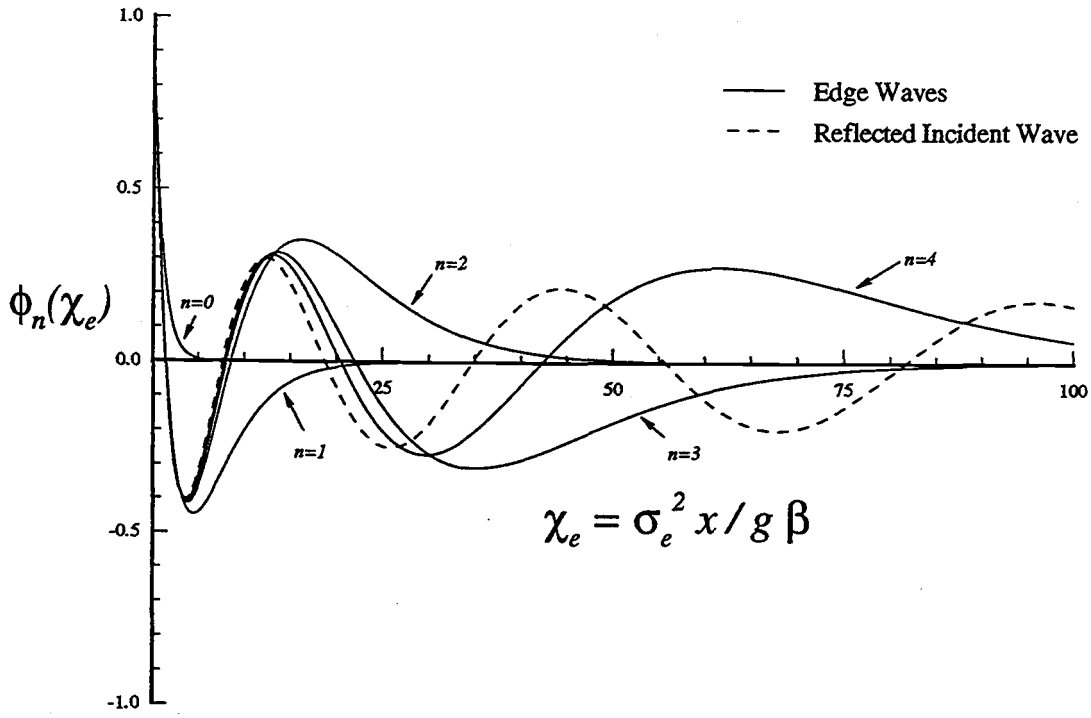

Figure. II.1. Cross-shore behavior, $\phi_n(\chi_e)$ (Eq. II.8), of the lowest five edge wave modes, $n = 0,1,2,3,4$, and the normally reflected incident wave for a plane sloping beach, plotted as a function of the non dimensional parameter $\chi_e = \sigma_e^2 x/g\beta$.

resonance considered here, leaving only the first and second term. If we assume that the edge wave growth rate is slow compared to its period, then the first term (describing the acceleration in growth) can be neglected. Thus an equation for the resonant edge wave growth rate is given by

$$i2\sigma_e \frac{\partial a_n(t)}{\partial t}\phi_n(x)e^{-i\psi_e} = -\frac{1}{\rho}\left(\frac{\partial^2 S_{xx}}{\partial x^2} + 2\frac{\partial^2 S_{xy}}{\partial x \partial y} + \frac{\partial^2 S_{yy}}{\partial y^2}\right) \tag{II.12}$$

We eliminate the cross-shore dependence in (II.12) by multiplication of $\phi_n(x)$ and then integrating in the cross-shore direction from the shoreline to infinity

$$i2\sigma_e \frac{\partial a_n(t)}{\partial t}e^{-i\psi_e}\int_0^\infty \phi_n^2(x)\mathrm{d}x = -\frac{1}{\rho}\int_0^\infty \mathbf{F}\phi_n(x)\mathrm{d}x \tag{II.13}$$

Conveniently,

$$\int_0^\infty \phi_n^2(x)\mathrm{d}x = \frac{1}{2k_e} = \frac{g\beta(2n+1)}{2\sigma_e^2} \tag{II.14}$$

where the last form is found after use of the dispersion relation (II.10).

The total forcing can be decomposed into contributions from within the surf zone, $\mathbf{F}_{sz}$, and from offshore, $\mathbf{F}_{off}$. Thus, using (II.14), (II.13) becomes

$$\frac{i}{a_i^o f_e}\frac{\partial a_n(t)}{\partial t}e^{-i\psi_e} = -\frac{2\pi}{a_i^o \rho g\beta(2n+1)}\left(\int_0^{x_b}\mathbf{F}_{sz}\phi_n(x)\mathrm{d}x + \int_{x_b}^\infty \mathbf{F}_{off}\phi_n(x)\mathrm{d}x\right) \tag{II.15}$$

where a_i^o is the mean incident wave amplitude. In (II.15) we have normalized the growth rate $\partial a_n(t)/\partial t$ by the edge wave frequency and the mean incident wave amplitude (described later). Thus the inverse of the normalized growth rate represents the number of edge wave periods necessary for the edge wave to grow to the size of the incident waves (based only on the initial growth rate and in the absence of friction).

Parameterizing the Forcing

Following Phillips (1977), the general form of radiation stress is given by

$$S_{\alpha\beta} = -\tau_{\alpha\beta} + \rho \int_{-h}^{\overline{\eta}} \overline{\frac{\partial \Phi}{\partial x_\alpha}\frac{\partial \Phi}{\partial x_\beta}} dz + \delta_{\alpha\beta}\left(\int_{-h}^{\overline{\eta}} \overline{p} dz - \frac{1}{2}\rho g\left(h+\overline{\eta}\right)^2 + \frac{1}{2}\rho g \overline{\eta^2} \right) \qquad \text{(II.16)}$$

where α and β denote either horizontal coordinate, $\tau_{\alpha\beta}$ is the integrated Reynolds stress (assumed negligible), and $\delta_{\alpha\beta}$ is the Kronecker delta. The momentum balance has been spatially averaged in the direction of the wave crests (allowing separation of the turbulent and wave terms), and temporally averaged over the incident wave period (allowing mean or slowly varying properties to be evaluated). An expression for the mean pressure, $\overline{p}$, is derived from the vertical flux of vertical directed momentum (Longuet-Higgins and Stewart, 1964)

$$\overline{p} = -\left(\rho g z + \overline{\left(\frac{\partial \Phi}{\partial z}\right)^2} \right) \qquad \text{(II.17)}$$

In shallow water the z-derivatives vanish, so that $\overline{p} = -\rho g z$. Utilizing (II.17), (II.5), and assuming $\overline{\eta} \approx 0$ at second order, (II.16) becomes

$$S_{\alpha\beta} \approx \rho h \overline{\frac{\partial \Phi}{\partial x_\alpha}\frac{\partial \Phi}{\partial x_\beta}} + \delta_{\alpha\beta}\frac{\rho}{2g}\overline{\left(\frac{\partial \Phi}{\partial t}\right)^2} \tag{II.18}$$

We consider the bichromatic case where the incident wave field is composed of two discrete wave trains with slightly different wavenumber and frequency,

$$\Phi = \Phi_1 + \Phi_2 \tag{II.19}$$

where the subscripts 1 and 2 signify the independent incident waves. Substituting Φ into (II.18) produces

$$S_{\alpha\beta} = S_{\alpha\beta}(\Phi_1\Phi_1) + S_{\alpha\beta}(\Phi_2\Phi_2) + \hat{S}_{\alpha\beta}(\Phi_1\Phi_2) \tag{II.20}$$

where ^ denotes the radiation stress arising from the cross-interaction, $\Phi_1\Phi_2$. The first two terms of (II.20) represent the self-self interactions which generate mean flows and harmonics but do not contribute to low frequency forcing, and are therefore not considered.

We choose the velocity potential for individual linear surface gravity waves (denoted with the subscript *i*) in shallow water over a plane sloping bottom after Stoker (1947)

$$\Phi_i = \frac{a_i g}{\sigma_i}\left(J_o(\mathrm{X}_i)\cos\psi_i + Y_o(\mathrm{X}_i)\sin\psi_i\right) \tag{II.21}$$

where $$\mathrm{X}_i = 2\left(\frac{\sigma_i^2 x}{g\beta}\right)^{1/2}$$

$$\psi_i = (k_i y - \sigma_i t)$$

and J_o and Y_o are the zero order bessel functions of the first and second kind, respectively. For $X_i > 3$ (equivalent to $H >\sim T^2\beta^2/2$, so valid for nearly all oceanic cases), the bessel functions may be approximated by

$$J_o(X_i) \approx \left(\frac{2}{\pi X_i}\right)^{1/2} \cos\left(X_i - \frac{\pi}{4}\right) \tag{II.22}$$

$$Y_o(X_i) = \left(\frac{2}{\pi X_i}\right)^{1/2} \sin\left(X_i - \frac{\pi}{4}\right)$$

(Abramowitz and Stegun, 1965). Using (II.22) in (II.21), and introducing complex notation, yields the following form for Φ_i

$$\Phi_i(x,y,t) = \frac{a_i g}{\sigma_i}\left(\frac{2}{\pi X_i}\right)^{1/2} e^{i\left(X_i - \psi_i + \pi/4\right)} \tag{II.23}$$

Substitution of (II.23) into (II.20) produces terms with sum and difference wavenumbers and frequencies. The sum terms (high frequency forced waves, Herbers and Guza, 1991) are unimportant to the generation of infragravity motions (Bowen and Guza, 1978) and are thus not considered further. The difference terms describe the long time and space scales of the incident wave modulation and allow for the possibility of edge wave forcing.

Since we are interested in the response of edge wave growth, we will choose the incident wave pairs to satisfy the resonance condition, such that

$$\sigma_e = \sigma_1 - \sigma_2 \qquad \text{and} \qquad |k_e| = |k_1 - k_2| \tag{II.24}$$

where k_1 and k_2 are the longshore wavenumbers of the incident waves and the e subscript indicates the difference values associated with edge waves which satisfies the dispersion relation (II.10). Incident wave angles are assumed to follow Snell's law for wave refraction and are chosen at the break point where the linear shallow water phase velocity is simply a function of the local depth, $c = \sqrt{gh}$, so that

$$k_i = \frac{\sigma_i^2}{g} \sin \alpha_\infty = \frac{\sigma_i}{\sqrt{gh_o}} \sin \alpha_i^o = \text{constant} \tag{II.25}$$

where ∞ indicates the deep water condition and α_i^o are the wave angles of the individual waves taken at some reference depth, h_o.

If we further reference a_i to the break point, where $h_o = h_b$, and evaluate (II.23) with (II.5), then products $a_1 a_2$ are given by

$$a_1 a_2 = \frac{\pi}{2} a_1^o a_2^o \left(\mathrm{X}_1^o \mathrm{X}_2^o \right)^{1/2} \tag{II.26}$$

where the superscript ° refers to values at the reference position (break point).

Now substituting (II.23) into (II.20), incorporating (II.24), (II.25), and (II.26), and taking the appropriate derivatives gives an analytic form of the fluctuating, second order radiation stress due to the interaction of two shallow water incident waves over a plane sloping bed

$$\hat{S}_{\alpha\beta} = \frac{\rho g a_1^o a_2^o}{2} \frac{\mathrm{X}_e^o}{\mathrm{X}_e} e^{i(\mathrm{X}_e - \psi_e)} \left(F_{\alpha\beta} - iG_{\alpha\beta} \right) \tag{II.27}$$

where $$F_{\alpha\beta} = \begin{vmatrix} 3 + \frac{1}{2}\Lambda & \sin\alpha_1^o + \sin\alpha_2^o \\ \sin\alpha_1^o + \sin\alpha_2^o & 2\sin\alpha_1^o \sin\alpha_2^o + 1 \end{vmatrix}$$

$$G_{\alpha\beta} = \begin{vmatrix} X_e\Lambda & \frac{\Lambda}{2}\left(X_1 \sin\alpha_1^o - X_2 \sin\alpha_2^o\right) \\ \frac{\Lambda}{2}\left(X_1 \sin\alpha_1^o - X_2 \sin\alpha_2^o\right) & 0 \end{vmatrix}$$

$$\Lambda = \frac{\Gamma^2}{X_e^2}$$

$$\Gamma = \frac{\sigma_e}{(\sigma_1\sigma_2)^{1/2}}$$

$$X_e = 2\left(\frac{\sigma_e^2 x}{g\beta}\right)^{1/2}$$

Using typical values found in nature, $f_1 \approx f_2 \approx 0.1$ Hz, $x_b \approx 100$ m, and $\beta \approx 0.02$, we find Λ is $O(10^{-3})$ at the break point, and therefore terms containing Λ contribute negligibly to the interaction and are henceforth ignored.

Offshore Response

The forcing function outside the break point is found directly by inserting (II.27) into the r.h.s. of (II.12) and evaluating the second spatial derivatives. The total expansion of the forcing term is

$$\mathbf{F}_{off} = 6\rho g a_1^o a_2^o X_e^o e^{i(X_e - \psi_e)}\left(\frac{\sigma_e^2}{g\beta}\right)^2$$

$$\cdot\left(\frac{3 - X_e^2 - iX_e}{X_e^5} + \frac{\Sigma\alpha}{6(2n+1)X_e^2} - \frac{2\alpha_{12}+1}{12(2n+1)^2 X_e}\right) \qquad \text{(II.28)}$$

where $\sum\alpha = \sin\alpha_1 + \sin\alpha_2$ and $\alpha_{12} = \sin\alpha_1 \sin\alpha_2$. The three terms on the r.h.s of (II.28) are derived from the components of the radiation stress corresponding to the three terms on the r.h.s. of (II.12), respectively. Note that the second and third terms (derived from S_{xy} and S_{yy}) are both real and of opposite sign, and thus have phases which will directly oppose (π out of phase). The relationship of the three components of the forcing are compared more completely in section 3.

Eq. II.28 represents the parameterization of the offshore forcing mechanism for generating low frequency edge waves from the nonlinear difference interaction of two incident waves. In this formulation we have assumed that the reference position designated in (II.26) is at the break point, and that incident wave angles and amplitudes at the break point are constant (hence are not dependent on more rigorous shoaling characteristics). We further assume at breaking that the incident wave height at the break point is given as a linear function of the depth (Miche, 1954; Thornton and Guza, 1982), where $h = h_o$

$$a_i^o = \frac{\gamma x_b \tan\beta}{2} \qquad x = x_b \qquad \text{(II.29)}$$

Furthermore we consider one wave to be much larger than the other,

$$a_2 = \delta a_1 \qquad \text{(II.30)}$$

where $\delta << 1$ is a constant. In this manner the primary wave, a_1, determines the mean wave amplitude and the modulation (about the mean) is determined by a_2, as was done by Symonds, *et al.* (1982).

Using these simplifications and inserting (II.28) into the second integral on the r.h.s. of (II.15) results in a complex expression for the initial growth rate (response) of

the edge waves by offshore forcing. After taking the real part, an expression for the normalized initial growth rate magnitude and phase, θ_n, is given by

$$\left|\frac{1}{f_e a_i^o}\frac{\partial a_n(t)}{\partial t}\right| = \frac{3\pi}{4}\frac{\gamma\delta\left(X_e^o\right)^3}{(2n+1)}\left(P_n^2+Q_n^2\right)^{1/2} \qquad X > X_b \qquad \text{(II.31)}$$

$$\theta_n = \tan^{-1}\left(\frac{Q_n}{P_n}\right)$$

where
$$P_n = \int_{X_b}^{\infty}\left(B_2(X_e)\cos X_e - B_1(X_e)\sin X_e\right)\phi_n(X_e)X_e dX_e$$

$$Q_n = \int_{X_b}^{\infty}\left(B_1(X_e)\cos X_e + B_2(X_e)\sin X_e\right)\phi_n(X_e)X_e dX_e$$

$$B_1(X_e) = \frac{3-X_e^2}{X_e^5} + \frac{\sum\alpha}{3(2n+1)X_e^2} - \frac{2\alpha_{12}+1}{12(2n+1)X_e}$$

$$B_2(X_e) = \frac{3}{X_e^4}$$

Surf Zone Response

The cross-shore integral parameterizing the surf zone contribution to the total edge wave forcing ranges from the shoreline to the break point, $0 \le x \le x_b$. As with our parameterization of the offshore forcing, $x > x_b$, we choose the amplitude of one wave to be much larger than the other (Eq. II.30). Inside the break point wave height is limited by the well known saturation condition (II.29). Following the ideas of Symonds, *et al.*

(1982), we do not allow modulations in wave amplitude inside the minimum break point by choosing γ to be constant for all waves. Thus once breaking occurs no modulations in the forcing can exist since the radiation stress gradients are constant, and lead only to a mean set-up (Bowen, *et al.*, 1968).

Thus for a plane beach incident wave modulations outside the surf zone are manifested as spatial and temporal variations in the width of the surf zone (Figure II.2). Symonds, *et al.* used this as the basis for providing a two-dimensional long wave generation mechanism. The total forcing modulation is determined by the maximum and minimum break point amplitudes, $a_{\max} = a_1 + \delta a_1$ and $a_{\min} = a_1 - \delta a_1$, respectively, so that the cross-shore range over which forcing occurs is defined using (II.29) by

$$\overline{x_b} - \delta\overline{x_b} \le x_b \le \overline{x_b} + \delta\overline{x_b} \tag{II.32}$$

This is in contrast to others (*e.g.*, Foda and Mei, 1981; Schaffer and Svendson, 1988) who considered a fixed (constant) break point position, and a modulation in γ which is a function of wave amplitude and thus varies through time.

We formulate the forcing function inside the surf zone just as before in the offshore region. Using (II.29), (II.30), and (II.31), an expression for the interaction radiation stress at the break point is

$$\hat{S}_{\alpha\beta} = \frac{\rho g}{8}\gamma^2\beta^2\delta^2 x_b^2 \frac{X_e^o}{X_b} e^{i(X_e - \psi_e)} \begin{vmatrix} 3 & \Sigma\alpha \\ \Sigma\alpha & 2\alpha_{12}+1 \end{vmatrix} \qquad x = x_b \tag{II.33}$$

At the break point, $X_e^o \equiv X_b$.

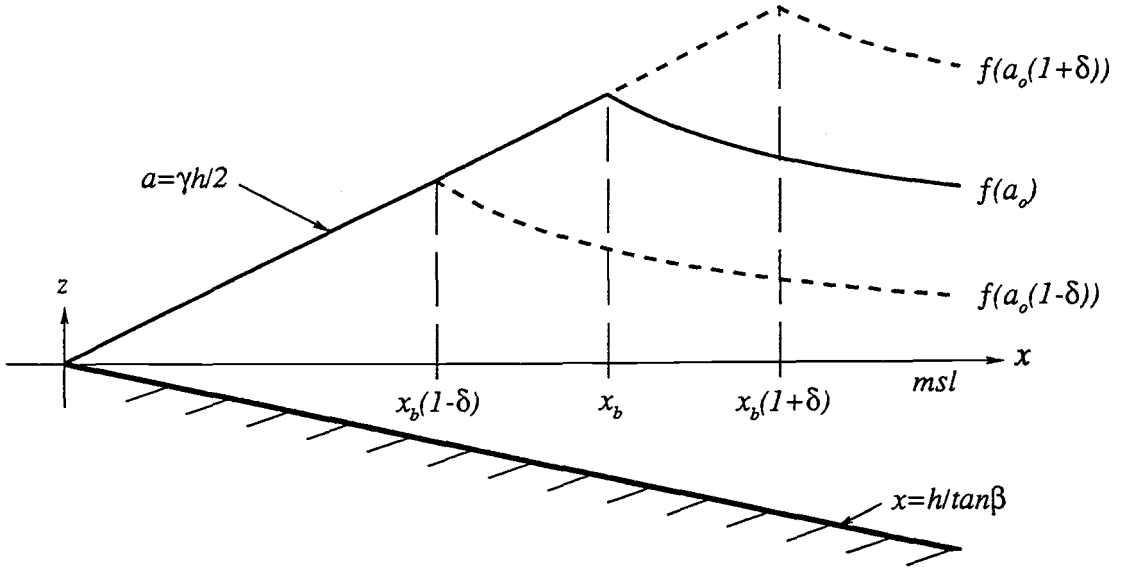

Figure II.2. Graphical representation of the envelop of incident wave amplitudes over a plane sloping bed as a function of cross-shore distance. Surf similarity (Eq. II.29) is assumed once waves are breaking so that modulations in incident amplitudes, δ, are manifested as variations in surf zone width. That is, larger waves simply break further offshore. The vertical (elevation) and horizontal (cross-shore distance) dimensions are arbitrary.

The surf zone forcing function is found by evaluating the second spatial derivatives on the r.h.s. of (II.12)

$$\mathbf{F}_{sz} = \frac{1}{8}\rho g\gamma^2\beta^2\delta e^{i(X_e-\psi_e)}$$

$$\cdot\left(\frac{24-3X_e^2+i21X_e}{4}+\frac{\left(X_e^3-i5X_e^2\right)\Sigma\alpha}{4(2n+1)}-\frac{X_e^4(2\alpha_{12}+1)}{16(2n+1)^2}\right) \qquad \text{(II.34)}$$

The dependence of wave angle on depth (hence cross-shore location) in the S_{xy} and S_{xy} terms are eliminated using (II.25) (the incident alongshore wavenumber is conserved across the surf zone). As with the offshore results (Eq. II.28), the second and third terms in the forcing have opposite signs. However, since the S_{xy} term in the surf zone region is complex, its phase relationship with the other terms is not necessarily π out of phase. Relative contributions to the total forcing are investigated further in section 3.

Since we are taking γ to be constant, all modulations inside the initial breakpoint vanish. In essence, variations in the forcing are defined by a wave maker type problem, where the forcing is turned on and off at the initial breakpoint (as in Symonds, *et al.*, 1982). This situation is shown graphically in Figure II.3, taken with slight modification from Symonds, *et al.* in which their $\sigma_e t$ dependence has been replaced with our ψ_e dependence. Once waves are breaking no forcing occurs since S_{ij} gradients are constant. Outside the break point all forcing is from the offshore mechanism (II.28). Thus periodic fluctuations in surf zone forcing arise from fluctuations in the position of the initial break point on time and space scales of the modulation. Alongshore modulations (ψ_e) allows for the possibility of resonant edge wave forcing.

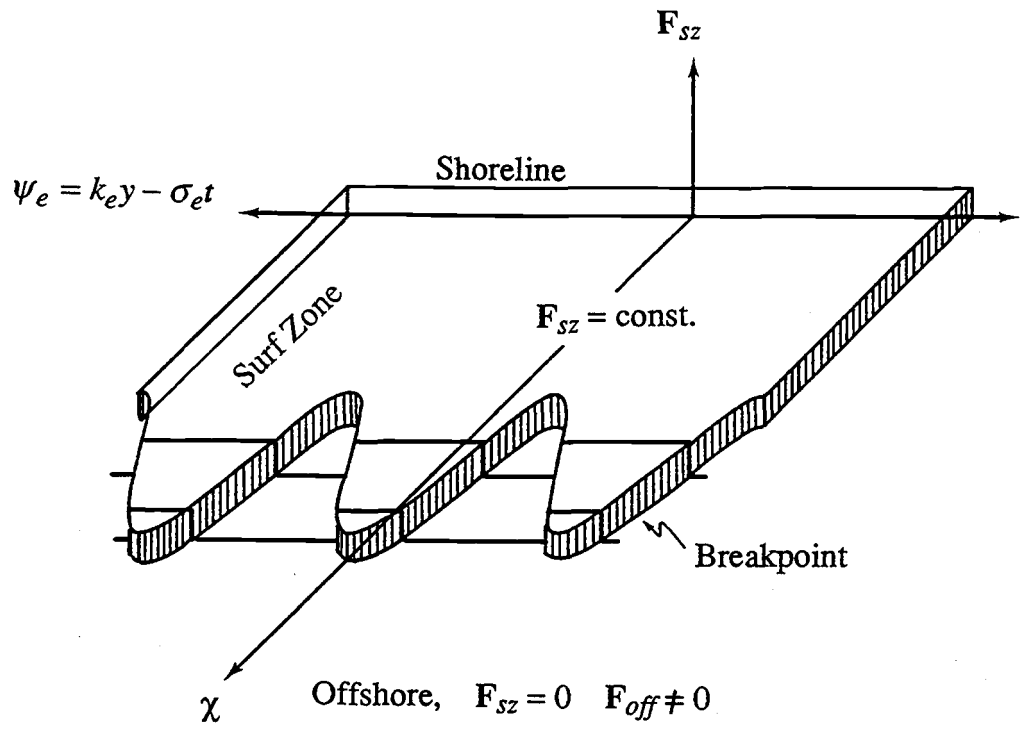

Figure II.3. Schematic representation of the forcing in the nearshore due to a sinusoidally varying break point position. The figure is from Symonds, *et al.* (1982) with slight modification in which their $\sigma_e t$ dependence has been replaced with $\psi_e = k_e y - \sigma_e t$. Alongshore variations give rise to the possibility of resonant edge wave forcing.

Following Symonds, *et al.*, we represent the forcing as a (complex) Fourier Series,

$$\mathbf{F}_{sz}(\mathrm{X}_e) = \varsigma_o(\mathrm{X}_e) + \sum_{m=1}^{\infty} \varsigma_m(\mathrm{X}_e) e^{-i\psi'} + (*) \tag{II.35}$$

where $\varsigma_m = \zeta_m + i\xi_m$

$$\zeta_m(\mathrm{X}_e) = \frac{1}{2\pi} \int_{\psi_1(\mathrm{X}_e)}^{\psi_2(\mathrm{X}_e)} \mathbf{F}_{sz}(\mathrm{X}_e) \cos m\psi' \, \mathrm{d}\psi'$$

$$\xi_m(\mathrm{X}_e) = \frac{1}{2\pi} \int_{\psi_1(\mathrm{X}_e)}^{\psi_2(\mathrm{X}_e)} \mathbf{F}_{sz}(\mathrm{X}_e) \sin m\psi' \, \mathrm{d}\psi'$$

where ψ_1 and ψ_2 define the interval over which forcing occurs, and (*) indicates the complex conjugate of the previous terms under the summation. Symonds, *et al.* present an extensive discussion for finding the limits of integration for the two dimensional case. We extend their ideas to three dimensions in the following.

The mean break point amplitude is defined by the largest wave, and the fluctuation about the mean is defined by the amplitude modulation, δ, such that

$$a_b = a_1 \left(1 + \delta \cos\left(\frac{1}{2} \overline{\mathrm{X}_b} + \psi_e \right) \right) \tag{II.36}$$

where $\overline{\mathrm{X}_b}$ is the mean X_e value corresponding to $x = x_b$. We can express (II.36) in terms of the more meaningful break point positions using (II.29)

$$x_b = \overline{x_b} \left(1 + \delta \cos\left(\frac{1}{2} \overline{\mathrm{X}_b} + \psi_e \right) \right) \tag{II.37}$$

where $\overline{x_b}$ is the mean break point position. An explicit derivation of (II.37) is shown in the Appendix. The limits of integration in (II.35) are determined when the argument of (II.37) is a maximum or minimum

$$\left|\frac{1}{2}\overline{X_e} + \psi_e\right| = \cos^{-1}\left(\frac{x_b - \overline{x_b}}{\delta\overline{x_b}}\right) = \tau \qquad \text{(II.38)}$$

Symonds, *et al.* (1982) show that for small δ the limits of integration are symmetric, hence $\psi_2(X_e) = \frac{1}{2}\overline{X_e} + \psi_e$ and $\psi_1(X_e) = -\psi_2(X_e)$. Using (II.38), the Fourier coefficients in (II.35) are

$$\zeta_o = 1 \qquad \text{(II.39)}$$

$$\zeta_m = F_{sz}(X_e)\frac{\sin m\tau}{m\tau} \qquad m = 1, 2, \ldots$$

$$\xi_m = 0 \qquad m = 0, 1, 2, \ldots$$

The first term in the series ($m = 0$) represents the mean value, or set-up (Symonds, *et al.*, 1982). Since we are only interested here in low frequency modulations in the forcing, we do not consider this term further. For $m > 0$, the series consists of a primary ($m = 1$) and harmonics ($m > 1$). In keeping with the lowest order approximation implicitly assumed in our formulation, we consider only forcing contributions from the primary. Thus to lowest order the forcing expressed in (II.34) is given by

$$\mathbf{F}_{sz} = \frac{1}{4}\rho g \gamma^2 \beta^2 \delta e^{-i\psi'} \frac{\sin\tau}{\tau}$$

$$\cdot \left(\frac{24 - 3X_e^2 + i21X_e}{4} + \frac{\left(X_e^3 - i5X_e^2\right)\Sigma\alpha}{8(2n+1)} - \frac{X_e^4(2\alpha_{12}+1)}{16(2n+1)^2} \right) \qquad \text{(II.40)}$$

Eq. II.40 represents the long wave forcing arising from lowest order fluctuations in break point amplitudes. The initial growth rate is found by inserting (II.40) into the first integral on the r.h.s. of (II.15) and evaluating in the same manner as in the offshore region, except that the limits of integration are now given by (II.32). Taking the real part yields expressions for the magnitude and phase of the initial edge wave growth rate

$$\left| \frac{1}{f_e a_i^o} \frac{\partial a_n(t)}{\partial t} \right| = \frac{\pi\gamma\delta}{2(X_e^o)^2(2n+1)} \left(M_n^2 + N_n^2\right)^{1/2} \qquad X_1 \le X_b \le X_2 \qquad \text{(II.41)}$$

$$\theta_n = \tan^{-1}\left(\frac{N_n}{M_n}\right)$$

where

$$M_n = \int_{X_1}^{X_2} \left(A_1(X_e)\cos\tfrac{1}{2}\overline{X_e} + A_2(X_e)\sin\tfrac{1}{2}\overline{X_e} \right) \frac{\sin\tau}{\tau} \phi_n(X_e) X_e dX_e$$

$$N_n = \int_{X_1}^{X_2} \left(A_2(X_e)\cos\tfrac{1}{2}\overline{X_e} - A_1(X_e)\sin\tfrac{1}{2}\overline{X_e} \right) \frac{\sin\tau}{\tau} \phi_n(X_e) X_e dX_e$$

$$A_1(X_e) = -21X_e + \frac{5X_e^2\Sigma\alpha}{2n+1}$$

$$A_2(X_e) = 24 - 3X_e^2 + \frac{X_e^3\Sigma\alpha}{2n+1} - \frac{X_e^4(2\alpha_{12}+1)}{4(2n+1)^2}$$

where $X_1 = \overline{X_b} - \delta\overline{X_b}$ and $X_1 = \overline{X_b} + \delta\overline{X_b}$.

MODEL RESULTS

The results are presented in two parts. The first focuses on the relative magnitudes of S_{ij} gradients which comprise the second order forcing functions in the offshore (Eq. II.28) and surf zone (Eq. II.34) regions. The second part compares initial growth rate amplitudes and phases in the two regions (Eq. II.31 and II.41) and for the total combined forcing. Sensitivity to mode number, n, and wave angle, α^o, are examined in each part. Model parameters used in the following analysis were $\beta = 0.01$, $\gamma = 0.42$, $\delta = 0.1$, and $x_b = 100$ m (chosen as reasonable for field situations). Additionally, the upper limit of integration in the offshore region, $x_{\max} = \overline{x_b} b_{\max}$ was set by $b_{\max} = 100$. The effect of changing δ and $b_{\max}$ on the growth rates is discussed in section 4. For convenience incident wave angles were chosen to be identical at the break point (similar to Schaffer, 1990). The range of values plotted, $\chi_b \leq 10$ (Eq. II.9 where $x = x_b$), covers typical infragravity frequencies (for constant x_b/β) commonly observed in nature (*i.e.*, Oltman-Shay and Guza, 1987).

Forcing

The relative strength of the components of the radiation stress forcing for mode 0 edge waves by the offshore and surf zone mechanisms is shown in Figure II.4. The magnitude and phase of $\partial^2 S_{xx}/\partial x^2$, $\partial^2 S_{xy}/\partial x \partial y$, and $\partial^2 S_{yy}/\partial y^2$, and the total (vector sum) forcing for the case of $\alpha_1 = \alpha_2 = 10^\circ$ is plotted as a function of non dimensional χ_b. For small χ_b (<~2.5) the S_{xx} terms dominate the forcing in each region. At χ_b >~ 2.5, S_{yy} becomes the more dominate term, with S_{xy} being an order of magnitude less in the offshore region and a factor of ~5 less for the surf zone mechanism.

The effect of stronger forcing at increasing χ_b for the mode 0 case is not physically realized in nature. This is because the energy transfer from incident wave forcing to the

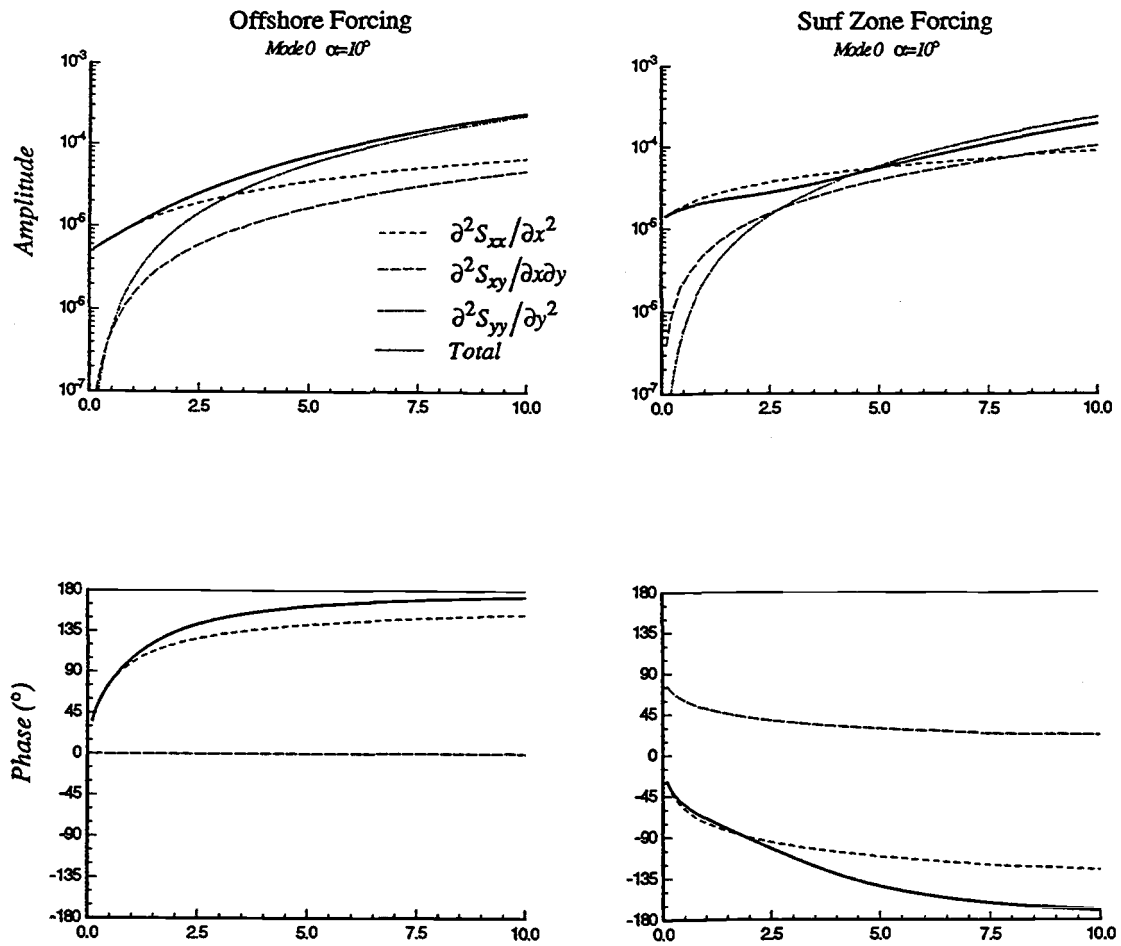

Figure II.4. Contributions to the mode 0 edge wave forcing by the offshore (Eq. II.28; left panels) and surf zone (Eq. II.34; right panels) mechanisms due to the three components of the radiation stress, $\partial^2 S_{xx}/\partial x^2$, $2\partial^2 S_{xy}/\partial x \partial y$, and $\partial^2 S_{yy}/\partial y^2$, and the vector sum, plotted as a function of $\chi_b = \sigma_e^2 x_b / g\beta$. Results are shown for $\alpha_1^o = \alpha_2^o = 10°$. Forcing amplitudes (m/sec^2) are plotted on a log scale in the upper panels; phases (degrees) on a linear scale are shown in the lower panels. The legend for identifying the components of the forcing are shown in the upper left hand panel. Results are computed for $\beta = 0.01$, $\gamma = 0.42$, $\delta = 0.1$, and $x_b = 100$ m.

edge wave depends on the cross-shore (standing) structure of the edge wave waveform, $\phi_n(x)$ (Eq. II.8). Forcing at χ_b greater than the turning point of the wave is simply a result of requiring the incident wave longshore wavenumbers and frequencies to match the resonance condition (Eq. II.24) specified by the edge wave dispersion relation (II.10).

Interestingly, the phase of S_{ij} is independent of both n and α^o. However, because the total forcing depends also on S_{ij} amplitudes, the resultant (total) phase will be dependent on n and α^o. Offshore, S_{xy} and S_{yy} are always π out of phase and hence will oppose and tend to cancel, particularly when their amplitudes are comparable (at higher χ_b). In the surf zone, S_{yy} has constant phase. For $\chi_b \rightarrow 10$, S_{xx} and S_{xy} approach a relative phase of $\sim\pi$, and will therefore tend to reduce the total forcing. Thus, the total forcing in each region may be less than for any of the particular S_{ij} components at particular χ_b.

Also clearly evident is that the magnitudes of the S_{ij} components and the total are comparable in the offshore and surf zone mechanisms. Surf zone forcing is slightly greater at small χ_b (<~1.5), with the offshore mechanism approximately twice as large as $\chi_b \rightarrow 10$ (the slope of the forcing function is greater in the offshore region). In general, the behavior of the forcing is very similar in each region, suggesting that each region can contribute significantly to the total forcing.

The S_{ij} forcing terms for edge wave modes, $n = 1,\ 2,$ and 3, is shown in Figure II.5 for $\alpha_1 = \alpha_2 = 10^{\circ}$. Only the forcing magnitudes are shown since the phases of S_{ij} are the same as for mode 0 (Figure II.4). The behavior of the forcing is similar in each region, with S_{xx} dominating all modes. This is largely through the inverse dependence of S_{xy} and S_{yy} on n, whereas S_{xx} is independent of mode. Furthermore, since S_{xy} varies as $(2n+1)^{-1}$ and S_{yy} as $(2n+1)^{-2}$, the contributions from S_{xy} also become relatively large at higher n. The total phase approaches the phase of S_{xx} rapidly as n increases, and

Figure II.5. Radiation stress forcing terms and the vector sum for edge wave modes 1-3, with $\alpha_1^o = \alpha_2^o = 10°$, plotted as a function of $\chi_b = \sigma_e^2 x_b / g\beta$. Contributions from the offshore (Eq. II.28) and surf zone (Eq. II.34) mechanisms are shown in the upper and lower panels, respectively. Only the amplitudes are plotted since the phases are identical to mode 0 (Figure II.4). The legend for identifying the components of the forcing is shown in the upper left hand panel, and is the same as in Figure II.4. Results are computed for $\beta = 0.01$, $\gamma = 0.42$, $\delta = 0.1$, and $x_b = 100$ m.

$\alpha = 10°$

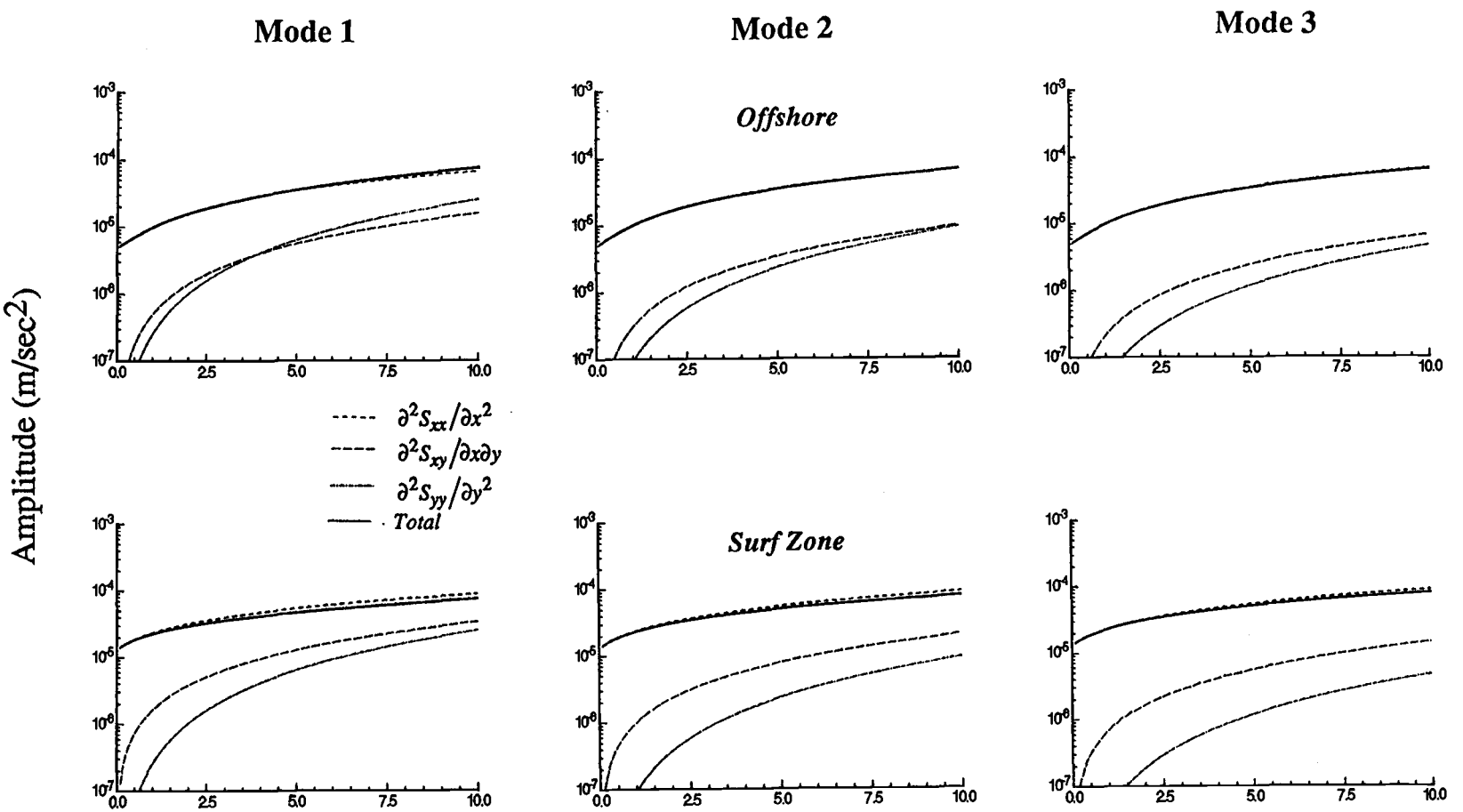

$\chi_b = \sigma_e^2 x_b / g\beta$

hence the phase dependence on n is weak. In general, the forcing magnitudes in the offshore and surf zone regions are about the same for all n.

The effect of changing α^o is examined in Figure II.6 with $\alpha_1 = \alpha_2 = 1°$, 10°, and 30°. Results for a mode 1 edge wave are shown as a representative example. Again the results are similar in the two regions. At small α^o (1°), the S_{xx} terms dominate the forcing, being approximately an order of magnitude greater than S_{yy}, which in turn is also at least an order of magnitude larger than S_{xy} (which $\rightarrow 0$ as $\alpha^o \rightarrow 0$). As α^o increases, S_{xy} rapidly increases due to its dependence on $2\sin\alpha^o$ (for $\alpha_1 = \alpha_2$), whereas S_{yy} is relatively insensitive to α^o because it depends on $1+2\sin^2\alpha^o$. At large incident angles (30°), S_{xy} can be of the same order as S_{xx}, particularly for the surf zone mechanism ($\chi_b >\sim 7.0$). However, because the phases of S_{xy} and S_{xx} approach π at large χ_b they tend to cancel. Thus the total forcing is actually less than for either of the components individually.

Growth Rates

Normalized growth rate magnitudes, $\left|(a_o f_e)^{-1}\,\partial a_n(t)/\partial t\right|$, and phases, θ_n, for the offshore (Eq. II.31) and surf zone (Eq. II.41) regions and the total (vector sum) are shown in Figure II.7 for edge wave modes 0-4 with $\alpha_1 = \alpha_2 = 10°$. The amplitudes are plotted on a log scale and the phases on a linear scale, as a function of χ_b. Clearly evident is that the growth rates from the surf zone mechanism are comparable throughout most of the χ_b range plotted. Thus neglecting the surf zone contribution to the forcing appears to be a poor assumption.

Also evident is that the growth rates are rapid, approaching a magnitude of 10^{-1} for $n = 0$ at small χ_b (somewhat less for higher modes). Because of the choice of normalization, the inverse of the growth rate magnitude predicts the number of edge wave periods for the edge wave amplitude to grow to the size of the incident waves. Thus

Figure II.6. Effect of α^o on the radiation stress forcing functions for a mode 1 edge wave plotted as a function of $\chi_b = \sigma_e^2 x_b / g\beta$. Results are shown for $\alpha_1^o = \alpha_2^o = 1°, 10°,$ and 30° in the left, middle, and right panels, respectively. Contributions from the offshore (Eq. II.28) and surf zone (Eq. II.34) mechanisms are shown in the upper and lower panels, respectively. Only the amplitudes are plotted since the phases are the same as in Figure II.4. The legend for identifying the components of the forcing is shown in the upper middle panel, and is the same for Figures II.4 and II.5. Results are computed for $\beta = 0.01$, $\gamma = 0.42$, $\delta = 0.1$, and $x_b = 100$ m.

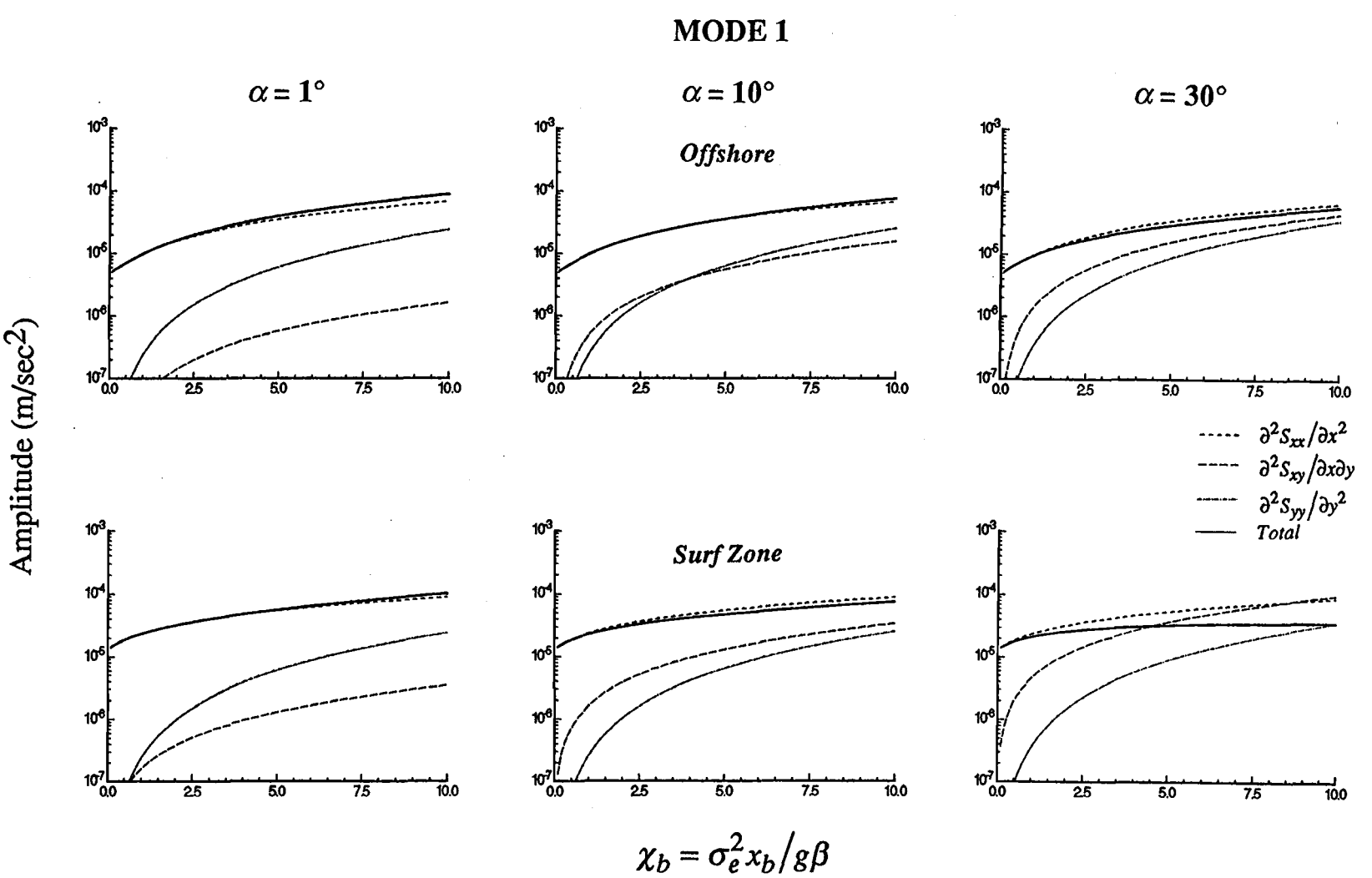
MODE 1
$\alpha = 1°$
$\alpha = 10°$
$\alpha = 30°$
Offshore
Surf Zone
Amplitude (m/sec^2)
$\partial^2 S_{xx}/\partial x^2$
$\partial^2 S_{xy}/\partial x \partial y$
$\partial^2 S_{yy}/\partial y^2$
Total
$\chi_b = \sigma_e^2 x_b / g\beta$

Figure II.7. Normalized initial growth rate magnitude (upper) and phase (lower) for the offshore (left panel; Eq. II.31), surf zone (middle panel; Eq. II.41), and total (right panel) edge wave forcing mechanisms, plotted as a function of $\chi_b = \sigma_e^2 x_b / g\beta$. Results are shown for the first 5 edge wave modes with $\alpha_1^o = \alpha_2^o = 10°$. The legend for indicating mode number is in the upper left hand panel. Growth rates (non-dimensional) are plotted on a log scale and phases (degrees) are plotted on linear scale. The inverse of the growth rate is the number of edge wave periods necessary for the edge waves to grow to the size of the incident waves (assuming no damping). Results are shown for $\beta =$ 0.01, $\gamma = 0.42$, $\delta = 0.1$, $x_b = 100$ m, and $b_{max} = 100$.

Mode 0-4 Growth Rates $\alpha = 10°$

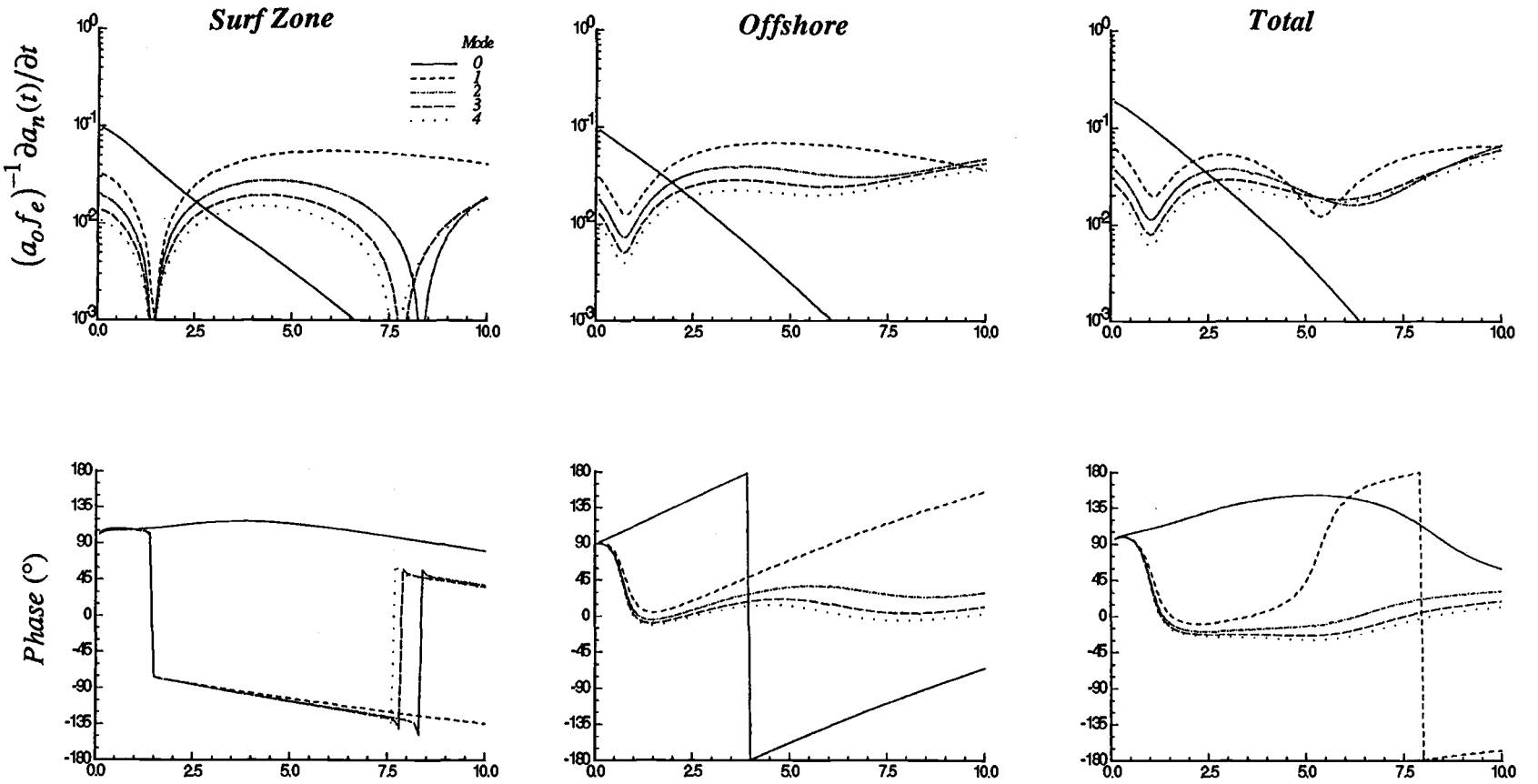

$$\chi_b = \sigma_e^2 x_b / g\beta$$

resonantly excited edge waves could grow to the same amplitude as the incident modulation in as fast as 10-20 edge wave periods (assuming no damping). This is in contrast to previous results of Foda and Mei (1981) who predicted growth rates on the order of days. However, the model predicts only initial growth rates, in which final amplitudes after a finite length of time can not be predicted. In fact any reasonable damping mechanism is likely to be different in the two forcing regions, and could quite possibly have characteristics which lead to preferential damping of high frequencies and low modes (Bowen and Guza, 1978; Holman, 1981).

The only known measurements of growth rates for progressive edge waves are from the laboratory investigation of Bowen and Guza (1978). Strict comparison with their results is difficult since their discussion was limited to very narrow $\chi_b \approx 0.25$, and furthermore they have $\delta = 1.0$ thus violating our assumption of small amplitude modulation (discussed more in section 4). Their observed growth rate is over an order of magnitude slower than predicted by our model (although much less than in Foda and Mei, 1981). Although a more precise reason for this discrepancy is not known, they show that viscous damping in the laboratory is clearly important.

Interestingly, the results for the surf zone forcing mechanism are not monotonic for $n > 0$, but show sharp valleys corresponding to zero crossings in $\phi_n(x)$. Figure II.8 shows the absolute value of Figure II.1, $|\phi_n(x)|$ (proportional to the variance of the edge wave modes), plotted out to $\chi_b = 10$. The shape of the edge wave profiles are similar to the growth rates for the surf zone mechanism. Thus for a fixed x_b, a predicted structure in the power spectrum, or equivalently a frequency selection mechanism, is implied. This structure is especially important for $\chi_b <\sim 2.5$ where the surf mechanism is highly frequency dependent. However, the dip in the offshore growth rate at $\chi_b \approx 1$ does not occur at the first edge wave node ($\chi_b = 1.5$), nor is there any indication of nodal structure at higher χ_b. Additionally at the nodes π phase jumps occur in the surf zone mechanism,

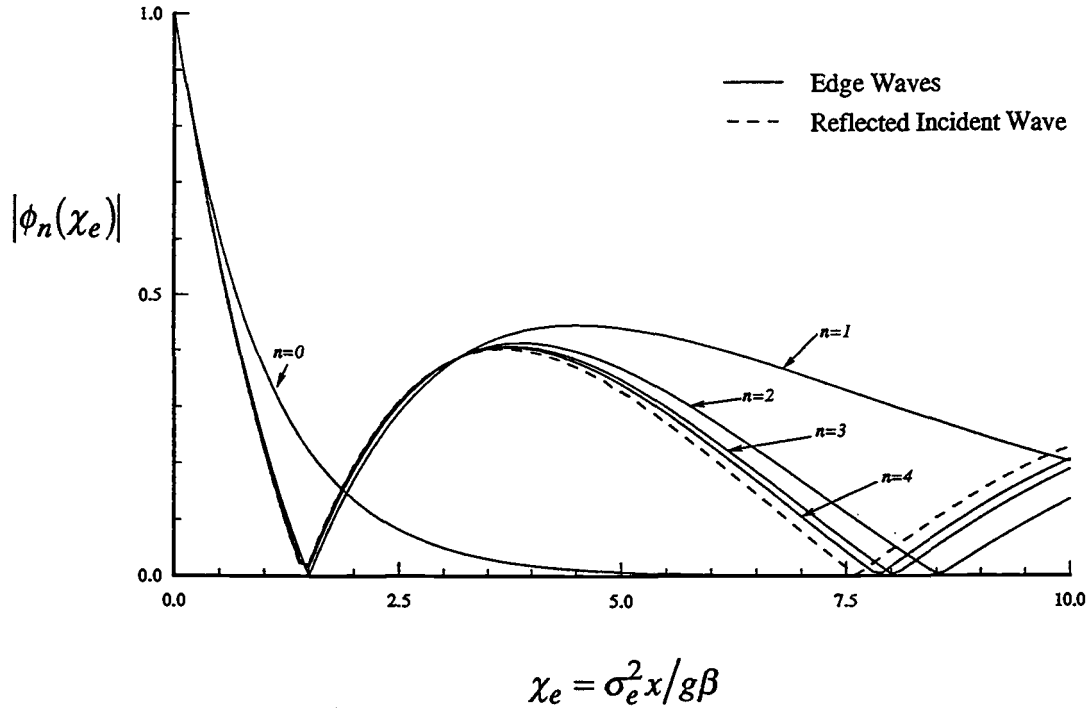

Figure II.8. Absolute value of the edge wave cross-shore behavior, $\phi_n(\chi_e)$ (Eq. II.8; Figure II.1), for the first 5 edge wave modes, plotted as a function of $\chi_e = \sigma_e^2 x/g\beta$. The range in χ_e plotted, $\chi_e < 10$, corresponds to typical surf zone conditions observed in nature. The shape of $|\phi_n(\chi_e)|$ is proportional to the variance of edge waves.

but not in the offshore forcing. This result is due to integrating the forcing over a larger portion of the edge wave profile in the offshore region ($b_{\max} = 100$), and thus incorporating more of the edge wave variance across χ space (*i.e.*, $\chi_{\max} = b_{\max}\chi_b$). In the surf zone, the integration region is determined by the incident modulation which must be small ($\delta = 0.1$), and thus nodal points are strongly reflected in the growth rates. The effect of varying b_{max} and δ is discussed more in section 4.

A further important point is that the vector sum growth rate is sometimes less than for either the offshore or the surf zone mechanisms individually, similar to the behavior of the S_{ij} forcing presented earlier (Figure II.6). Essentially the added structure in the total growth rate is a result of cancellation at certain χ_b due to the opposite (π) phase relationship between the two mechanisms. This is most notable for mode 1, shown again in Figure II.9 with the offshore, surf zone, and total growth rates and phases overlayed on the same graph. The new minimum at $\chi_b \approx 5.3$, which does not occur in either component individually, arises from the π phase difference between the two forcing regions. Thus, combining the offshore and surf zone contributions provides an additional frequency selection mechanism not occurring in either region separately.

The effect of α_o on growth rates is shown in Figure II.10 for $n = 1$ with $\alpha_1 = \alpha_2 = 1°$, 10°, 30°, and 45°. The effect of α_o is small for the extreme directional range investigated, particularly for $\chi_b <\sim 2.0$. At higher χ_b the affect is larger, ranging about a factor of 5 from 1°-45°. Interestingly, increases in α_o tend to smooth (reduce structure) and decrease the total growth rate. This is again a consequence of the π phase relationships in S_{ij} (Figure II.4), which reduces the total forcing contributions for the growth rate integral. The effect is greatest in the surf zone mechanism because the opposing S_{ij} components are the most energetic, S_{xx} and S_{xy}. In the offshore region S_{xx} and S_{yy} are nearly in phase (for $\chi_b >\sim 3.0$) and thus add to dominate S_{xy} (~π out of phase), thus limiting the influence of α^o on total edge wave growth in this region.

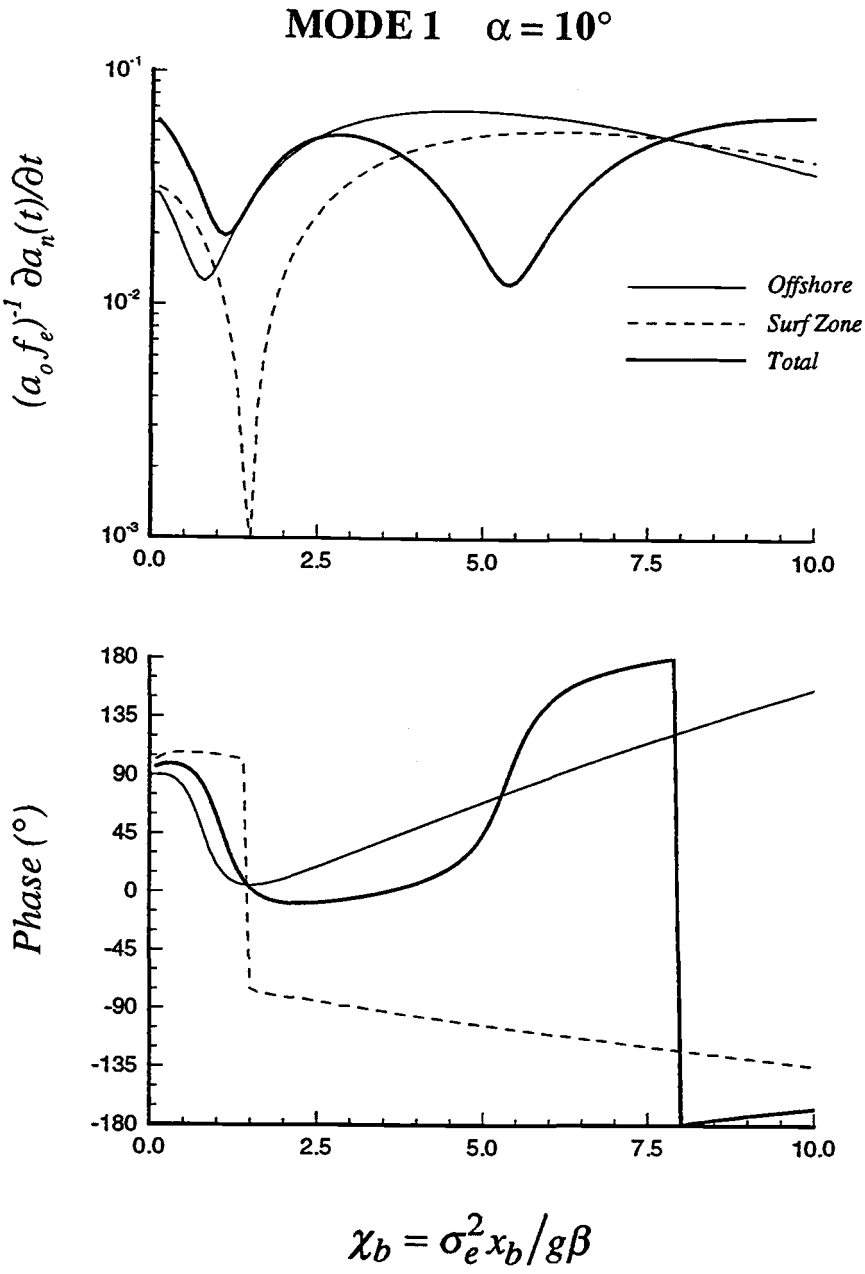

Figure II.9. Normalized growth rate for mode 1 edge waves, with $\alpha_1^o = \alpha_2^o = 10°$, for the offshore (Eq. II.31), surf zone (Eq. II.41), and total forcing plotted as a function of $\chi_e = \sigma_e^2 x / g\beta$. Growth rate amplitudes are shown in the upper panel on a log scale and the phase in the lower panel on a linear scale. Because of the phase relationship in the forcing between the two regions, the summation inputs structure into the total growth rate, suggesting an additional frequency selection mechanism.

Figure II.10. Normalized initial growth rate magnitudes (upper) and phases (lower) for the offshore (left panel; Eq. II.31), surf zone (middle panel; Eq. II.41), and total (right panel) mode 1 forcing as a function of incident wave angle ($\alpha_1 = \alpha_2 = 0°$, 10°, 30°, and 45°), plotted as a function of $\chi_b = \sigma_e^2 x_b / g\beta$. Amplitudes (non-dimensional) are plotted on a log scale and phases (degrees) on linear scale. Results are shown for $\beta = 0.01$, $\gamma = 0.42$, $\delta = 0.1$, $x_b = 100$ m, and $b_{max} = 100$.

Mode 1 Growth Rates as a Function of α

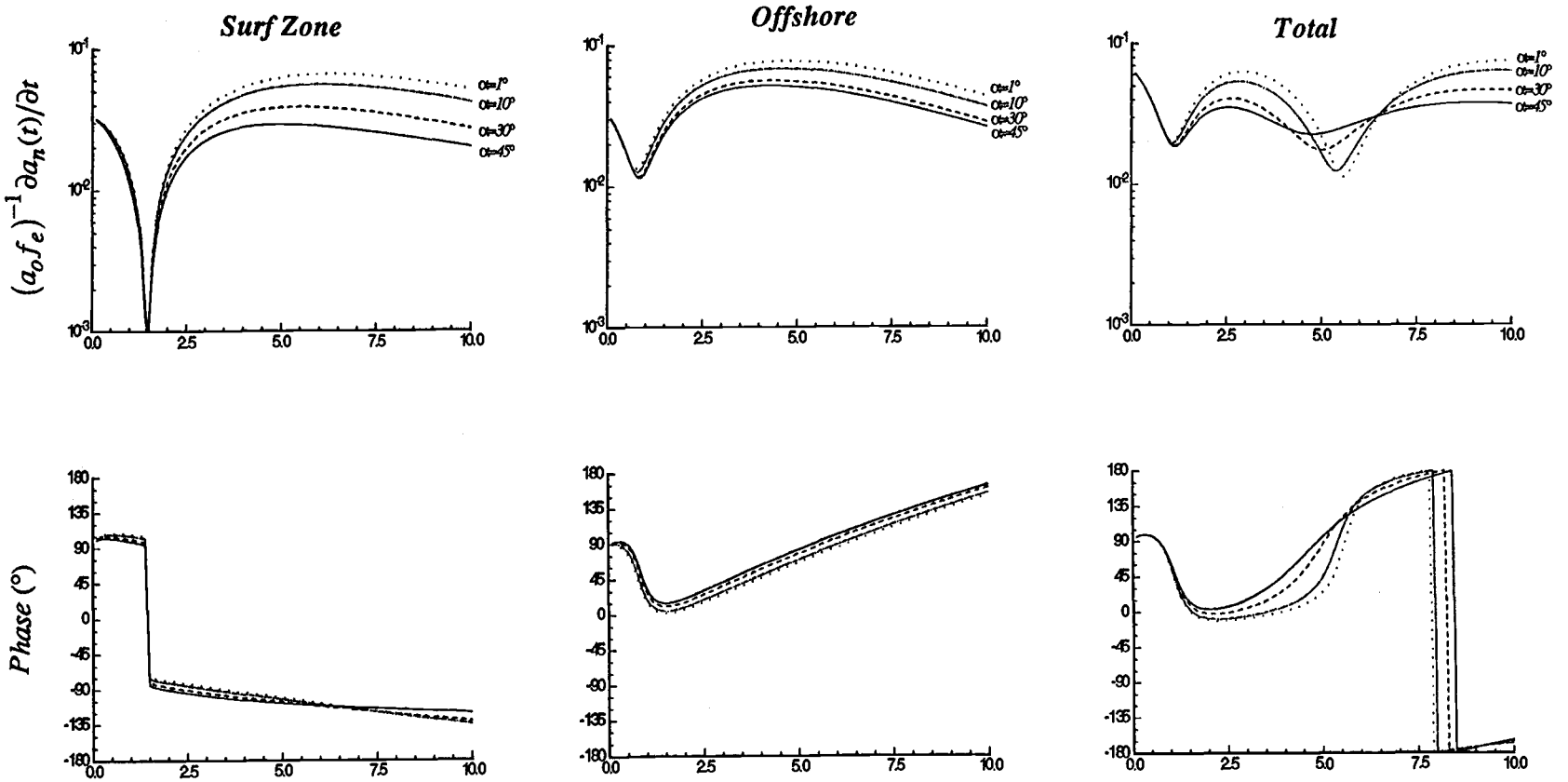

$$\chi_b = \sigma_e^2 x_b / g\beta$$

DISCUSSION

Growth Rates

The predicted growth rates for the case of phase-locked forcing by deterministic wave trains is not unrealistic if we expect this mechanism to provide reasonable forcing of progressive edge waves under the stochastic forcing conditions found in nature (Holman, 1981). The same type of result arose in the study of energy transfer into internal gravity waves from surface wave packets. An initial study of Watson *et al.* (1976) showed a very strong forcing for the phase-locked case. However, Olbers and Hevterich (1979) redid the problem for a stochastic surface wave field and found the strength of the forcing to be several orders of magnitude weaker than predicted by Watson, *et al.* This suggests that our predicted growth rates are higher than can be expected in nature, but possibly places an upper bound (time constraint) on edge wave growth.

As indicated by the growth rate equations (II.31) and (II.41), the behavior of the forcing with various parameters turns out to be quite simple. The surf zone growth rates vary with χ_b in a way which largely follows ϕ_n. In the offshore region, the influence of mode number on actual rates is largely through the variance distribution of ϕ_n in χ space. That is, the rate of transferring energy from the incident field appears to be about the same for all modes, where in fact for higher modes the energy must be spread over a larger cross-shore distance. The effect in the surf zone is reduced since the limits of integration are much smaller in this region.

This paper deals theoretically with the strength of resonant edge wave forcing due to the difference interaction of a bichromatic incident wave field. Yet in natural situations incident wave fields are distinctly not bichromatic but rather consist of a spectrum of energy. Although complete resonance is unlikely in nature, near resonance can occur for particular frequencies, particularly in narrow banded wave fields (Bowen and Guza, 1978;

Holman, 1981; Holman and Bowen, 1982). Bowen and Guza (1978) discuss the implications of this resonant restriction and show that for narrow-beam incident swells some frequency selection, with a strong modal dependence, may be expected.

Offshore Lower Limit of Integration

In the region $x_1 \leq x_b \leq x_2$ the limits of integration are determined by the maximum and minimum break points (Eq. II.32; Figure II.2). However, outside the surf zone, $x > x_b$, we have assumed that the lower limit of integration is constant and taken at the mean breaker position, $\overline{x_b}$. Thus in the offshore region we have integrated the exterior forcing along $\overline{x_b}$ rather than along the contour of the breaker position defined in ψ_e space. The situation is shown graphically in Figure II.11. Essentially we have assumed that forcing in area I exactly balances the contribution from area II, and have not considered the possibility of wave shoaling by non breaking waves in area I. If the forcing region is relatively narrow (δ small), this is a very good approximation. If it is large the waves in area I will have already moved into shallower water and the height difference will become significant. An error occurs proportional to the difference in mean wave height in areas I and II.

The analogy is with set-down and set-up. Immediately outside the break point (in the shoaling region) second order forcing is relatively small compared to forcing inside the break point. That is $a^2 \approx h^{-1/2}$ in the shoaling region (Eq. II.26; *c.f.* Longuet-Higgins and Stewart, 1962) whereas $a^2 \approx h^2$ in breaking waves (Eq. II.29; Thornton and Guza, 1982). As the total value of this forcing is not very large, differences are even less significant and the approximation should be more than adequate for a first order estimate of the forcing.

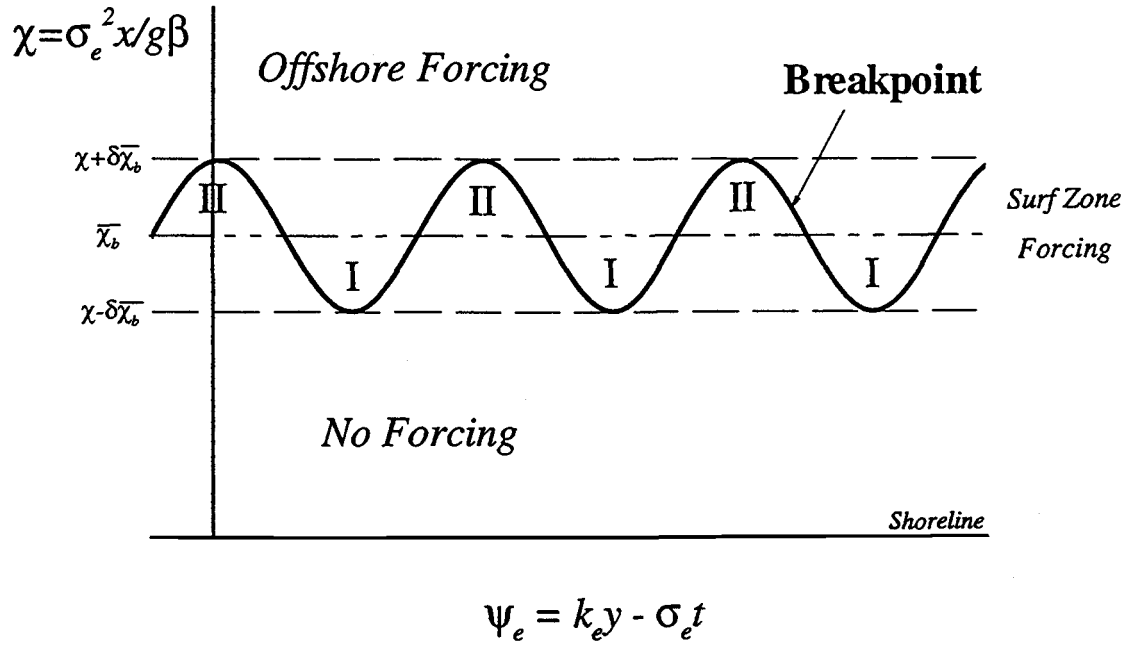

Figure II.11. Graphical representation of the edge wave forcing regions relative to an oscillating surf zone width. The vertical axis is $\chi_e = \sigma_e^2 x/g\beta$ and the horizontal axis is $\psi_e = k_e y - \sigma_e t$. The offshore forcing region is from the mean break point, $\overline{\chi_b}$, to deep water. Inside the minimum break point, $\chi - \delta\overline{\chi_b}$, no forcing occurs. The range of forcing by a modulating break point position is a function of incident wave modulation, δ. The region where waves are alternately shoaling and breaking (between $\overline{\chi_b}$ and the oscillating breaker line) are labeled I and II, respectively.

Sensitivity to Model Parameters

The dependence of growth rates on $\overline{x_b}$, β, and σ_e is essentially combined into the non dimensional scaling parameter χ (Eq. II.9). Thus, measured spectra (*i.e.*, current velocity) obtained in the field can be interpreted in terms of sampling position and lowest order profile characteristics. The effect of varying any particular combination of parameters is easily deduced. Additionally, because the forcing is dominated by S_{xx} components of the radiation stress, incident wave angles have little influence in the final growth rate, although for low modes and steep angles of incidence S_{xy} and S_{yy} components can be significant.

In the model $\gamma = 0.42$ is assumed constant, consistent with field data (Thornton and Guza, 1982; Sallenger and Holman, 1985), and enters the growth rate equations (II.31) and (II.41) linearly. Since all reported values of γ are O(II.1), varying γ does not significantly influence the final results. Thus, the formulation of the growth rate (in both the offshore and surf zone regions) is dependent on only one free parameter: the incident modulation, δ.

The effect of varying δ on growth rates is shown in Figure II.12 for a mode 1 edge wave with $\alpha_1 = \alpha_2 = 10°$. Values of δ plotted range from 0.01-0.5. In both the surf zone and offshore regions growth rates depend linearly on δ (Eq. II.31 and II.41). However, the response is greater for the surf zone mechanism because the limits of integration also depend on δ. Thus the overall surf zone response is quadratic in δ. In nature large incident modulations are not uncommon, and thus surf zone forcing might be expected to be more dominant over offshore forcing when $\delta >\sim 0.1$, as indicated in Figure II.12. However, in the formulation of the model we have assumed small δ so that incident wave travel times in the surf zone forcing region is short compared to time scales associated with the modulation, a point also made by Symonds, *et al.* (1982). Thus

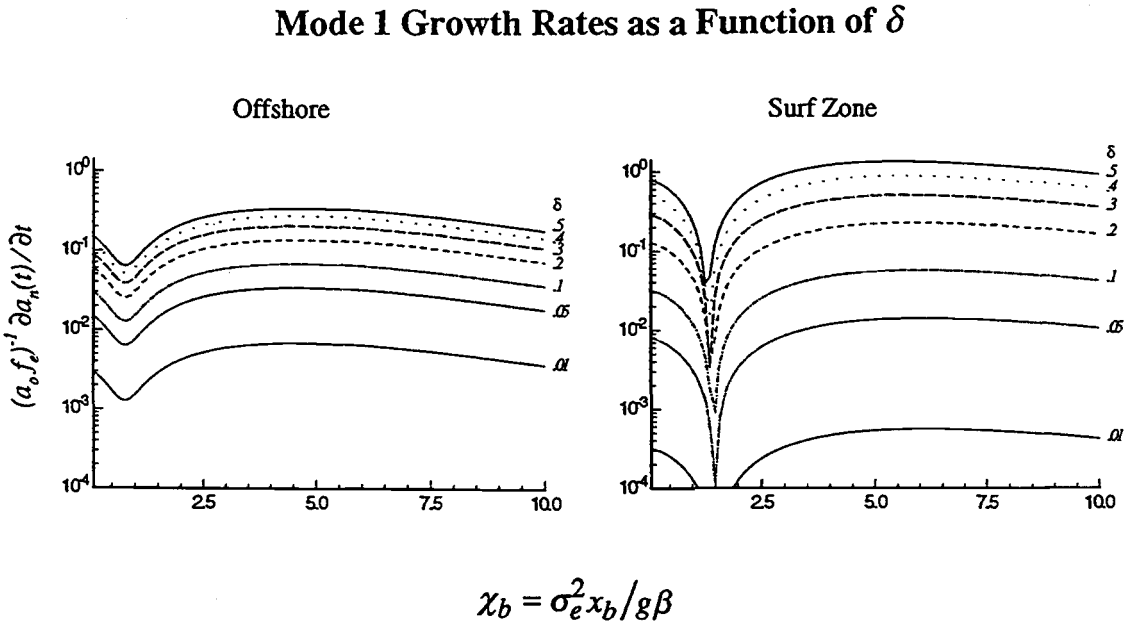

Figure II.12. Normalized growth rate magnitudes for a mode 1 edge wave for the offshore (left; Eq. II.31) and surf zone (right, Eq. II.41) regions for various values of incident amplitude modulation, δ, ranging from 0.01 - 0.5, plotted as a function of $\chi_e = \sigma_e^2 x / g\beta$. The offshore response is simply a linear function of δ, whereas the surf zone mechanism has a greater (quadratic) response because the limits of integration in this region also depend on δ.

allowing the modulation to get much larger than $\delta \approx 0.1$ is not accounted for by the model.

Also entering into the offshore formulation of growth rates is the upper limit of integration, x_{max}, which we have parameterized with b_{max}, the number of $\overline{x_b}$ offshore to integrate. The effect of varying b_{max} on the offshore growth rate is shown in Figure II.13 for both mode 1 and mode 4 edge waves, each with $\alpha_1 = \alpha_2 = 10°$ and $\delta = 0.1$. Results are computed over five orders of magnitude of b_{max}, ranging from 10^0-10^4. The surf zone growth rate for $\delta = 0.1$ is also shown for comparison.

For very small b_{max} the shape of the growth rate approaches the surf zone mechanism, with pronounced minima occurring at the location of nodes in ϕ_n (Figures II.1 and II.8). This arises because we are now integrating over a comparable χ range of ϕ_n, and thus details in ϕ_n strongly influence the growth rate integral. The magnitude of the offshore forcing, however, is much reduced. This is because the lower limit of integration is still fixed at the mean break point, and thus does not include modulations in the break point position nor forcing due to wave breaking which is expected to be much greater very near the surf zone (discussed previously).

As b_{max} increases, the influence of nodes in ϕ_n is greatly reduced, and the relative minima are displaced to lower χ_b. Furthermore, the results are virtually indistinguishable for $b_{max} >\sim 10^2$. Thus increasing b_{max}, for example to ∞, does not alter the growth rate integral for the low mode edge waves investigated (larger modes with greater cross-shore extent will require higher upper limits of integration). An additional point is that at very small χ_b , the results from the offshore and the surf zone mechanisms converge. This is because the integration takes place in χ space, so that for small χ_b, the range of integration for the two regions is comparable, even for large b_{max}.

Since we have neglected terms in (II.27) containing Λ (as being small compared to other terms), the forcing is independent of incident frequencies. In effect, incident

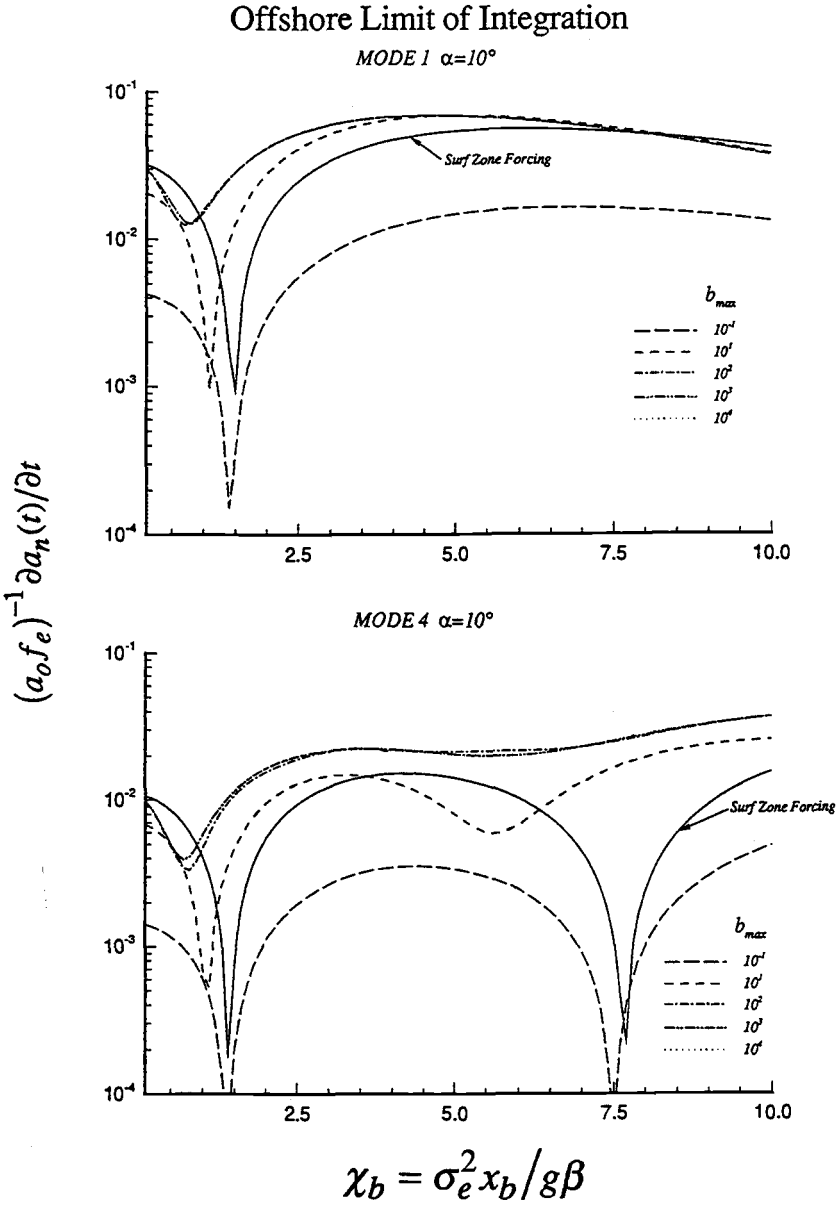

Figure II.13. Offshore growth rate amplitudes (Eq. II.31) for mode 1 (upper panel) and 4 (lower panel) edge waves for various values of the offshore limit of integration, $x_{max} = b_{max} x_b$ for b_{max} ranging from 10^{-1} - 10^4, plotted as a function of $\chi_e = \sigma_e^2 x / g\beta$. Also shown is the surf zone mechanism (solid line; Eq. II.41) for comparison. The legend for indicating different values of b_{max} is shown in the upper panel. As $b_{max} \rightarrow 0$ the shape of the offshore growth rate approaches the surf zone mechanism, although with a much reduced magnitude. The offshore curves are virtually indistinguishable for b_{max} greater than about 10^2. Results are shown for $\beta = 0.01$, $\gamma = 0.42$, $\delta = 0.1$, and $x_b = 100$ m.

frequencies serve only to provide a necessary σ_e-k_e interaction which matches the edge wave dispersion relation (Eq. II.10). Products in incident wave velocity potentials, $\Phi_1\Phi_2$ (Eq. II.23), have an $(X_1X_2)^{-1/2}$ dependence, which contain products of incident frequencies, $\sigma_1\sigma_2$. However, we have removed the dependence on incident frequencies in the formulation of $\hat{S}_{\alpha\beta}(\Phi_1\Phi_2)$ in (II.20) by choosing incident wave amplitudes relative to the break point, where by (II.26) products of $a_1^o a_2^o$ have an $\left(X_1^o X_2^o\right)^{1/2}$ dependence. Substituting (II.26) into (II.20) thus eliminates dependencies on $\sigma_1\sigma_2$.

Still, the resonsant response assumed in the model restricts incident wave pairs to difference frequencies (II.24) which satisfy the edge wave dispersion relation (II.10). Bowen and Guza (1978) discuss these resonant restrictions in terms of incident wave angles (*i.e.*, wavenumbers) and frequencies. They show that only a finite number of incident frequency pairs satisfy the resonant condition for narrow beam incident swell, thus placing a restriction on the possible (σ_1, σ_2) combinations which could theoretically excite edge waves.

Shallow Water Assumption

In (II.13) edge wave growth rates are integrated from the shoreline to infinity. Even though offshore growth rates are reasonably insensitive to the offshore limit of integration ($b_{max} >\sim 10^2$; Figure II.13), requiring the upper limit of integration in (II.15) to reach beyond shallow water clearly violates our initial assumptions, creating an internal inconsistency in the model.

In our formulation of the interaction radiation stress, the incident wave surface elevation is approximated by the shallow water bessel function solution for progressive surface gravity waves over a sloping bottom (Eq. II.21-II.23; Stoker, 1947). Inside the surf zone, this formulation seems very reasonable since the water depth is always shallow with respect to incident wave wavelengths and amplitudes are given as a function of the

local depth. Outside the surf zone, however, the use of the shallow water solution is only valid for a limited distance offshore determined by the beach slope, and depends on the incident wave wavelength (or frequency, equivalently). In the offshore region, (II.23) gives an $x^{-1/4}$ dependence on wave amplitude. Thus, products of incident wave amplitudes decay in this region as $x^{-1/2}$, whereas they should become constant in deep water. Magnitudes of offshore growth rates would thus be less than for actual intermediate water solutions.

The growth rate equation (II.15) also includes consideration of ϕ_n. Since ϕ_n decays exponentially offshore as a function of mode number (Eq. II.8; Figure II.1), the offshore integral for low modes is not biased significantly by reduced contributions in intermediate water. Therefore, when evaluating the model the upper limit of integration can be reduced for low sloping beaches without substantially underestimating the growth rate. This approximation is good for shallow beaches where edge wave length scales are small, as indicated by the inverse relationship of β and x in (II.9); for steeper beaches the application is questionable. This is also the case for low modes which have a relatively small offshore decay scale; for higher modes with larger decay scales contributions are more severely biased.

Comparison with Foda and Mei (1981)

Foda and Mei (1981) consider the problem of long waves generated by a normally incident swell which has a small alongshore variation which is fixed in space, but has a slow modulation in time. This variation in wave height could be thought of as two incident waves of the same frequency approaching the beach from equal but opposite angles to the normal. The modulation is then the beat frequency between these waves and the normally incident wave. This is therefore a rather particular case of the general problem which we are considering. Their discussion was limited in that the dominant

(largest) wave is normally incident. However, Foda and Mei have carried through a very sophisticated analysis which includes results for the case where the long waves grow to magnitudes of the same order as the incident modulation. They can therefore discuss the processes that eventually limit edge wave growth. However, the complexity of the calculation rather precludes any simple interpretation of these results.

A further complication is that, for the case of breaking waves, Foda and Mei have used a doubtful representation of the breaker condition in which the break point is constant, and the perturbation amplitude (modulation) extends to the shoreline. The variation in breaker position due to the changing wave conditions is ignored. In affect Foda and Mei assume that γ is always larger when the incident waves are large. Recent field evidence (Guza and Thornton, 1982; Sallenger and Holman, 1985; Holman and Sallenger, 1985) suggests that γ is reasonably constant for any particular beach and the position of the breaker is the property that varies as a function of incident wave height. This is a central point in our calculation.

Foda and Mei also compute growth rates for the interaction which vary over two orders of magnitude as a function of the parameter

$$\overline{\Omega} = \frac{\sigma_e}{\beta \sigma_i} \tag{II.42}$$

This parameter arises from a particular scaling which is not the natural scaling for the shallow water profile we have considered. As a consequence Foda and Mei have computed values of $\overline{\Omega}$ which seem rather small, ranging from 1-3. If we consider a 60 second beat, 10 second incident wave, and slope of 1:50, then $\overline{\Omega} \approx 8$. As growth rates increase very rapidly with $\overline{\Omega}$ in Foda and Mei's results we might expect very large growth rates for values typical of open coast beaches. However, precise values can not be

compared due to their very difficult (4th order) representation of the forcing inside the surf zone.

Comparison with Schaffer (1990)

Schaffer (1990) considers the problem of long waves generation by wave groups, and demonstrates the possibility of three dimensional infragravity waves by including off normal angles of incidence. Schaffer considers a plane sloping beach connected to a flat shelf at some depth outside the break point, and allows for both fluctuations in surf zone width and incident wave modulations inside the break point.

Outside the break point incident wave amplitudes are determined from conservation of wave energy flux referenced to some offshore position. Inside the break point wave height is given as a constant proportion of the depth (as in this study). Break point positions are found by matching offshore conditions to the surf zone condition, in which

$$|A|^2 = \gamma_o^2\left(1+\delta^2+(1-\kappa)2\delta\cos 2\theta\right)h^2 \qquad \text{(II.43)}$$

where $$\theta = \int_{const.}^{x_b} K_x dx + k_e y + \sigma_e t$$

and where K_x is the cross-shore component of the difference wave number, and γ_o is chosen so that A is continuous at the fixed break point. κ is an adjustable parameter ranging from 0-1 which specifies the amplitude modulation characteristics inside the break point. In the limiting case where $\kappa \to 1$ the break point position fluctuates and no incident wave amplitude modulation inside the break point exists (essentially the case we are investigating). At the other extreme $\kappa \to 0$ the break point is fixed and incident modulations progress all the way to the shoreline (as in Foda and Mei, 1981). Break point positions are given (to first order in δ) by

$$x_b \approx \overline{x_b}(1+\delta\kappa\cos\theta) \tag{II.44}$$

which when $\kappa = 1$ is our representation of the break point position (Eq. II.37).

In their formulation the forcing is parameterized using the general linear form (lowest order Stokes theory) for the radiation stress following Mei (1983)

$$S_{ij} = \frac{\rho g}{2}|A|^2\left\{\left(\frac{c_g}{c}-\frac{1}{2}\right)\delta_{ij}+\frac{c_g}{2c}\begin{bmatrix}2\cos^2\overline{\alpha} & \sin 2\overline{\alpha}\\ \sin 2\overline{\alpha} & 2\sin^2\overline{\alpha}\end{bmatrix}\right\} \tag{II.45}$$

where A is a complex amplitude describing the modulation of the incident waves, c_g is the group velocity, c is the phase velocity of the incident waves, and $\overline{\alpha}$ is the mean local wave angle. In their formulation $\overline{\alpha}$ is chosen at some offshore location where the two incident wave trains have a common angle of incidence. Schaffer solves the momentum equations numerically without specifying the exact case of resonance, hence he is able to predict the forced infragravity surface elevation profile. This formulation of the model represents the principal difference from our work.

The radiation stress in (II.45) is expanded in a Fourier Series and second derivatives (as in Eq. II.6) are computed. Fluctuating break point positions for the surf zone forcing mechanism are represented in a similar analysis as in our work, although Schaffer parameterizes modulations in (II.45) through variations in incident amplitudes. This is in contrast to our work where we have referenced the incident amplitudes and wave angles to a fixed value (taken at the mean break point), and allowed the radiation stress to modulate on time and space scales determined by the nonlinear difference interaction of two beating incident waves. Since the results in Schaffer do not explicitly include resonance (as is considered herein), growth rates are not considered. Furthermore, since the model is complicated by a matching condition at the break point, a simple straightforward comparison is not easily accomplished and is thus not pursued further.

CONCLUSIONS

A theoretical mechanism for driving resonant longshore progressive surface gravity wave motions in the nearshore (edge waves) is derived from the forced momentum balance equations. Forcing integrals are separated into offshore (outside the break point) and surf zone (at the break point) contributions. Both mechanisms are based on amplitude modulations which arise from an interacting bichromatic wave field. Surf zone forcing is derived from momentum fluxes induced by temporal and spatial variations in initial break point amplitudes, expressed for the plane beach case considered as three dimensional modulations in surf zone width (first suggested by Symonds, *et al.* (1982) who considered the two dimensional problem). The nonlinear forcing is provided by the unbalanced gradient in radiation stress, $S_{\alpha\beta}$. Following Phillips (1977), a general form for $S_{\alpha\beta}$ due to the nonlinear difference interaction of two incident waves approaching the beach at an angle is derived.

The model indicates that the cross-shore component of onshore directed momentum flux, S_{xx}, usually dominates over S_{yy} and $2S_{xy}$, particularly for small angles of incidence, higher edge wave modes, and lower frequencies. The effect of wave angle is relatively small for higher modes due to the dominance of S_{xx} in the forcing. Interestingly, increasing incident wave angle tends to reduce the overall growth rates for all modes because of the relative phase relationships of the forcing components.

Growth rates predicted by the two mechanisms have similar dependencies. A notable exception is that the offshore mechanism is linearly proportional to the incident wave modulation, whereas the surf zone mechanism has a quadratic dependence. Edge wave response is only weakly dependent on wave angle, a result of the dominance of S_{xx} terms in the forcing. Increasing wave angles also tends to reduce growth rates because of the phase relationships of the $S_{\alpha\beta}$ forcing terms.

The strength of the surf zone generation mechanism is found to be comparable to offshore forcing proposed by Gallagher (1971), who intentionally excluded forcing due to breaking phenomena. Thus the surf zone component of the forcing can not be neglected, and under some conditions could actually dominate. The strength of the growth rates in the two regions have similar dependencies, where magnitudes are inversely proportional the edge wave mode numbers and directly proportional to the incident wave modulation. Edge wave response is only weakly dependent on wave angle, a result of the dominance of S_{xx} terms in the forcing. Initial growth rates are predicted and found to be quite rapid, with edge waves amplitudes growing to incident wave amplitudes on the order of 10-20 edge wave periods, much faster than other model predictions (*e.g.*, Foda and Mei, 1981). However in nature frictional damping and directional distribution due to the stochastic behavior of real ocean waves will reduce these rates by an unknown amount.

Finally, the total forcing mechanism including both offshore and surf zone contributions introduces structure into the infragravity band of the forcing spectra, and with restrictions introduced by discrete resonances of the system, provides a frequency selection mechanism necessary for the generation of nearshore sand bars. However, because we have not included viscous damping, apriori relationships of edge wave response after a finite time period is not justified.

ACKNOWLEDGEMENTS

This research was sponsored by the National Science Foundation under contract OCE-8007972-01, and by the Office of Naval Research under grant number N00014-90-J1118. The research addressed in this study was first postulated by Tony Bowen and Rob Holman, who originally formulated the parameterization of the interaction radiation stress.

CHAPTER 3

Phase Speed and Angle of Breaking Waves Measured with Video Techniques

ABSTRACT

The phase speed and incident angle of breaking surface gravity waves in the surf zone are measured using video processing techniques. The analysis of video data follows two lines. The first focuses on the time series of image intensity at points corresponding to known surf zone locations, and comparisons with *in situ* pressure gages. Celerity spectra of video and pressure data from a single location show similar results. Wavenumber spectra at the peak frequency from two longshore arrays of intensity time series compares favorably with similarly spaced current meter data. The second part of the analysis focuses on individual waves. A method for identifying breaking waves with video is presented. Analysis of travel-time of individual breakers estimated from 2 pairs of spatially separated sensors in an orthogonal array is done in both the time domain, using the cross-covariance function, and the frequency domain, via the phase spectrum. Phase speeds and wave angles of individual waves are then computed using the time lag and sensor separation. Results are similar for each method. Mean values of phase speeds and wave angles are consistent with first order shoaling theory.

INTRODUCTION

The nearshore coastal zone is generally a wave dominated environment. It is therefore not surprising that models used to describe sediment transport in the nearshore are largely based on breaking surface gravity waves and the stresses they exert on the bottom sediment. Mechanisms for sediment transport under waves have been studied for many years, and the problem has proven to be quite complex. Although researchers have become adept at measuring the wave field (primarily pressure and bi-directional current velocity) at a particular point, and in some instances the suspended sediment concentration, the need for new sampling and analytical techniques is becoming more apparent. In particular, logistical difficulties of sampling over the naturally large scale of complex topographies have been great.

There are two basic types of sediment transport models which predict the shape of beach topography: those describing cross-shore sediment transport (*e.g.*, Bagnold, 1963; Bowen, 1980) and those which look at the alongshore littoral drift (*e.g.*, Komar and Inman, 1970). The cross-shore models are based primarily on sediment transport mechanics on an integrated wave-by-wave basis, focusing attention on the orbital velocity of the wave raised to some power, and on the convergence and divergence of drift velocities associated with different wave-induced phenomena, such as edge waves and undertow. The longshore models rely more heavily on the net, or bulk movement of sediment, driven largely by the mean circulation or longshore current. For each model type the importance of various wave parameters are predicted; commonly included is the phase speed and breaking wave angle. Our primary motivation lies in the dependance of theoretical expressions for wave-induced momentum fluxes, mean longshore currents, and alongshore sediment transport on phase speed and wave angle.

We present a method for measuring the phase speed and wave angle of individual breaking waves and bores. The technique is based on the premise that the foam and

bubbles at the crest of breakers is bright in contrast to the darker unbroken surrounding water, and provides a means for distinguishing breaking from non-breaking waves. The passage of breaking wave crests is identified by a local maximum in image intensity that is recorded with video and accessed with a computerized image processing system. This method is similar in principle to the traditional method of visually identifying the passage of breaking waves past a surf zone sensor (*e.g.*, Thornton and Guza, 1983).

The analysis will follow two lines. The first focuses on the time series of video intensity. Ground truth comparisons are made with pressure data from the same surf zone position, and from pairs of "sensors" separated a distance in the cross-shore direction. Celerity spectra from video and pressure data are compared, as are mean wave angles estimated with two longshore arrays of video and current meter data. The second line of analysis focuses on the measurement of phase speed and wave angle of individual waves. A method for identifying breaking waves using a variable thresholding method is presented. Analysis is done in the time domain, using the cross-correlation function, and in the frequency domain, via the phase spectrum. Comparisons between the two methods are presented, as is a qualitative assessment of the results with regard to simple shoaling ideas.

The first section summarizes our theoretical motivation and expectations. The following section describes the methods for computing time lags and estimates of phase speed and wave angle. The field study (DELILAH experiment) and sampling methods for collecting the raw data are described next. Results are then presented for the time series analysis and the individual wave methods. Finally, results are discussed and summarized.

THEORETICAL MOTIVATION

Models which rely on the momentum flux induced by breaking waves depend on the phase speed, C, and wave angle, α. For example, Thornton and Guza (1986) show the gradient of the cross-shore flux of longshore directed momentum, or radiation stress, S_{xy}, is given by

$$\frac{\partial}{\partial x} S_{xy} = \frac{\sin \alpha_o}{C_o} \langle \varepsilon_b \rangle \tag{III.1}$$

where $\langle \varepsilon_b \rangle$ is the local ensemble-averaged energy dissipation due to wave breaking and provides the thrust necessary to drive nearshore flow. Thornton and Guza then show how (III.1) relates to the mean longshore current,

$$V = \frac{1}{\rho c_f |\tilde{u}|} \frac{\sin \alpha_o}{C_o} \langle \varepsilon_b \rangle \tag{III.2}$$

where ρ is density of water, $|\tilde{u}|$ is the total instantaneous velocity, and c_f is the bed shear stress coefficient.

Other models predicting the mean longshore transport have been based on what has been referred to as the "longshore component of wave energy flux", also a function of C and α,

$$P_L = (ECn)_b \sin \alpha_b \cos \alpha_b \tag{III.3}$$

where ECn is the wave energy flux, and the subscript b indicates that the parameter is to be evaluated for the breaking waves. (III.3) is proportional to the volumetric transport

rate, Q_s, and is shown by Komar and Inman (1970) to be a useful predictor of the immersed weight transport rate (Bagnold, 1963)

$$I_L = K(ECn)_b \frac{\overline{V}}{u_m} \tag{III.4}$$

where u_m is the maximum orbital velocity, K is a non-dimensional constant, and $\overline{V}$ is proportional to P_L.

Measurements of the transport rate (III.4) and its relationship to the forcing terms has varied widely, partly due to the accuracy in measuring the parameters (Komar, 1991). We hope to provide an alternative, low cost method that will allow further model testing as well as relatively easy monitoring for these dynamically important variables.

Shoaling Expectations

The first order approximation of phase velocity is

$$C = \frac{g}{\sigma}\tanh(kh) \tag{III.5}$$

where h is the local water depth, σ and k are the radian frequency and wavenumber, and g is acceleration of gravity. In shallow water, (III.5) reduces to simply a function of depth, $C = \sqrt{gh}$, which is independent of frequency. Considering simple bore theory, or similarly the asymptotic shallow water form of Cnoidal theory (solitary wave theory), which includes amplitude dispersion, the phase speed of the wave is given (to lowest order) by

$$C = \sqrt{g(h+H)} \tag{III.6}$$

where H is the height of the wave. Since we are assuming shallow water, (III.6) is also seen to be frequency non-dispersive. It should be noted that these theories work well for frequencies satisfying the shallow water criteria, but lose validity in intermediate depths.

Snell's Law for wave refraction predicts that waves will tend toward a more normal angle of incidence when propagating into shallower water,

$$\frac{\sin\alpha}{C} = \frac{\sin\alpha_o}{C_o} \tag{III.7}$$

where α_o and C_o are the offshore estimates of wave angle and speed, and α and C are the inshore estimate. Thus, waves approaching the coast at a steep angle of incidence will gradually refract toward the normal, and is a common observation in the tracking of individual crests. For narrow banded wave fields, the mean wave angle of incidence at progressively shallowing depths should also show this affect.

Estimating Time Lags

Measurement of the phase velocity of progressive waves with pairs of spatially separated sensors depends on the estimate of the time it takes the wave to pass between sensors. The resolution in phase speed will then depend on the accuracy of the travel time estimate. Time lags may be computed in either the time domain or the frequency domain. In the time domain, the cross-covariance of two stationary random processes at time lags, τ, is determined from the cross-covariance function, $R_{xy}(\tau)$

$$R_{xy}(\tau) = \mathrm{E}[x_k(t)y_k(t+\tau)] \tag{III.8}$$

where x_k and y_k are two time series, and E[] indicates expected value (Bendat and Piersol, 1986). The lag at which the maximum correlation occurs, τ_o, is the mean travel time of the wave over the distance separating the sensors. This technique has a resolution proportional to the sampling interval, Δt.

In the frequency domain, mean time lags are manifested as a linear trend or ramp in the phase spectrum. The time lag estimated from the phase spectrum is computed using the method described by Bendat and Piersol (1986). For a given length of time series, the slope of the phase spectrum is proportional to τ_o,

$$\phi_x(f) \approx 2\pi\tau_o f \tag{III.9}$$

The determination of τ_o is derived from $R_{xy}(\tau)$. For the cross-covariance function to be a maximum the derivative of $R_{xy}(\tau)$ with respect to τ must be equal to zero. Bendat and Piersol then show that

$$\frac{\partial R_{xy}(\tau_o)}{\partial \tau_o} = 0 = -\int_0^\infty 2\pi f \left| G_{xy}(f) \right| \sin\left[2\pi f \tau_o - \phi_{xy}(f)\right] df \qquad \text{(III.10)}$$

where $G_{xy}(f)$ is the gain spectrum (dependant on the coherence spectrum). Since, by (III.9), the argument in (III.10) is nearly zero, the sine of the argument can be replaced by just the argument. Solving for τ_o yields

$$\tau_o = \frac{\int_0^\infty 2\pi f \left| G_{xy}(f) \right| \phi_{xy}(f) df}{\int_0^\infty (2\pi f)^2 \left| G_{xy}(f) \right| df} \qquad \text{(III.11)}$$

The resolution of the time lag estimate in (III.11) is expected to be better than that from the time domain method, simply because the spectrum takes into consideration all the frequency content of the series. This implies that the shape of the spectrum is similar at each spatial position used in the calculation, which may not be true for rapidly transforming waves. However, individual frequencies are weighted by the gain function to give higher importance to those frequencies with higher coherence. Thus, the method does not assume that the form of the wave remain constant, although, the technique does require that the peak frequency does not change, only allowing the harmonics to differ.

Phase Speed and Wave Angle Estimation

Phase speed and wave angles of individual waves are computed by first defining the slowness, S, the inverse of the phase velocity, as simply the time lag (computed above) divided by the distance separating the sensors, Δx,

$$S = \frac{\tau}{\Delta x} \qquad \text{(III.12)}$$

The phase speed magnitude, $|C|$, and wave angle, α, are then found using the orthogonal components of (III.12)

$$|C|^2 = \frac{1}{S_x^2 + S_y^2} \quad , \quad \alpha = \arctan\frac{S_x}{S_y} \tag{III.13}$$

This method works well when the distance separating the sensors is not so large that the coherence of the wave becomes statistically insignificant. The error in the phase velocity estimate depends on the errors in the slowness (III.12). From (III.12) the resolution of the slowness is given by

$$\frac{\Delta S}{S} = \frac{\Delta T}{T} - \frac{\Delta L}{L} \tag{III.14}$$

where L is the distance between sensors, ΔL is the error in L (for our application taken to be equal to the pixel resolution in the image, described later), T is the time lag that it takes the wave to travel the distance L, and ΔT is the error in the time lag estimate. Thus, the magnitude of the error in S is due to both image and time lag resolution. Since for constant sensor position the uncertainty due to image resolution will be constant, most errors will arise from the estimate in time lag.

Using a mean phase speed of 5 m/s corresponding to a sensor separation of 5 m (implying a mean lag of 1.0 seconds), a pixel resolution of 0.10 m, and an error in mean lag of 0.10 sec, the error in phase speed is 8%. This is, of course, assuming a coherence of 1.0. If the coherence is not equal to 1.0 then the uncertainty would be greater and primarily reflected in the estimate of travel time.

FIELD METHODS

The data were collected as part of the DELILAH experiment, held at the Army Corps of Engineers CERC Field Research Facility (FRF) on the Outer Banks of North Carolina near the village of Duck, in the fall of 1990. The sampled area ranges from the dune crest to 200 m offshore, begins approximately 180 m north of the FRF research pier and extends north ~200 m. A description of the general beach conditions at Duck is given by Birkemeier, *et al.* (1985).

Video data were collected using up to eight cameras simultaneously, each looking over a particular region of the study area. One camera view providing sufficient coverage of the entire study area was used in the following analysis. Image intensity is sampled at 10 Hz for 2 hour records. The time series data were resampled at 8 Hz (using a cubic spline interpolation) to allow best comparison with other surf zone instrumentation.

Video tapes of surf zone wave breaking are digitized at a rate of 30 Hz by an image processing system in a SUN4/110 host computer. Locations on the image of pixels (picture elements) corresponding to pre-determined ground coordinates are found from geometric transform equations using photogrammetric relationships (Lippmann and Holman, 1989). Spatial resolution at the desired location is a function of the field set up geometry and is determined using the method described in Lippmann and Holman (1989). The resolution from DELILAH ranges from 0.10 m (in the near field) to 0.5 m (further away from the camera). The time series data from video are in the form of non-dimensional image intensity units ranging linearly in value from 0 (totally black) to 255 (totally white), and are linearly adjusted to the full dynamic range using the minimum and maximum values in the image prior to sampling to improve contrast. Use of the image processing system to enhance image quality and dynamic range is described more fully in Lippmann and Holman (1989).

The data discussed in the text are from the October 12, 1990 near high tide (+0.71 m above NGVD) at 1600 EST, the evening prior to the expected arrival of Hurricane Lily. Directional spectra from a linear array of bottom mounted pressure sensors located at the 8 m depth contour indicated waves were very narrow banded in frequency and direction, with a peak incident frequency of 0.07 Hz and mean wave angle of -40 degrees from normal. The significant wave height (at the linear array) during the run was 2.18 m. Video data are compared with data from an *in situ* cross-shore array of strain-gage pressure sensors, as well as two longshore arrays of bi-directional current meters, one in the trough of the longshore bar and the other on approximately the seaward flank of the bar (see Figure IV.3). The pressure data have been corrected for atmospheric pressure prior to analysis and the spectra have been depth corrected using linear theory. All of the surf zone instruments were sampled continuously at 8 Hz.

RESULTS

Intensity Time Series

The use of video is only valid if intensity time series act as a coherent proxy to wave variables over the incident band; especially critical for our application is the phase relationship of the waves past successive instrument locations. Ground truthing is accomplished by comparing the video data with *in situ* pressure sensors. Figure III.1 shows a sample time series for both video and pressure data located in the mid surf zone on October 12. The data look quite similar in the relationship of peak wave position. The intensity record is slightly more skewed, alluding to the rapid increase and decrease in the passage of the breaking wave crest. The vigor of breaking is somewhat revealed in the decay scale of intensity signal after the passage of the wave crest. There are times when the pressure sensor detects waves which the video data does not, indicating that not all the waves are breaking.

The relationship between the intensity and pressure data is further shown with the cross-spectrum between pressure and video time series (Figure III.2). Both power spectra (upper panel) show very similar structure throughout the incident band. The strong relationship is confirmed by the high coherence (lower panel). It should be noted that most of the energy at higher frequencies (greater than the peak) in the video spectrum (as well as the pressure spectrum) is not derived from free waves, but instead are primarily harmonics necessary to describe the correct shape of the waves. Not too surprisingly, low frequency (non-breaking) waves are not well represented by the intensity records.

To test the ability of the intensity data to accurately represent the phase relationship of the progressive incident waves, cross-spectra have been computed between spatially separated intensity time series from the cross-shore array positions, and compared with

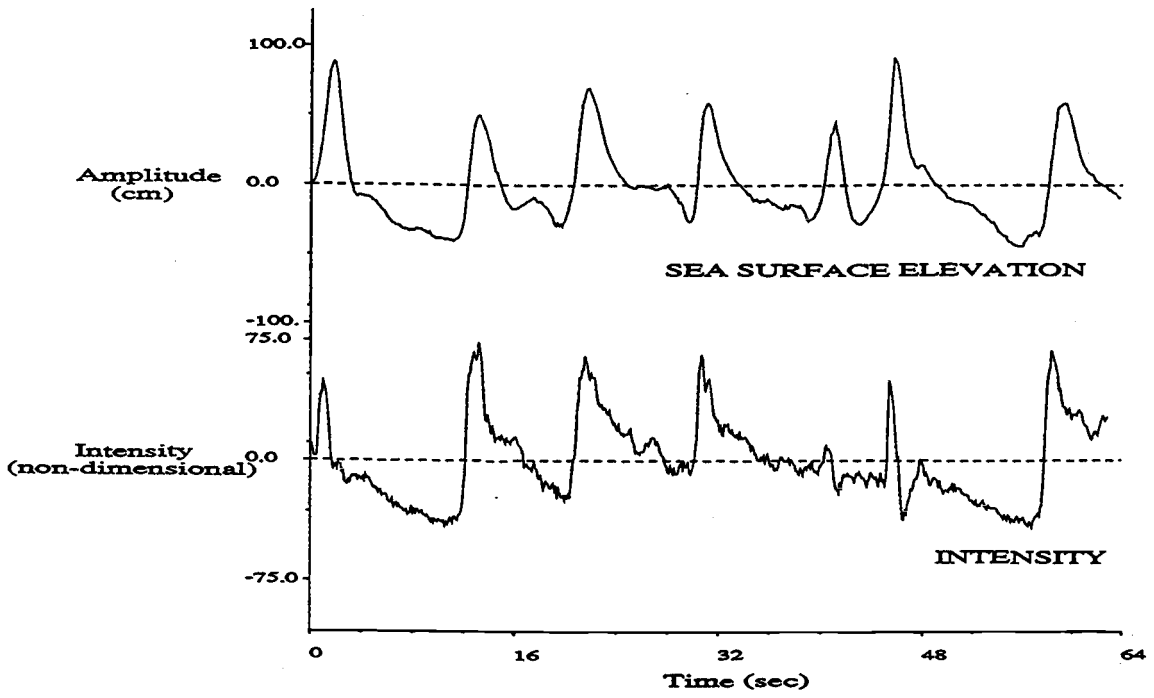

Figure III.1. Example colocated pressure (top) and intensity (bottom) time series from October 12, 1990.

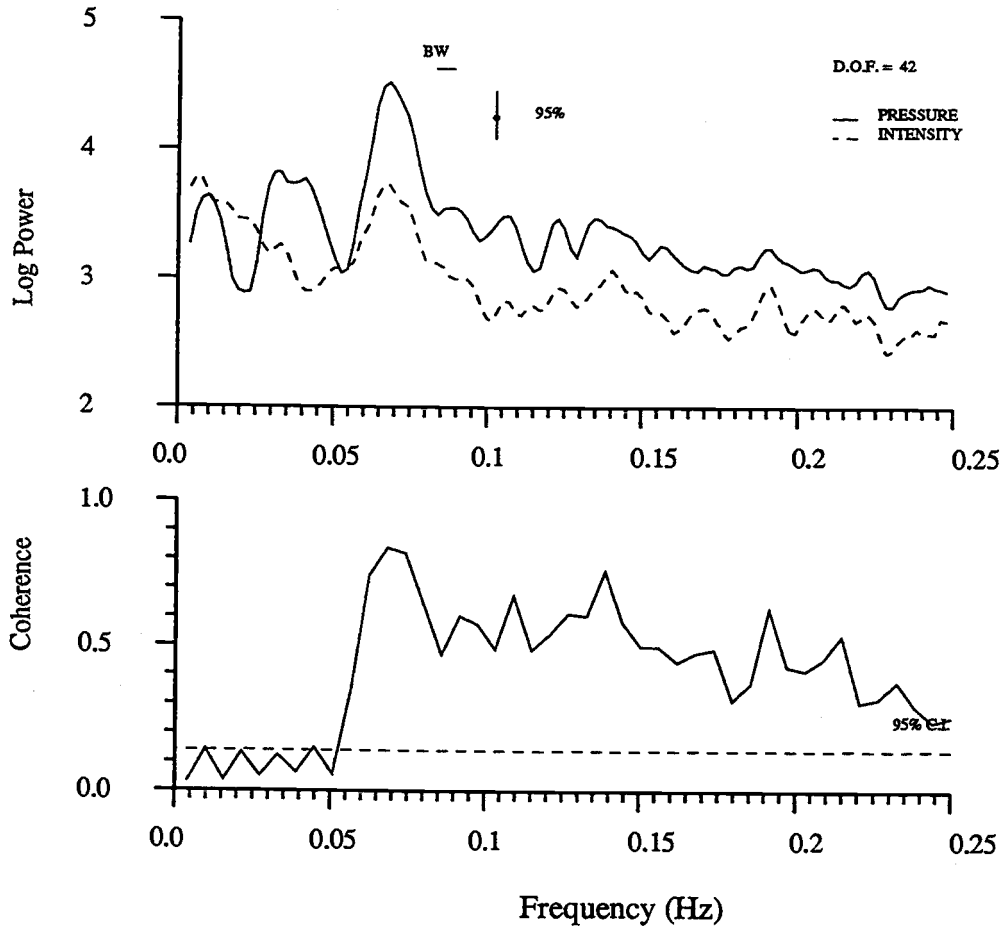

Figure III.2. Cross-spectrum between a video intensity time series and an *in situ* pressure gage from the mid surf zone. The power spectrum is shown in the top panel, and the coherence spectrum is shown in the lower panel. The power spectra for the pressure data (solid line) has units cm^2sec, whereas the intensity power spectra (dashed line) is non-dimensionally based. The spectra were calculated with 42 degrees of freedom.

that derived from two pressure gages. Figure III.3 shows the power spectra (upper panel), coherence and phase spectra (middle panels), and the celerity spectra (lower panel) for pressure data (left column) and video data (right column) sampled from sensor positions separated 18 m near the landward edge of the bar crest. The high coherence of the pressure data throughout the incident band indicates that the waves are passing each sensor. The positive linear ramp in the phase spectrum throughout the incident band well into the higher frequencies indicates the waves are propagating landward with a constant speed. This is confirmed by the constant celerity spectra (for frequencies greater than ~0.05 Hz).

The results for the video data are similar: high coherence throughout the incident band, a positive linear trend in the phase spectra, and approximately constant celerity greater than the peak frequency. It should be emphasized again that the pressure record sees all waves, breaking or non-breaking, whereas the video method sees primarily the breaking waves. The high coherence for the intensity records is at least partly attributable to the observation that nearly all the waves are breaking continuously between the two sensor positions, implying that initial breaking is predominantly offshore of the deepest sensor position and breaking bores are not reforming before passing the inshore sensor.

The constant celerity spectra is consistent with the linear wave theory prediction for shallow water that celerities are frequency non-dispersive. The linear theory phase speed approximation, (III.5), for the average depth (2.61 m) between the sensors is plotted for comparison. Also plotted is the prediction from Cnoidal theory, (the asymptotic form given by Eq. III.6), using a significant breaking wave height of 1.30 m. Celerities at higher frequencies are assumed to be derived from harmonics of the peak frequency, therefore phase locked to the peak wave and travelling at the same speed.

Mean wave angles at the peak incident frequency, 0.07 Hz, are estimated from the longshore wavenumber, k_y, spectra of the wave field at two cross-shore positions: in the trough and on the outer flank of the first sand bar (Long and Oltman-Shay, 1991).

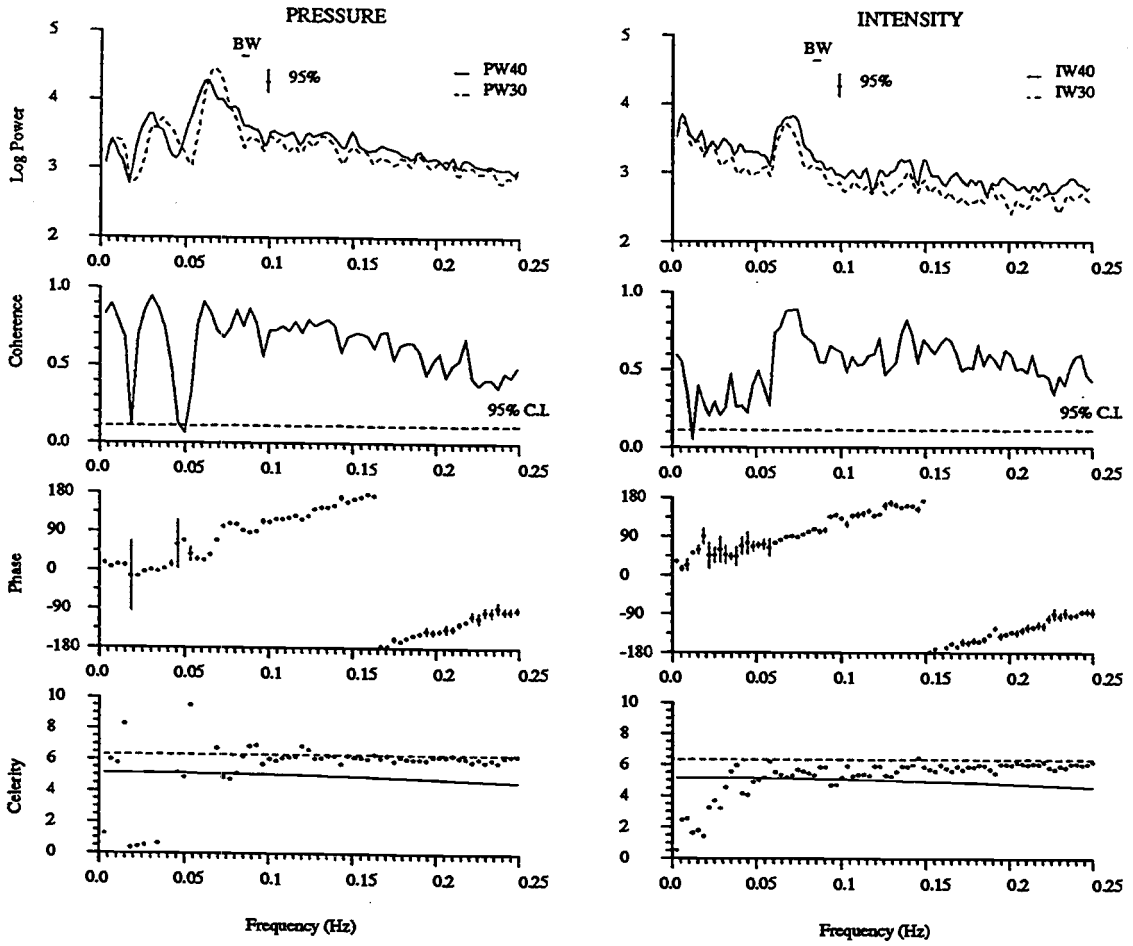

Figure III.3. Amplitude, coherence, phase, and celerity spectra between time series collected from sensors separated 18 m in the cross-shore for both pressure (left column) and intensity data (right column). All spectra are computed for 52 degrees of freedom. The linear (solid line) and Solitary (dashed line) theory approximations are plotted on the celerity spectra for comparison.

Wavenumber spectra for the peak frequency are estimated from longshore arrays of intensity time series (~2 hour records) and from current meters (cross-shore component only, ~4 hour records) at the same longshore locations, using the Iterative Maximum Likelihood Estimator (Oltman-Shay and Guza, 1987). Normalized wavenumber spectra at the peak frequency from both types of data are shown in Figure III.4. The agreement is good for the peak wavenumber, although the wavenumber half-power bandwidth from the intensity data is narrower in the trough but wider on the bar, possibly due to the selection of only the breaking waves, which were in general very long-crested.

The wavenumber of maximum energy is used to compute the average wave angle as $\alpha = \arcsin\left(k_y/\mathbf{k}\right)$, where $\mathbf{k}$ is the wavenumber magnitude given by the dispersion relation for linear waves, (Eq. III.5; Long and Oltman-Shay, 1991). The intensity data measure the same mean wavenumber as the current meters for each array, corresponding to a mean wave angle of -7.8 degrees in the trough and -7.5 degrees on the bar flank.

Phase Speed and Incident Angles of Individual Breaking Waves

Breaking waves are apparent in the intensity time series as distinct intensity peaks, and are identified using the following variable thresholding method (Figure III.5). Objective discrimination for long records was carried out determining the variation in number of waves counted as a function of the threshold level, set as a variable fraction of standard deviation. Intensity time series are first band-pass filtered to remove the low and high frequency energy unassociated with breaking incident waves. The means and trends are removed using a least-square quadratic fit to the data. The number of waves (using a modified zero-up-crossing method) with a maximum exceeding a threshold level are counted for a range of thresholds ranging from 1 to 4 times the standard deviation of the filtered time series. The correct threshold is set so that the number of waves counted matches that counted manually by visually inspecting a short section of the video tape. This method appears to work best for narrow banded swell days and tends to be more

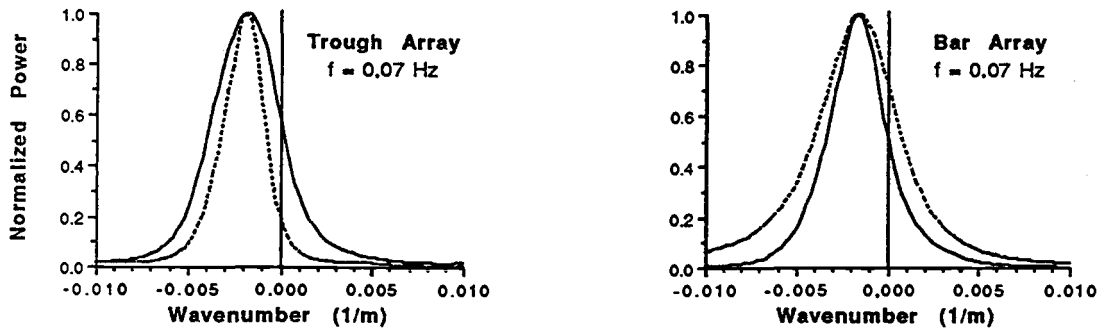

Figure III.4. Normalized wavenumber spectrum for the peak frequency on October 12, 1990 for the array located in the trough (left panel) and on the outer flank of the bar (right panel). The solid lines are the estimates from the current meters, and the dashed lines are from video data arrays. Current and intensity spectra are computed with 418 and 178 degrees of freedom, respectively, although, each have a frequency bandwidth of 0.0156 Hz and wavenumber bandwidth of 0.0002 m^{-1}.

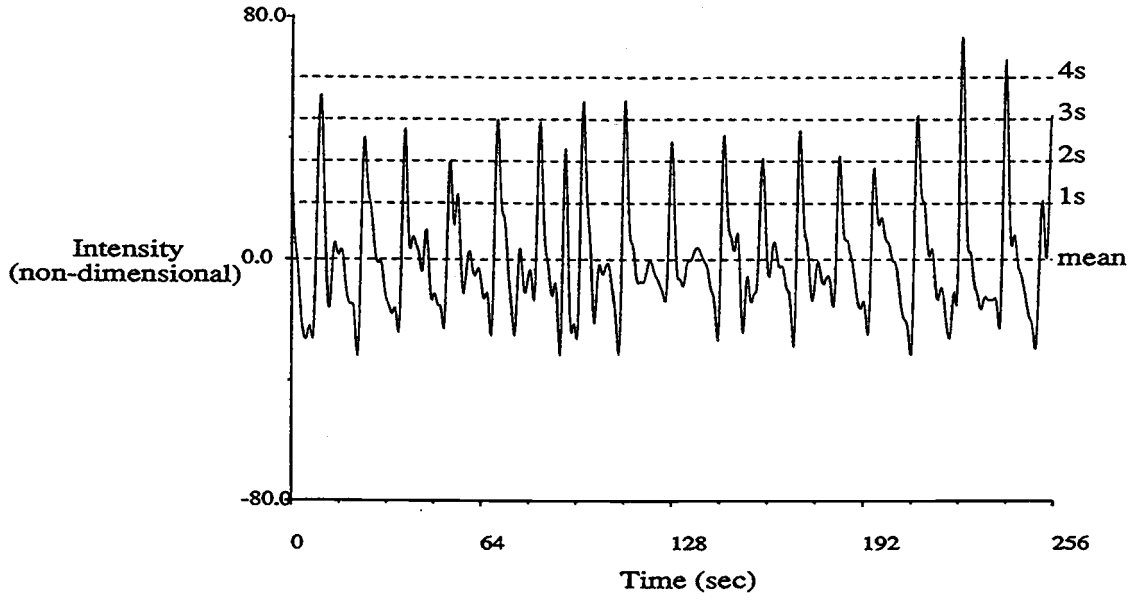

Figure III.5. An example intensity time series (band-pass filtered and mean corrected) from October 12, 1990 illustrating the variable thresholding method used to determine the passage of a breaking wave. The dashed lines indicate fractions of the standard deviation corresponding to 1.0, 2.0, 3.0, and 4.0. The vertical scale is in non-dimensional intensity units.

difficult on windy days when there is more local chop and residual foam (see Lippmann and Holman, 1989).

Estimates of the mean travel time of individual wave propagation are made using both the cross-covariance (III.8) and spectral (III.11) methods. The threshold level, determined from above, was used to indicate the passage of a breaking wave in a subsection of the time series, typically 32 seconds. The wave was skipped if zero or more than one wave was detected in the second time series within a set limit (2.0 seconds for ~5.6 m sensor separation). For the cross-correlation method the maximum correlation must also fall within that limit. For the spectral method, the windowed time series was demeaned, quadratically detrended, and a Kaiser-Bessel Cosine Taper data window applied, thus minimizing leakage and reducing the effective size of the window by a factor of 2. Frequency bands are then merged to improve the confidence intervals for the phase. 95% significance levels were set for each frequency in the interval $0.02 < f < 1.0$.

Phase speeds and wave angles of individual breaking waves are then computed from orthogonal slowness components (III.12) derived from pairs of sensors that form the diagonals of a square array 4 m wide. An example time series of the resulting phase speed and wave angle for the two time lag estimation methods is shown in Figure III.6. There is good agreement between the two methods. Mean phase speeds and wave angles (III.13) derived from the video data by averaging results from each method are summarized in Table III.1. They show consistent results for all sensors at the same cross-shore locations. The standard deviations in wave angle are quite large, on the order of the means, indicating that though the mean angle is from the south, there is an angular spread in the wave field (Figure III.6), possibly due to topographic refraction and some offshore directional spread. The mean wave angles show progressively more normal incidence as the waves progress landward, a result expected due to wave refraction in shallow water. Mean phase speeds also show reasonable results, in which higher speeds are measured offshore in deeper water. The mean phase speed values show similar results as predicted by first order theory (Eq. III.5-III.6).

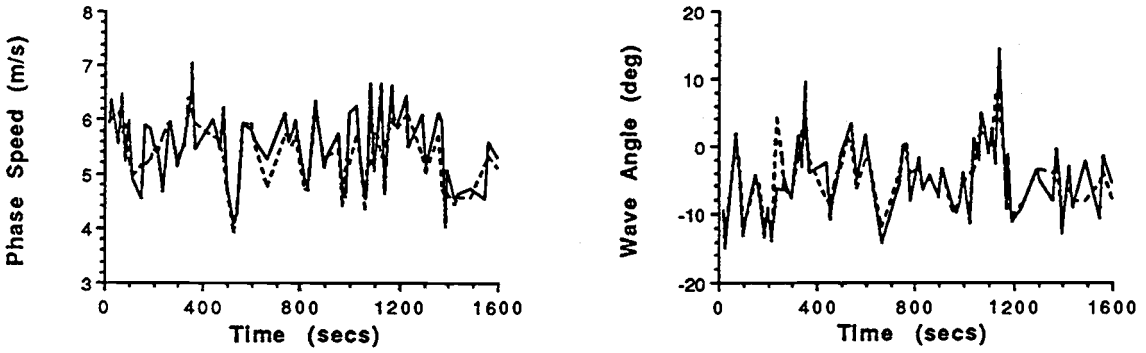

Figure III.6. Comparison of the two analytical methods for computing the phase speed (left panel) and wave angle (right panel). The solid line represents the estimate derived from the spectral method, and the dashed line is from the cross-covariance method.

Table III.1. Summary statistics of wave-by-wave analysis of phase velocity. The position of the sensor is given by x and y. The linear (L.T.) and solitary (S.T.) wave theory prediction for phase speed (in m/s) using the peak frequency, water depth, and rms wave height is also shown. (standard deviations of $|\bar{C}|$ and $\bar{\alpha}$ are in parentheses).

Name	x (m)	y (m)	$\|\bar{C}\|$ (m/s)	L.T.	S.T.	$\bar{\alpha}$ (°)	h (m)	H_{rms} (m)
CS10	125	985	5.2 (0.50)	4.0		-9.6 (4.7)	1.6	
CS20	145	986	6.0 (0.59)	5.0	5.8	-8.7 (7.6)	2.6	0.78
CS30	170	986	5.2 (0.64)	5.2	5.9	-7.0 (7.7)	2.7	0.80
CS31	170	967	5.4 (0.81)	5.2		-8.2 (7.2)	2.7	
CS32	169	936	6.0 (0.62)	5.2		-9.1 (8.2)	2.7	
CS33	168	926	5.3 (0.68)	5.1		-11.9 (6.6)	2.7	
CS34	166	856	6.1 (0.65)	5.2		-6.7 (10.9)	2.8	
CS35	165	806	6.4 (0.95)	5.2		-9.9 (9.7)	2.8	
CS40	189	986	5.4 (0.65)	4.8	5.6	-7.5 (7.5)	2.3	0.84
CS50	207	986	7.4 (1.12)	4.8	5.8	-13.8 (6.7)	2.4	1.04
CS54	210	856	7.7 (0.94)	5.0		-17.3 (12.5)	2.6	
CS60	226	986	7.9 (1.39)	5.5		-19.9 (6.7)	3.0	
CS70	245	986	7.9 (1.19)	6.1	6.9	-20.2 (10.1)	3.8	1.10
CS71	244	966	7.2 (0.67)	6.1		-16.6 (9.9)	3.8	
CS72	244	936	7.1 (0.75)	6.1		-21.2 (9.7)	3.7	
CS73	243	926	7.2 (1.02)	6.1		-19.9 (8.2)	3.8	
CS74	241	856	8.6 (1.39)	6.1		-23.1 (15.0)	3.9	

DISCUSSION

Celerity spectra are estimated from both video intensity time series and *in situ* pressure data. The results are similar for both data types and show reasonable agreement with Cnoidal theory, which includes first order amplitude dispersion (higher order theories which include the Boussinesq approximation are not considered). The theory deviates from the data at higher frequencies where the waves are no longer in shallow water. Similar results were obtained previously with pressure data by Thornton and Guza (1982), who found celerities to be weakly amplitude dispersive. They also noted that low frequency motions and mean currents could produce deviations from simple, first order theory.

Results from the spectral analysis of intensity time series indicates that the video data samples the breaking wave field well. The improvement over previous visual methods is accomplished by the good spatial resolution of the geometrical transformation of image points to ground position. The measurement of breaking wave phase speed and angle from simple square arrays of tightly placed sensors can now be applied to field data in general, providing a quantifiable means for testing some of the common sediment transport theories. Insight into the dynamics of breaking waves, although not a concern of this paper, appears to be a viable natural consequence of the measurement techniques.

The problem of directional spread of the incident wave field in the surf zone is not easily solved. In the past, directional spectra in deep water have been computed from slope arrays of bottom mounted pressure sensors or pitch-and-roll buoys (Oltman-Shay and Guza, 1984), or with greater angular resolution from large aperture longshore arrays of spatially separated wave sensors (Long and Oltman-Shay, 1991). Surf zone arrays have been successfully used to determine the wavenumber-frequency content of low-frequency motions, such as edge and shear waves. However, higher frequencies are not easily resolved, largely due to its shorter longshore length scale (limited by Snell's Law,

Eq. III.7). Alongshore topographic refraction due to irregular beach topography can also cause a reduction in coherence over the large spatial scale of the array . For the data run looked at in this study, the long period swell is coherent over the length of the array, and since the beach topography was nearly two-dimensional (Bill Birkemeier, pers. comm.), spatial inhomogeneity was reduced. Therefore, the mean values obtained from video and current meter data (which show similar results) appear to be valid.

Resolution and uncertainty will be dependant on the spatial separation of the sensors and the sampling interval. The placement of sensors depends on the expected coherence of the wave field. For short, choppy seas the coherence drops off rapidly, however for long crested swell the waves are coherent over a much greater distance. In the surf zone the waves are refracting, interacting with other waves, and breaking and reforming, thus it is expected that the coherence will not be high over large scales, thus sensors must be placed closer together. Uncertainty due to loss of coherence can more than compensate for the gain from spatial resolution. The adjustments are easily made using the video method.

CONCLUSIONS

Time series of image intensity appear to accurately represent the phase progression of breaking waves, and show good spectral agreement with *in situ* pressure measurements in the incident band. Celerity spectra compare favorably with solitary wave theory for the day analyzed. Wavenumber spectra at the peak frequency from video derived data and from an *in situ* current meter array show similar results in the trough, but deviate slightly offshore.

The discrimination of breaking waves is intrinsic to the nature of the video data. Individual waves are identified using a variable thresholding method calibrated manually by inspecting the video tapes. Phase speeds and wave angles of individual breaking surface gravity waves are also estimated from pairs of intensity time series sampled at locations arranged in a square array with 4 m side width. Time lags for 32 second windows, centered around the occurrence of a passing wave, are computed directly from the cross-covariance function or from the slope of the phase spectrum. Slowness (inverse of phase velocity) estimates are computed for each orthogonal sensor pair, and then combined to yield phase speed magnitudes and wave direction. Results are similar for each method. Mean wave angles and phase speeds agree with simple shoaling theory.

These results are encouraging. The video method measures the dynamically important waves that presumably provide the forcing for nearshore phenomena and sediment transport. The determination of breaking wave statistics appears to be useful for application to surf zone forcing and sediment transport models. A new method for sampling waves is available, and is not constrained by logistic difficulties of adverse surf zone conditions. Furthermore, the ability to post-design arrays and sampling location make this video technique attractive for studying large scale wave-induced flow phenomena.

ACKNOWLEDGEMENTS

This work could not have been done without the excellent staff at the FRF, led by Bill Birkemeier. Special thanks to Kent Hathaway for providing unlimited field and lab support during DELILAH, and to Pete Howd and Todd Holland for first aid and data collection abilities. Appreciation is given to Ed Thornton and Bob Guza for providing the surf zone data used in calibration of the video data. Paul O'Neill was chief engineer for the video group and as usual, was outstanding. Chuck Long at the FRF provided the directional wave information from the linear array. The wavenumber-frequency spectra were computed using software developed by Joan Oltman-Shay. This work was supported by the Office of Naval Research, Coastal Sciences program under grant number N00014-90-J1118. A large potion of the funding for the DELILAH experiment was graciously contributed by CERC. Finally, thanks to D.J.A., K.S.M., B.T.W., and S.E. for enhancing after hours entertainment during DELILAH.

CHAPTER 4

Modulations in Wave Breaking Due to Incident Wave Groups

ABSTRACT

When gravity waves dissipate by breaking, momentum is transferred to the water column, forcing secondary flows. Modulations in this process due to varying incident wave height can therefore force motions at group, or infragravity, time scales. The principal aim of this work is to quantify the temporal and spatial scales associated with modulations in incident wave dissipation by wave breaking in the surf zone. A video based sampling technique is employed which relies on the gray tone contrast between lighter intensity of foam and bubbles created by actively breaking waves and bores, and the darker, unbroken surrounding water. Video image intensity time series, $I(x,y,t)$, are compared with colocated *in situ* measurements of sea surface elevation and bi-directional current collected on a narrow band day (in both frequency and direction) during the DELILAH experiment.

In the region of fluctuating surf zone width low frequency oscillations in I are associated with wave groups. Low frequency phase relationships between I data at adjacent locations in a cross-shore array indicate a shoreward progressive group structure up to the crest of the bar. Landward of the bar crest low frequencies in I are uncoupled from group modulations seaward of the bar. The temporal and spatial scales of the group modulations indicate that infragravity band forcing would be broad-banded across wavenumber-frequency space. However, no coherence was found between the group forcing in the outer part of the surf zone and the infragravity band response in the inner surf zone and at the shoreline. Low coherence can be a consequence of the Q (resonance) of the system being high, substantial topographic influence (*e.g.*, Kirby, *et al.*, 1981), or lack of significant coupling between wave breaking distributions and free infragravity waves (Bowen and Guza, 1978).

In the inner surf zone (where nearly all waves are breaking) low frequency intensity energy appears to be a result of foam on the sea surface being advected by currents away

from the area of greatest foam production (in the vicinity of the bar crest). Strongest low frequency signals in I have longshore structure characteristic of shear instabilities of the longshore current, and high mode edge waves or leaky waves. Finally, contrary to model predictions, image intensity data show that wave dissipation does not stop as waves propagate past the bar crest into the deeper water of the trough. The observed continued dissipation could be an important mechanism for producing observed distributions in the mean longshore current (*e.g.*, Roelvink and Stive, 1989).

INTRODUCTION

Wave motions with much longer periods than typical sea and swell waves were first observed in the nearshore by Munk (1949), who coined the term "surf beat" to generally describe oceanic waves with periods on the order of several minutes (subsequently these have been called infragravity waves to distinguish them from the simple incident wave modulation). Motivated by Munk's observations, Tucker (1950) made comparisons between the incident wave envelope and low frequency oscillations in the same sea surface elevation time series (sampled approximately 1 km offshore), and found correlations at 3-5 minute lags with the wave envelope leading the surf beat. Tucker speculated that the lag represented the time needed for the wave group to propagate shoreward to the surf zone where a long wave was generated, then for the long wave to propagate seaward back to the point of measurement. Predicted travel times were in general agreement with the observed time lags.

Since these initial observations, considerable effort has been focused on understanding the link between incident wave groupiness and low frequency waves in the nearshore. The most widely accepted theory suggests that in deep water a depression in mean water level (set-down) is forced by gradients in the momentum flux (radiation stress) associated with a modulating incident wave field (Longuet-Higgins and Stewart, 1962, 1964). Secondary long waves are generated by time varying gradients on scales associated with wave groups. Offshore this leads to a forced response at infragravity frequencies. The long wave is phase-locked to the groups, with a phase relationship of 180° with the wave envelope, and thus propagates at the group velocity. In shallow water the forced response may become resonant and free waves can be generated (*e.g.*, Bowen and Huntley, 1984).

The nature of the free wave response depends on the time and length scales of the forcing and can be either edge waves or leaky waves. Edge waves are the normal mode

oscillations (discrete resonances of the system) that exist on a plane sloping beach, and obey the dispersion relation

$$\sigma^2 = gk_y \sin(2n+1)\beta \qquad \text{(IV.1)}$$

where σ and k_y are the edge wave radian frequency ($2\pi f$) and alongshore wavenumber ($2\pi/L$), respectively, g is gravity, n is the edge wave mode number, and β is the beach slope (Eckart, 1951; Ursell, 1952). Edge waves are trapped to the shoreline by refraction since their phase speeds are dependent on the local depth, $c = \sqrt{gh}$. Leaky waves are those waves which reflect from the shoreline at steep angles to the beach and thus escape the nearshore by propagating into deep water. Edge wave modes are distinguished from a continuum of leaky and forced waves by their σ-k_y relationship, where

$$\frac{\sigma^2}{g} > |k_y| \qquad \text{Leaky waves} \qquad \text{(IV.2)}$$

$$\frac{\sigma^2}{g} < |k_y| < \frac{\sigma^2}{g\beta} \quad \text{and (IV.1)} \qquad \text{Edge waves} \qquad \text{(IV.3)}$$

otherwise $\qquad$ Forced waves $\qquad$ (IV.4)

Bowen and Guza (1978) show that resonant free waves, (IV.2) and (IV.3), are likely to dominate over forced waves, (IV.4), which have σ-k_y relationships which do not satisfy (IV.1). In fact, field data from oceanic beaches indicates that indeed infragravity motions in the surf zone predominantly consist of free edge wave modes and leaky waves (Huntley, *et al.*, 1981; Oltman-Shay and Guza, 1987; Howd, *et al.*, 1991; and others). In addition, it has been shown recently that some very low frequency waves may be instabilities of the longshore current which have low celerity, $\sigma \approx k_y \overline{V}$, where $\overline{V}$ is the mean longshore current, and are thus easily distinguished from edge waves in σ-k_y space (Bowen and Holman, 1989; Oltman-Shay, *et al.*, 1989).

The link between forcing by incident band modulations and infragravity wave response has been the subject of much experimental study. Many investigators have tried to correlate the incident wave envelope with low frequency wave motions, similar to the early work of Munk (1949) and Tucker (1950) but with more sophisticated sampling methods and analytical techniques (*e.g.*, Huntley and Kim, 1984; Guza, *et al.*, 1984; List, 1987, 1991, 1992). These studies have met with only limited success, largely owing to the stochastic nature of real ocean waves, which generally do not have a single group time scale. Furthermore, Bowen and Guza (1978) and Holman (1981) point out that resonant edge wave response requires at least some of the temporal and spatial components of the group forcing, $\mathbf{F}(x,t)$, to match the cross-shore structure of the edge wave, $\phi_n(x)$. Mathematically, resonant edge wave growth rates are determined by

$$\frac{\partial a_n(t)}{\partial t} \approx \frac{a_1 a_2}{g} \frac{\int_0^\infty \mathbf{F}(x,t)\phi_n(x)dx}{\int_0^\infty \phi_n^2(x)dx} \qquad \text{(IV.5)}$$

where a_n is the edge wave modal amplitude, and a_1 and a_2 are incident wave amplitudes. Thus, without coupling between $\mathbf{F}$ and ϕ_n, significant edge wave growth cannot occur. Furthermore, resolving $\mathbf{F}$ in the field is difficult due to inherently large time and space scales of stochastic wave breaking. In this study, data are presented which quantify the temporal evolution of breaking wave patterns, a proxy for $\mathbf{F}$, over large spatial scales of natural surf zones.

The data used to quantify wave breaking patterns in this study were gathered remotely utilizing video image processing techniques. The technique is based on contrast between the dark intensity of non-breaking water and the lighter intensity of foam and bubbles associated with actively breaking waves and bores. Image intensity is digitized

by an image processing system at discrete pixels corresponding to known field coordinates. Data are collected along a cross-shore transect extending from near the maximum break point to the saturated inner surf zone, and from large longshore arrays that span several hundred meters down the beach.

A brief description of the sampling methods and the basis by which video data serves as a proxy for dissipation modulations are presented next, followed by a description of the field site and ancillary measurements used in the study. Analysis of wave breaking time series sampled from video tapes of the surf zone are presented as a function of cross-shore distance, and are compared with direct observations of sea surface elevation and velocity in both the time and frequency domains. Alongshore arrays are used to investigate the temporal and spatial scales (*i.e.* frequency-wavenumber) of wave breaking patterns. Comparisons are made between modulations in breaking wave distributions in the region of fluctuating surf zone width and the response in the flow field observed in the inner surf zone and at the shoreline (runup).

SAMPLING TEMPORAL AND SPATIAL SCALES OF WAVE BREAKING

Previous estimates of breaking wave distributions were determined by visually identifying breaking waves in the time series of sea surface elevation on site during the collection of the data (Thornton and Guza, 1983). This method works well, although with tremendous logistical effort. Lippmann and Holman (1989b) made similar observations utilizing video recordings to identify breaking waves in colocated sea surface elevation time series. Remote sensing techniques are not constrained by potential destruction due to wave forces, and can sample at numerous locations simultaneously over large spatial scales. Video techniques thus have great potential for field use.

The basis by which nearshore measurements can be made with video methods is from the visible surface expression of actively breaking waves and bores in the surf zone (or indirectly through the modification of wave breaing by interactions with lower frequency waves). An example snap shot of wave breaking in the surf zone is shown in Figure IV.1. The high intensity of the foam and bubbles created from active wave breaking contrasts with the darker non-breaking water.

In this work, our principal aim is to quantify the time and space scales associated with modulations in incident wave dissipation through breaking, ε_b. We hypothesize that time series of image intensity, $I(x,y,t)$, can be used as a means to quantify the time and space scales of ε_b at given locations throughout the surf zone. Thus we assume

$$I(x,y,t) \propto \varepsilon_b(x,y,t) \tag{IV.6}$$

where x and y are the cross-shore and alongshore Cartesian coordinates, respectively. Following the random wave dissipation model of Thornton and Guza (1983), wave breaking distributions, and thus image intensity patterns, are expected to show a strong dependence on local depth. For the case of time averaging, Lippmann and Holman

Figure IV.1. Example photographic snap shot of wave breaking in the surf zone from October 13, 1990 at ~0900 EST. Breaking waves and bores are identified by the sharp contrast between breaking and non breaking waves.

(1989a) tested and exploited (IV.6) in a technique to image subaqueous morphology using ten minute time averages of wave breaking patterns. Figure IV.2 is a ten minute time exposure image illustrating the average image intensity pattern of a typical surf zone. In this work, we reduce the time scales of interest to the order of incident waves. Thus we include low frequency modulations in wave breaking patterns, and attempt to find an association with infragravity waves.

Quantification of images is accomplished using a real time image processing system. Video frames are digitized (at up to 30 Hz) by the image processor into an array of 512 x 480 picture elements (pixels). Individual pixels store the value of light intensity (luminance) in gray shades from 0 (black) to 255 (white). Images are digitally enhanced to better show the contrast differences of the observed phenomena; for example, images are typically contrast-stretched to the full 256 gray shade range prior to analysis.

Image locations of interest (for example the location of a fixed surf zone instrument) are determined using known photogrammetric transformation equations assuming the vertical coordinate to be the still water level (Lippmann and Holman, 1989a). Time series at each location are then collected by sampling the corresponding pixel intensity at a sampling frequency of 6 Hz for the entire run (tape) length of ~2 hours. Overall, several hundred pixel locations were sampled from two cameras (shown later in Figure IV.3). Resolution in image pixels is typically much less than 1 m in the cross-shore direction, and from ~0.5-5 m in the longshore direction.

While intensity values from a particular view can be compared, different contrast enhancements between cameras makes inter-camera comparisons of intensity magnitudes difficult. Gain and offset adjustments can be applied to the means and variances to allow basic statistical comparisons beetween views. In addition, relative temporal phase relationships of shoreward progressive breaking waves, sampled in different camera views, are not altered by video levels. Furthermore, higher order statistics (such as skewness) and probability density functions can also be compared.

Figure IV.2. Example ten minute time-exposure image (created digitally with an image processing system) from October 13, 1990 at ~0900 EST. Wave breaking patterns have been averaged over ten minutes to yield a statistically stable pattern of the surf zone sea surface luminance, revealing a clear picture of the (linear) sand bar morphology.

FIELD METHODS

The data were collected as part of the DELILAH experiment in October of 1990, held at the Army Corps of Engineers Field Research Facility (FRF) on the Outer Banks of North Carolina near the village of Duck (Birkemeier, *et al.*, 1991). A general description of the beach conditions at the FRF is given by Birkemeier, *et al.* (1985). A map of the field site showing the position of the cameras on the FRF tower (44 m above NGVD), the fixed *in situ* instruments, and the FRF pier is shown in Figure IV.3. The ground coverage of the cameras used in this study are also shown in the figure. The imaged area ranges from the dune crest to ~400 m offshore and begins ~180 m north of the FRF pier and extends alongshore ~350 m. The cameras were mounted in weatherproof housings, hard wired to the FRF building, and recorded in S-VHS format.

Direct measurements of the wave field used in this study include data from two alongshore arrays of bi-directional current meters and a cross-shore array of colocated current meters and strain gage pressure sensors. In addition, shoreline runup elevation was digitized from video tapes using the timestack methods of Holland and Holman (1992) using the camera labeled R2. Offshore (seaward of the surf zone) wave conditions are provided by an alongshore array of bottom mounted pressure gages located ~800 m offshore in 8 m depth (Long and Oltman-Shay, 1991).

Video time series data for this paper were collected using cameras labeled DS and OF (Figure IV.3). Time series were sampled at the location of all the fixed surf zone instruments to allow best comparison with *in situ* wave records. Data were also obtained along a cross-shore transect along the main instrument line (y = 986 m in the FRF coordinate system), from just outside the shore break (x = 135 m) to the far reaches of the surf zone (x = 505 m) with a cross-shore spacing of 10 m, as well as an alongshore array spanning 230 m (from y = 976-1206 m) located at x = 500 m and with a longshore spacing of 10 m. Timing errors with *in situ* instrumentation were minimized by

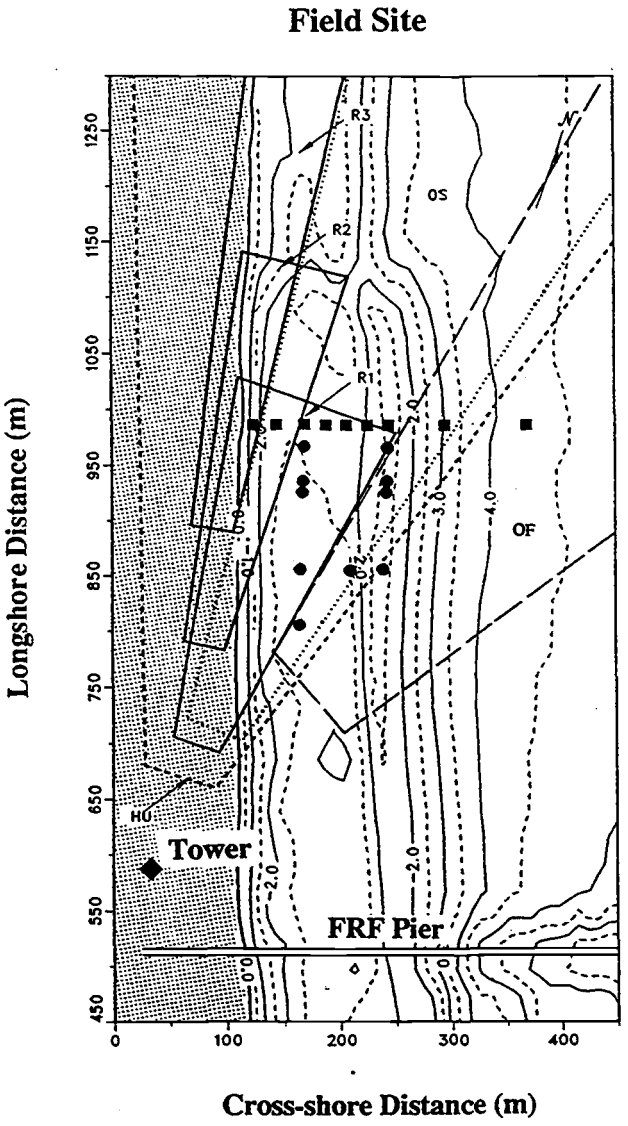

Figure IV.3. Schematic maps of the field site during the DELILAH experiment held at the Army Corps of Engineers Field Research Facility near Duck, N. C. Bathymetric contours were from bathymetry sampled on October 9 during the experiment. The relationship of the camera location on top of the FRF tower is shown in relation to the study area and the FRF pier. The location of fixed *in situ* instruments are shown with squares to indicate colocated strain gage pressure gages and bi-directional current meters, and with circles for single current meters. The ground coverage of the cameras are shown identified by the outlined areas.

synchronously recording on audio channels video generated (SMPTE) timecode as well as the time base used by all other surf zone instruments.

Data are presented from October 13 at ~0645 EST, coinciding with swell generated by Hurricane Lily. Low tide (-0.21 m NGVD) occurred at ~0900 EST. A photographic snap shot from this day is shown in Figure IV.1. The offshore incident waves during this period were long crested and energetic, with $H_s \approx 2.23$ m in 8 m depth. Directional spectra from the 8 m depth array (Figure IV.4) shows a very narrow banded swell at the peak frequency, $f_p \approx 0.083$ Hz, approaching from an incident angle $\alpha_o \approx 24°$ CW from normal to the beach. The nearshore bathymetry consisted of a prominent linear bar ~100 m offshore (Figure IV.5). Although only partial bathymetric measurements were obtained on this day (with the Coastal Research Amphibious Buggy, or CRAB; Birkemeier and Mason, 1984), bar morphology observed from time-exposure data (Figure IV.2) was approximately linear, indicating alongshore homogeneity in topography is reasonably approximated. Figure IV.5 shows the bathymetry from October 12, as well as cross-shore profiles at the position of the main cross-shore array ($y = 986$ m) from October 12, 13, and 14.

All sampled positions discussed are referred to in the FRF "right-handed" coordinate system (Figure IV.3), with alongshore distance increasing to the north and cross-shore distance increasing offshore. For reference, the position of the shoreline is at $x \approx 120$ m and the approximate bar crest is at $x \approx 220$ m (Figure IV.5). In addition, the surf zone area seaward of the bar crest is referred to as the region of fluctuating surf zone width, since large incident amplitude modulations cause the maximum width of the surf zone to vary over several hundred meters on time scales of a few minutes (shown later).

Frequency - Direction Spectra
13 Oct 90 0700 EST

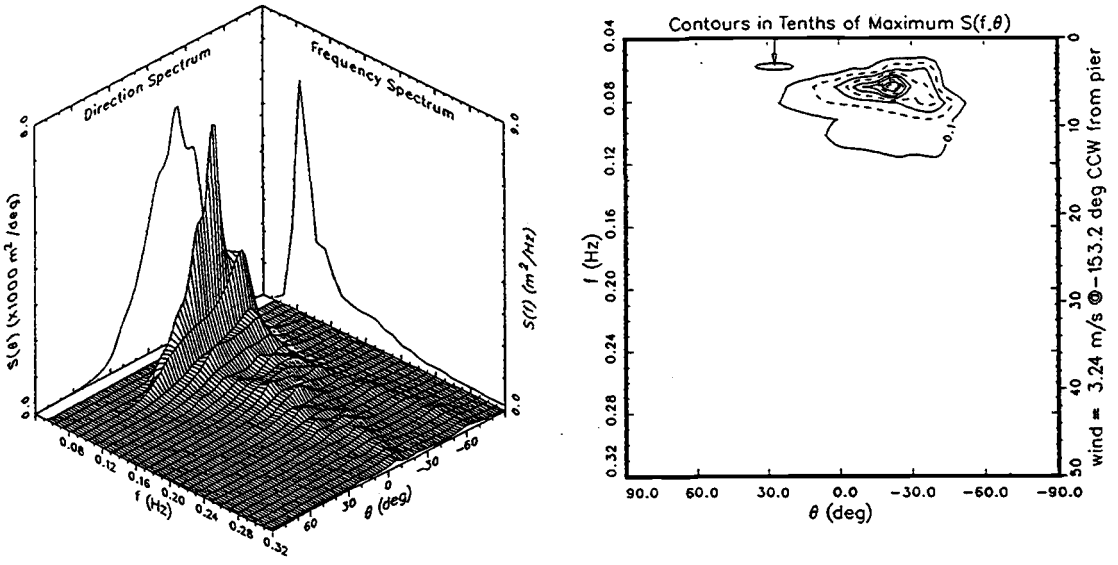

Figure IV.4. Three-dimensional (left panel) and contour (right panel) plots of wind-wave directional spectrum at the 8 m depth array from October 13, 1990. The spectra were computed from a 3 hour run beginning at 0700 EST. The 95% confidence intervals on the estimates are shown in the contour plot. Negative angles indicate waves approaching the beach from the southeast. The waves during this run were energetic (H_S = 2.23 m) and very narrow banded in both frequency ($f_p \approx 0.083$ Hz) and direction ($\alpha_o \approx$ 24° CCW from the beach normal).

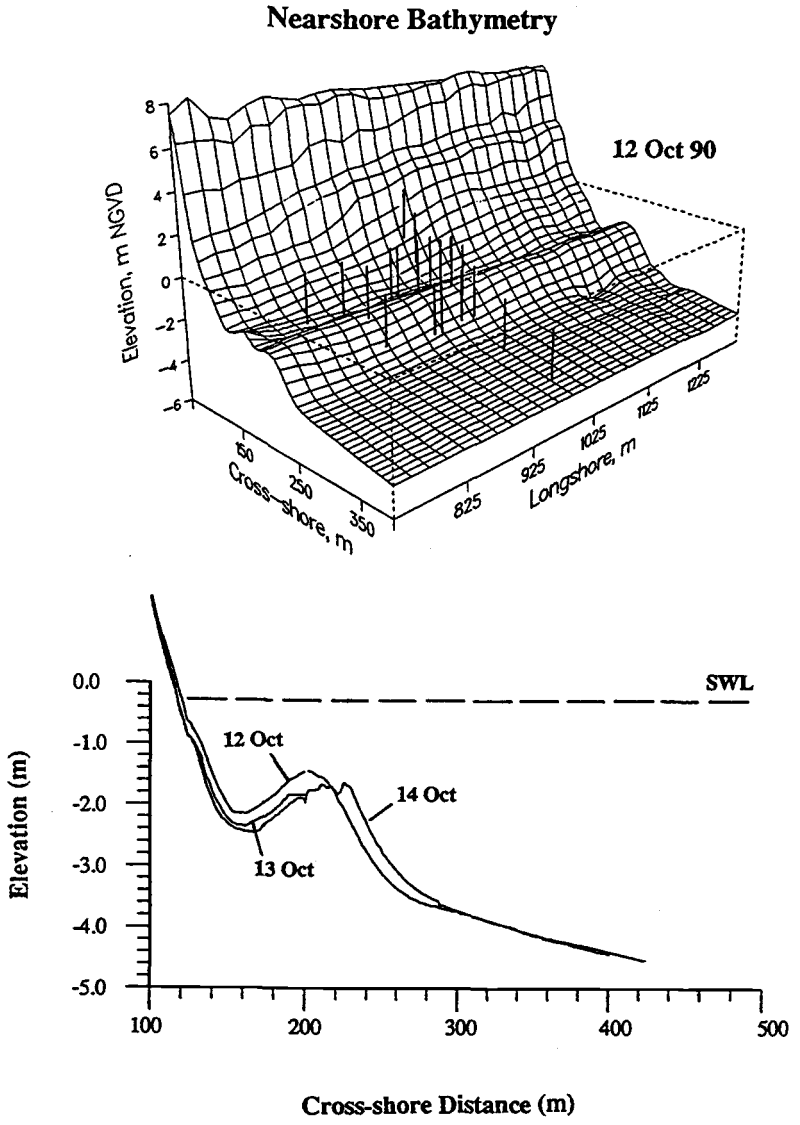

Figure IV.5. Nearshore bathymetry of the study area surveyed with the CRAB from October 12, 1990 is shown in the upper panel. Also shown in the lower panel are cross-shore beach profiles along the main instrument array (y = 986 m) from October 12, 13, and 14 and the still water level (SWL). (Bathymetry obtained on the 13th was limited to inside the bar crest due to the strong currents.) The bathymetry was characterized by a single shore-parallel linear sand bar. The location of the surf zone instruments are shown in the bathymetry plot for reference.

RESULTS

Cross-shore Time Domain Analysis

Figure IV.6 shows an example I time series (mean corrected) from just shoreward of the bar crest at (x = 188 m in the FRF coordinate system) along the main instrument line (y = 986 m). I time series are characterized by large intensity peaks which represent changes in contrast. The largest peaks are associated with the lighter color of foam and bubbles created by actively breaking waves and bores, easily identifiable in the snap shot shown in Figure IV.1. The wave peaks in I are characterized by steep front faces and a gradual decrease in intensity after the passing of the crest.

For comparison, time series of colocated η, u (positive offshore) and v (positive to the south) are also shown in Figure IV.6. The correlation coefficients, r, between I and the fixed *in situ* instruments are all high, with values of 0.54, -0.51, and -0.31 for η, u, and v, respectively. The passage of incident waves (breaking and non breaking) are clearly identified in η and u. The peaks in I coincide with the passage of most but not all the waves, indicating that nearly all the waves are breaking. The relationship of I with v is not as strong since the waves were nearly shore normal at the position of the sensor (α_o <~ 10°). Note that the shape of the waveform in I is similar to the waves observed in η, in which wave crests are pitched forward with steep front faces and a lower back slope.

Figure IV.7 shows time series of I, η, u, and v from a location well seaward of the bar crest (x = 370 m) in the region of fluctuating surf zone width, where breaking is sporadic. Not all the waves are detected in I, indicating a much lower percentage of waves are breaking compared with the saturated inner surf zone (Figure IV.6). Waves in η are more skewed and less asymmetric than those observed in the bar trough, whereas peaks in I are generally more broad. Correlation coefficients in this region are generally

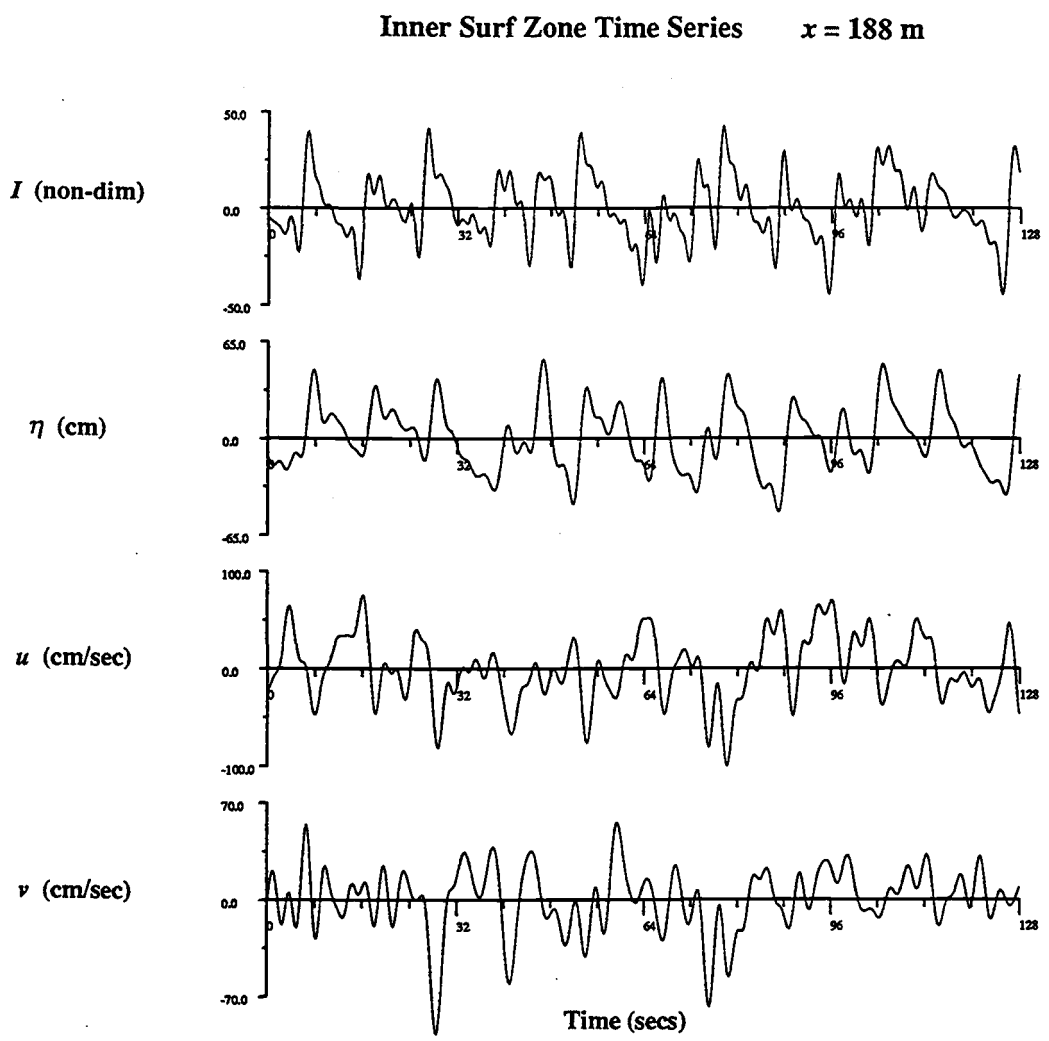

Figure IV.6. Example 128 second time series (mean corrected) of video image intensity, I, sampled at $x = 188$ m (in the FRF coordinate system) in the trough of the bar. Also shown for comparison are η, u, and v from the same location. The vertical axes are scaled to approximately +/- 3 standard deviations in the respective time series. Peaks in I coincide with peaks in the wave record, identifying the passing of breaking waves and bores. Most of the waves in η are identified in I, indicating that nearly all the waves are breaking.

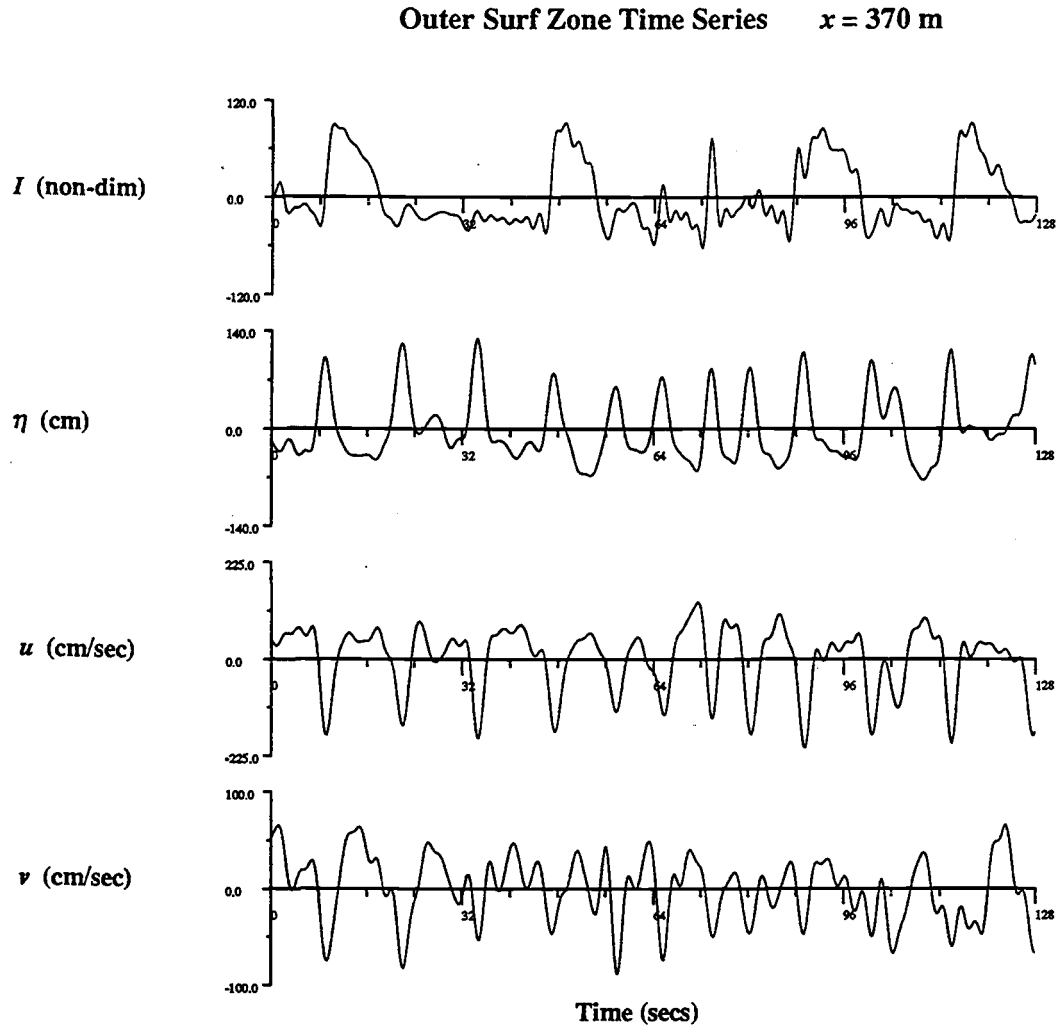

Figure IV.7. Same as Figure IV.6 for data sampled at $x = 370$ m, approximately 150 m seaward of the bar crest. Much fewer waves are identified in I, indicating a lower percentage of waves are breaking than in the inner surf zone (Figure IV.6).

smaller than in the inner surf zone (Figure IV.6), with values of -0.20, 0.17, and -0.15, for η, u, and v, respectively.

The groupy behavior of breaking waves is seen graphically by plotting together time series of I sampled along a cross-shore transect spanning the width of the surf zone. Figure IV.8 shows 38 vertically stacked I time series, each of 120 minute duration. Time series were sampled from two camera views at 10 m intervals along the main cross-shore array (y = 986 m), from far offshore but still in the surf zone, x = 505 m, to just seaward of the shore break, x = 135 m. The intensity values are normalized to +/- 3 standard deviations about the mean in each respective time series. Also shown on the right hand side is the approximate cross-shore beach profile obtained from CRAB data (recreated from Figure IV.5).

Seaward of the bar crest wave breaking distributions clearly show the arrival of wave groups, with breaking being more infrequent in the outer surf zone. The group structure is reduced by breaking in shallower depths. At the bar crest, nearly all of the waves are breaking. Interestingly, bores do not cease breaking immediately landward of the point of minimum depth over the bar, but continue to break well into the deeper water of the trough. Although the vigor of breaking is gradually reduced further into the trough, breaking generally does not cease. (At higher tides wave breaking in the trough is generally greater.) This phenomena was reported previously by Lippmann and Holman (1989b) in an analysis of different data collected at this same beach in October of 1986.

Figure IV.8 clearly shows the different characteristics in I collected well seaward of the bar and in the saturated part of the surf zone. Offshore the intensity fluctuates slightly about the mean value until the passing of breaking waves (Figure IV.7). At the bar crest intensity patterns fluctuate in response to most of the waves since they are nearly all breaking (Figure IV.6). This behavior in I is seen clearly in probability density functions (pdf). Example pdf's from I sampled at x = 205 m and x = 505 m are shown in Figure IV.9. Offshore the pdf is highly skewed, whereas at the bar crest the pdf is more

Figure IV.8. Time series (for a 120 minute record) of I sampled at 10 m intervals along the main cross-shore array, from just beyond the shore break (x = 135 m) to the outer surf zone (x = 505 m). The vertical axis is nondimensional image intensity (mean corrected) scaled to +/- 3 standard deviations. Time series are stacked vertically with offshore distance increasing toward the top. The beach profile (from Figure IV.5) is shown at the right. The time series clearly show the occurrence of wave group modulations in wave breaking.

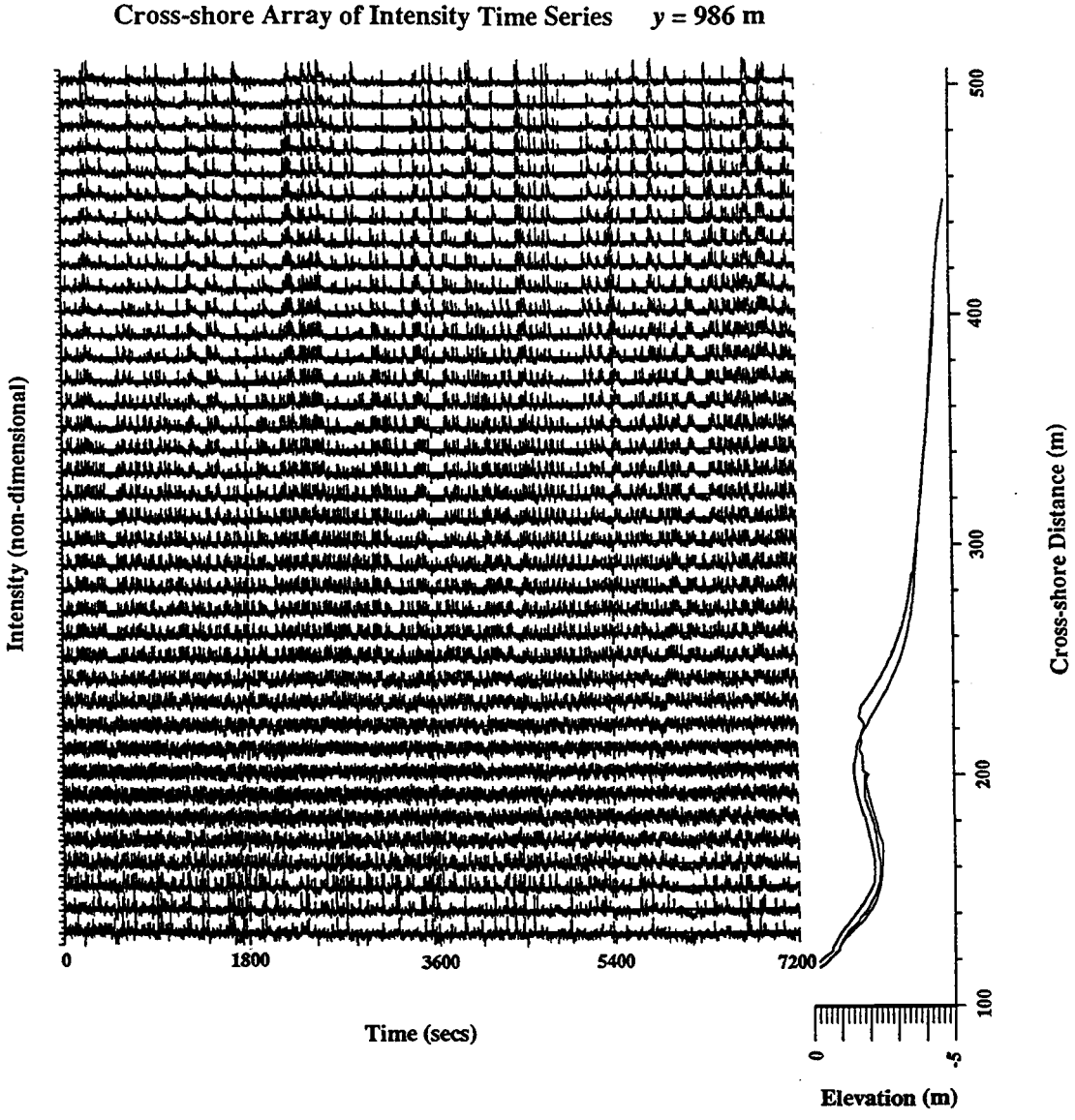
Cross-shore Array of Intensity Time Series y = 986 m
Intensity (non-dimensional)
0
1800
3600
5400
7200
Time (secs)
500
400
300
200
100
Cross-shore Distance (m)
0
-5
Elevation (m)

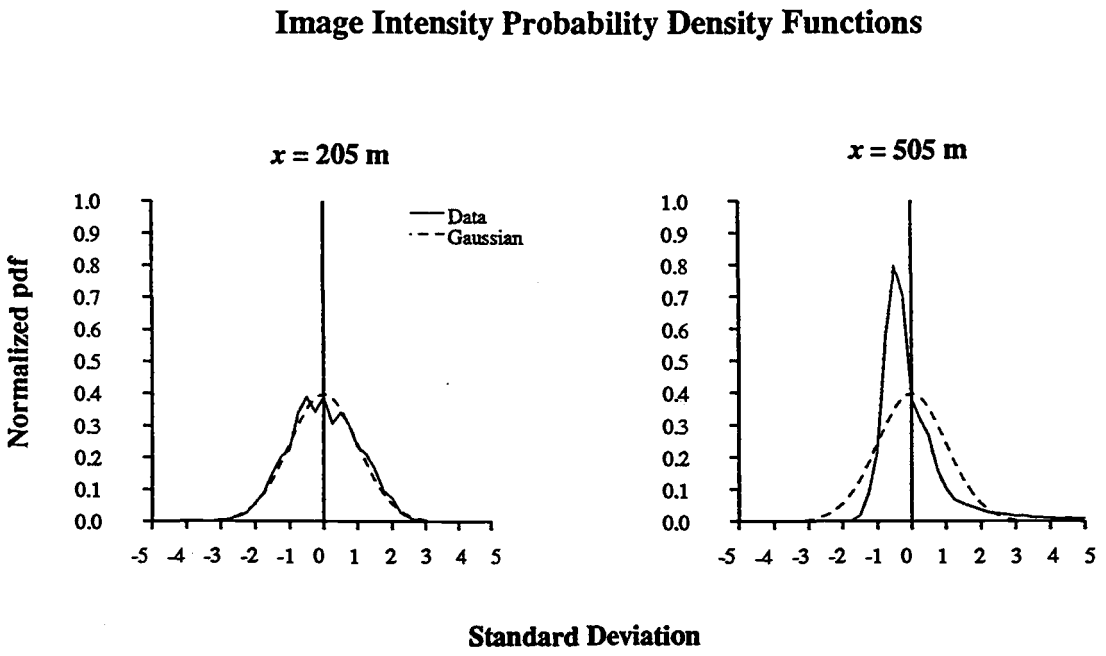

Figure IV.9. Example normalized probability density functions from I sampled near the bar crest (x = 205 m; left panel) and in the far reaches of the surf zone (x = 505 m; right panel). The horizontal axis is in number of standard deviations. The data are shown with the solid lines, and the Gaussian distribution for the mean and standard deviations in the respective time series is shown with the dashed line for comparison.

normally distributed. In general, the pdf is more skewed where fewer waves are breaking. These differences in breaking distributions are best represented by the third order moment of the time series, the skewness, a first order estimate of the degree to which the data are Gaussian distributed.

Figure IV.10 shows the first 3 moments from each time series plotted in Figure IV.8. The mean values represent the average image intensity, the same as that obtained from a time exposure image (*e.g.*, Figure IV.2). The I means are clearly higher over the bar, an association with topography previously used by Lippmann and Holman (1989a) in sampling bar morphology. The higher intensity at the bar is from increased wave breaking but also from the persistence of residual foam (left after the passage of a breaking wave). The standard deviations in regions of relatively higher residual foam (at and just landward of the bar crest) are diminished because the higher background intensity tends to reduce contrast. The cross-shore behavior of the skewness is a clear indicator of wave breaking distributions, since it best represents the systematic differences in the pdf's (Figure IV.9). In Figure IV.10 the (normalized) skewness is high offshore where the fewest waves are breaking (and the pdf is highly non Gaussian), becomes gradually smaller in shallower depths as more waves are breaking, is nearly zero at the bar crest where the wave field is saturated, and becomes large again in the trough as bores begin to reform.

There are also long period fluctuations (greater than incident periods) observed in both I and the wave records. The nature of this signal in I and its relationship to incident wave breaking is of interest since modulations in incident wave amplitudes potentially give rise to infragravity wave forcing (Eq. IV.5). We investigate the nature of any long period fluctuations in I in the frequency domain.

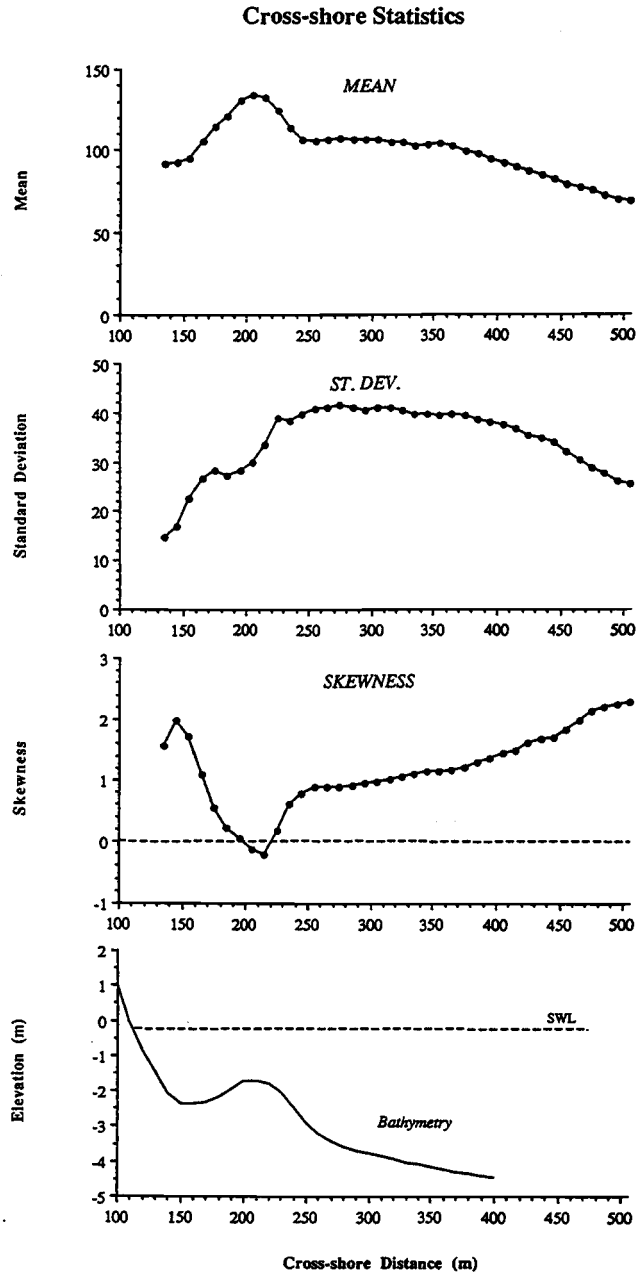

Figure IV.10. Mean, standard deviation, and normalized skewness of *I* from a cross-shore array spanning the width of the surf zone (Figure IV.8). The horizontal axis is cross-shore distance in meters relative to the FRF coordinate system. The approximate (smoothed) beach profile (from October 14) is shown in the bottom plot for reference. Skewness statistics are normalized by the variance to the 3/2 power.

Cross-shore Spectral Analysis

Spectral estimates of I are computed for 120 minute (demeaned) time series subsampled at 0.5 Hz. The time series is first broken up into 50-percent-overlapping, 2400 point segments, quadratically detrended, and windowed with a Kaiser-Bessel cosine taper to reduce leakage (see Harris, 1978). Transformed (FFT) ensembles are averaged and adjacent frequency bands merged to achieve the desired degrees of freedom (d.o.f.). The frequency bandwidths and 95% confidence intervals are shown in the figures.

Example auto power spectra of I (54 d.o.f.) are shown in Figure IV.11. Spectra are computed from 10 cross-shore locations along the main instrument line, eight corresponding to the position of surf zone instruments (x = 145, 170, 190, 207, 226, 245, 295, and 370 m) and two from further offshore (x = 455 and 505 m). The spectra were sampled from two camera views indicated in Figure IV.3. Spectral power is not normalized to account for gain and offset differences in each camera.

Each power spectrum in Figure IV.11 shows a prominent narrow peak at $f \approx 0.08$ Hz, corresponding to the peak incident frequency ($f_p \approx 0.083$ Hz; Figure IV.4). Just seaward of the shore break (x = 145 m, ~25 m offshore) this peak is not as pronounced since wave breaking is less vigorous and produces a smaller incident band signal in the video. There is considerable low frequency energy in all spectra throughout the surf zone, as has been observed in previous video time series (Lippmann and Holman, 1991).

If modulations in the breaking wave field are associated with wave groups, with periods long compared to peak incident periods, then we expect low frequency energy in I to be coupled with incident frequencies. Coupling between frequencies in the power spectrum of any given time series are detected with the third order spectrum, the bispectrum, B (Hasselmann, 1962; Haubrich, 1965; Kim and Powers, 1979; Elgar and

Figure IV.11. Example power spectra of I sampled at 10 positions along the main instrument line (y = 986 m), with the 8 landward most spectra corresponding to the locations of surf zone instruments (Figure IV.3). Cross-shore sensor positions in the FRF coordinate system are indicated on the plots. Spectra are computed with 56 d.o.f. with frequency bandwidth (0.0039 Hz). 95% confidence intervals are shown on the upper left hand plot. All spectra show a significant peak at the peak frequency ($f_p \approx 0.08$ Hz), as well as substantial low frequency energy ($f <\sim 0.05$ Hz) throughout the surf zone.

Intensity Spectra

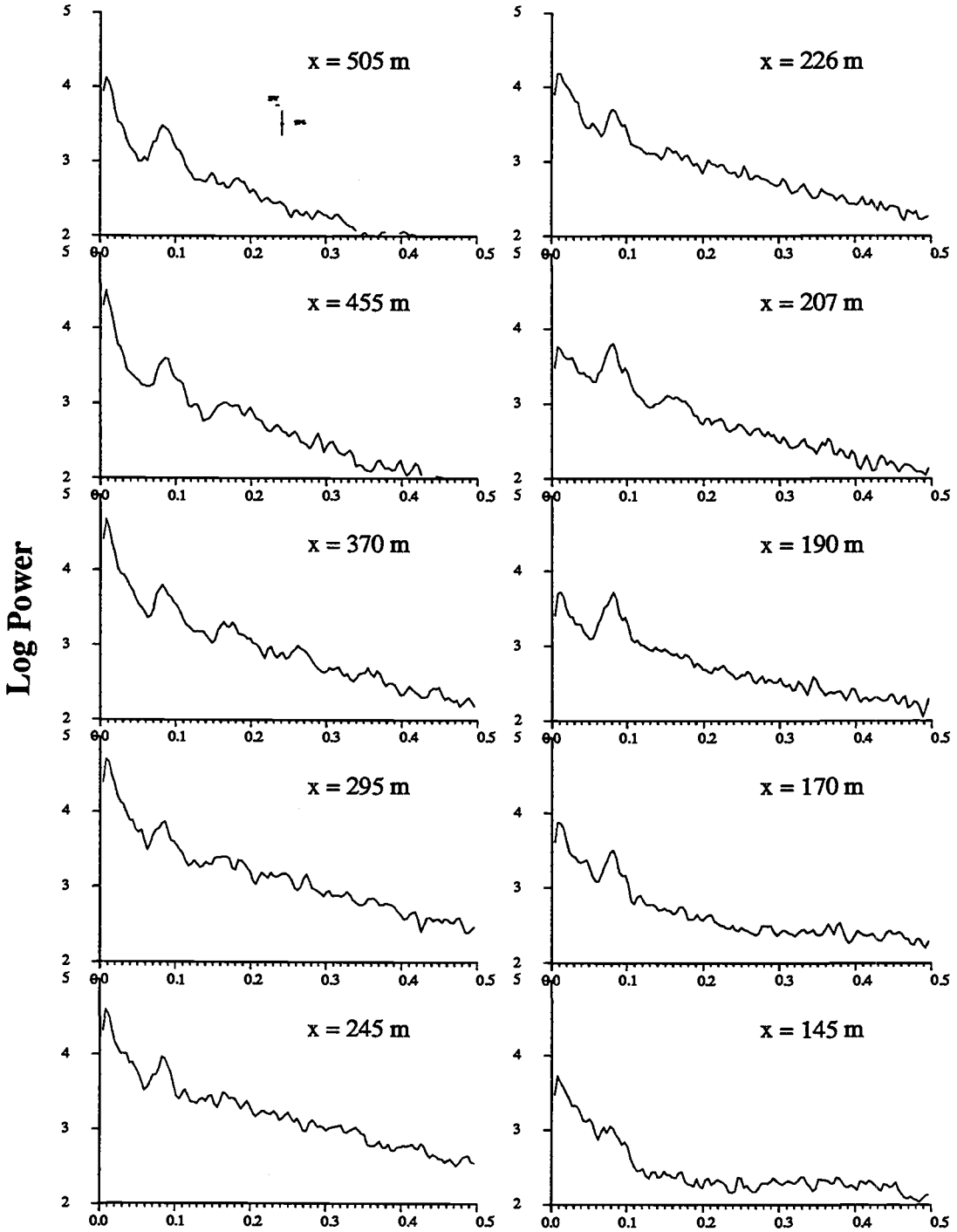

Guza, 1985a; and others), computed by

$$B(f_k, f_j) = \mathrm{E}\left[A_{f_k} A_{f_j} A^*_{f_k+f_j}\right] \tag{IV.7}$$

where E[] is the expected value operator, A_f are the complex Fourier coefficients at each frequency, j and k are indices denoting different f in the spectrum, and * indicates the complex conjugate. The bispectrum is a measure of lowest order triad interactions between a pair of primary waves (f_1, f_2) and a secondary wave, f_3

$$f_1 \pm f_2 = f_3 \tag{IV.8}$$

The bispectrum has been used extensively in intermediate water depths to resolve nonlinear coupling between incident and low frequency waves (*e.g.* Elgar and Guza, 1985a; Okihiro, *et al.*, 1992; Elgar, *et al.*, 1992) and to separate free waves from nonlinearly generated high frequency forced waves (Herbers and Guza, 1991, 1992). In addition to high frequency forced waves, the sum interaction in (IV.8) generates harmonics which are phase-locked to the primary, and thus are not free and travel at the phase speed of the primary (Elgar and Guza, 1985b). Since the breaking wave peaks in I time series (Figures IV.6 and IV.7) are very non-sinusoidal, we expect to see strong coupling between the primary frequency, f_p, and harmonics: $2f_p$, $3f_p$, etc. On the other hand, the (small) difference frequencies are associated with coupling between two waves of nearly the same frequency, and a secondary low frequency wave. In time series where both sum and difference interactions contribute to the nonlinearities, the bispectrum is difficult to interpret because it is incapable of distinguishing between the two.

The degree of the coupling is quantified with the bicoherence, b, the normalized bispectrum given by Kim and Powers (1979)

$$b^2(f_1,f_2)=\frac{|B(f_1,f_2)|^2}{\mathrm{E}\left[\left|A_{f_1}A_{f_2}\right|^2\right]\mathrm{E}\left[\left|A_{f_3}\right|^2\right]} \qquad \text{(IV.9)}$$

Important to the computation of b is the manner in which the Fourier coefficients are computed and then averaged. For the results presented, 7200 second time series subsampled to 2 Hz were transformed into the frequency domain using 512 point segments (with 50% overlap) in which each segment was demeaned, quadratically detrended, and then windowed with a Kaiser-Bessel cosine taper. The Kaiser-Bessel taper has the attractive property that sidelobes are extremely small, and thus reduces spurious bicoherences due to spectral leakage (although the frequency resolution of the main lobe is reduced; Harris, 1978). Ensembles were averaged (no frequency merging was applied) to yield ~56 d.o.f. All bicoherence plots show only contours of b (at 0.05 increments) which are greater than the 95% significance level ($b_{crit} = 0.33$) computed as $\sqrt{6/\text{d.o.f.}}$ (Kim and Powers, 1979). Elgar and Guza (1988) show with synthetic simulations that this is a fairly conservative estimate, and is actually closer to the 99% significance level.

Figure IV.12 shows example bicoherence estimates from I sampled in the trough of the bar ($x = 188$ m) and in the fluctuating region of the surf zone ($x = 370$ m). Due to the symmetry properties of B, only the unique portion of b is shown (see Kim and Powers, 1979). Figure IV.12 indicates that strong coupling exists between the primary frequency (0.08 Hz) and the higher harmonics in both regions of the surf zone. Strongest coupling occurs at the self-self interaction (f_p, f_p), $b \approx 0.61$ and $b \approx 0.68$, and the interaction between the primary and first harmonic (f_p, $2f_p$), $b \approx 0.51$ and $b \approx 0.55$, for the inner and outer surf zone data, respectively. Harmonic coupling arises from the sharp (non sinusoidal) peaks in the time series records (Figures IV.6 and IV.7). In the trough, there is a distinct lack of coupling between incident ($f \geq f_p$) and lower frequencies ($f << f_p$),

Figure IV.12. Example bicoherence estimates (lower panels) for I sampled in the trough (x = 188 m; left panels) and in the region of fluctuating surf zone width (x = 370 m; right panels). Power spectra are also shown in the top panels for comparison (same format as in Figure IV.11). Bicoherences greater than the 95% significance level for 56 d.o.f. (b = 0.33) are plotted in bi-frequency space with f_1 along the horizontal axis and f_2 along the vertical axis.

Intensity Bispectra

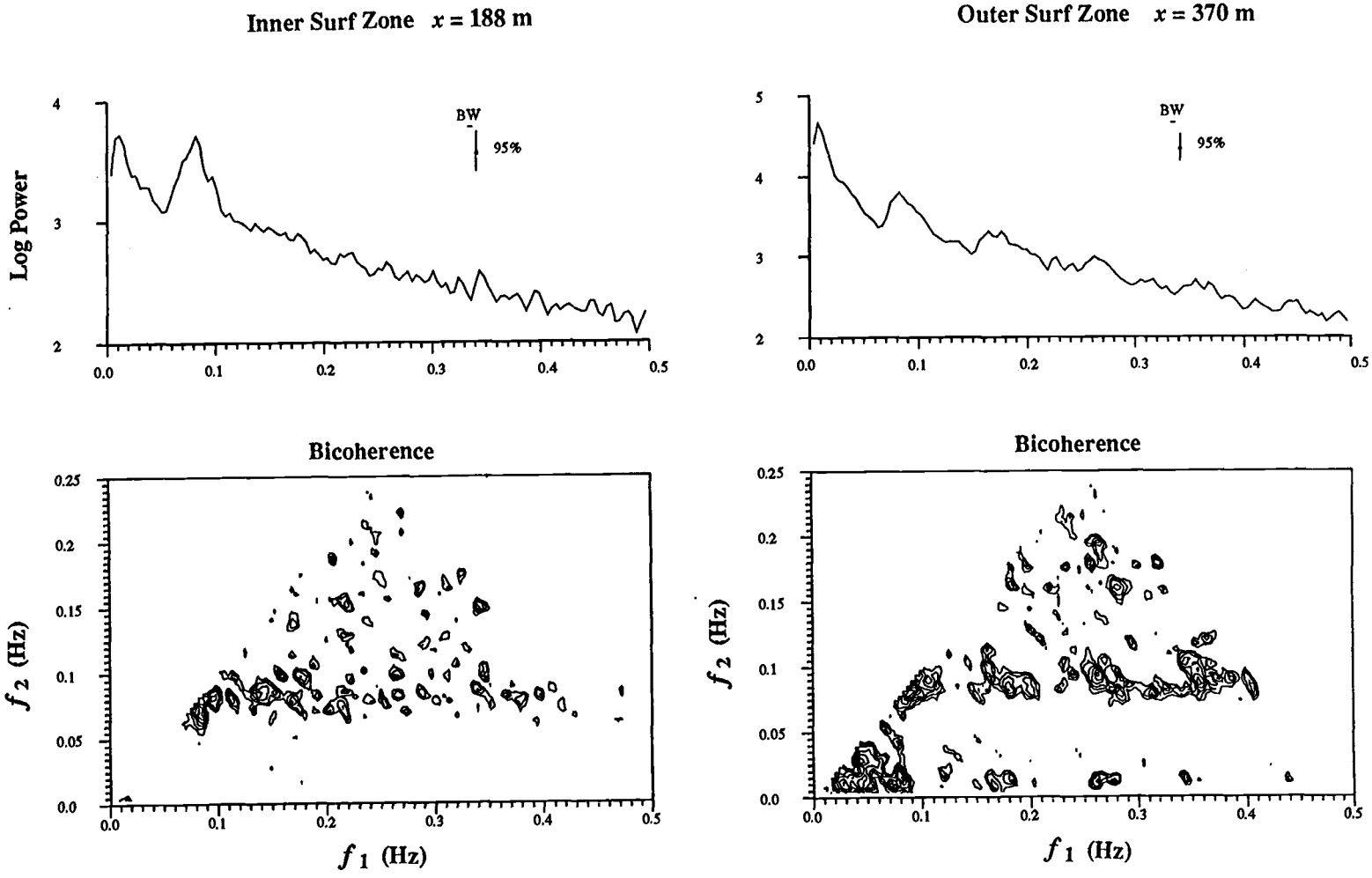

suggesting that the origin of infragravity energy in I is derived from free waves not directly associated with incident wave breaking. However, seaward of the saturated inner surf zone, widespread bicoherence at low f reveals strong coupling to f_p. Highest coupling ($b \approx 0.62$) occurs at $(f_1, f_2) \approx (0.082, 0.015)$. This result is typical of all I time series sampled in the fluctuating region of the surf zone, demonstrating that low frequency spectral energy in I is coupled to modulations in incident wave breaking patterns, and is thus associated with wave group time scales.

In the cross-shore array of I shown in Figure IV.8, wave group modulations can be followed all the way to the bar crest. The phase propagation of the groups can be quantified using frequency domain (complex) empirical orthogonal functions (CEOF), previously applied to nearshore data by Holman and Bowen (1984). In CEOF analysis, eigenvectors of the cross-spectral matrix are computed at each frequency (Wallace and Dickinson, 1972), analogous to more traditional time domain EOF analysis (Priesendorfer, *et al.*, 1981). Thus the data are decomposed into orthogonal factors representing the amplitudes and phases at each frequency as a function of cross-shore distance.

Figure IV.13 shows the first CEOF from the peak incident frequency ($f_p \approx 0.082$ Hz), and also from the low frequency peak ($f \approx 0.015$ Hz) observed in all the power spectra across the surf zone (Figure IV.11). Only the first factor is shown since it contains the greatest proportion of the variance (63.7% at f_p and 45.9% at low f), and because orthogonality constraints in the decomposition of the data make interpretation of higher modes unclear. CEOF phases are relative to cross-shore position (the absolute value of individual phase estimates is arbitrary), and amplitudes are normalized by the spectral power within each frequency band. Also shown are estimated (relative) phase

Figure IV.13. Frequency domain empirical orthogonal functions (CEOF) from I at the peak frequency ($f_p \approx 0.082$ Hz; left panel) and also the low frequency peak in the power spectra ($f_p \approx 0.015$ Hz; right panel), plotted as a function of cross-shore distance. Phases are shown in the upper panels and normalized amplitudes in the middle panels. The approximate (smoothed) beach profile (from October 14) is shown in the lower panels for comparison. Predicted relative phase relationships (from shallow water theory) for shoreward progressive incident waves are indicated with the dashed lines in the phase plots .

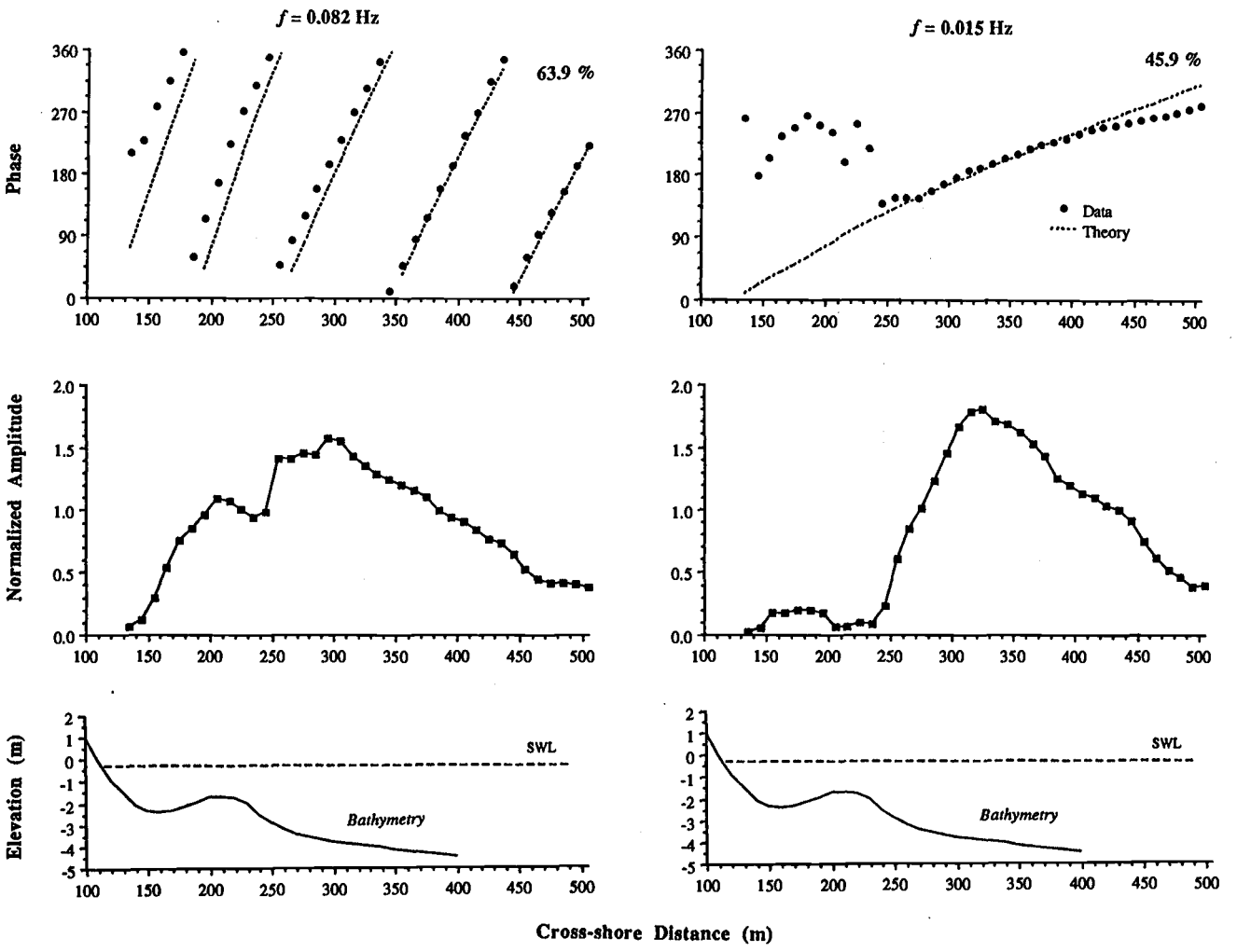
1st f-Domain EOF
f = 0.082 Hz
63.9 %
f = 0.015 Hz
45.9 %
Data
Theory
Phase
Normalized Amplitude
Elevation (m)
SWL
Bathymetry
Cross-shore Distance (m)

relationships for phase speeds, C_p, predicted by shallow water (Solitary) wave theory

$$C_p = \sqrt{g(h + H_{\text{rms}})} \tag{IV.10}$$

where H_{rms} is the root mean square wave height. H_{rms} across the surf zone was estimated using the random wave dissipation model of Thornton and Guza (1983), shown previously to well predict the energy decay of incident wave energy in the surf zone (see also Thornton and Guza, 1986; Whitford and Thornton, 1988). The predicted phases, $\phi(x)$, in Figure IV.13 were computed by

$$\phi(x) \approx \frac{2\pi f \Delta x}{\overline{C}_p} \tag{IV.11}$$

(Thornton and Guza, 1982) where $\overline{C}_p$ is the mean phase speed of the peak incident waves over the distance, Δx (10 m).

For f_p, predicted and observed phases are matched at the most seaward location to allow comparison across the surf zone. The first CEOF shows a clear negative phase ramp, indicating shoreward propagating progressive (breaking) incident waves which are coherent all the way through the surf zone. The data are reasonably predicted by (IV.10), although near the bar crest and in the trough the theory systematically overpredicts the observed phase speeds (*i.e.*, steeper phase ramps), consistent with previous comparisons with video derived data (Lippmann and Holman, 1991).

At the low frequency peak ($f \approx 0.015$ Hz), the cross-shore phase structure in the first CEOF also has a linear trend, but only seaward of the bar crest. In this region theoretical group velocities are in excellent agreement with the data (although deviates slightly in the far reaches of the surf zone, $x > \sim 425$ m). Predicted phases relationships (IV.11) are best fit to the data in the region of (approximately) constant celerity, between x

$\approx$ 255-425 m. The average phase speed between x = 255-425 m, $\overline{C}_p \approx 7.3$ m/s, is very nearly the same as predicted by Solitary theory, $\overline{C}_p \approx 7.5$ m/s. The phase relationships are consistent with a shoreward propagating group modulation in the breaking incident wave field traveling at the phase speed of the incident waves. Furthermore, the very small CEOF amplitudes over the bar crest indicate that low frequencies observed in I in this region are uncoupled to wave groups seaward of the bar, a consequence of energy saturation over the bar.

Cross-spectra of Colocated I, u, v, and η

The frequency relationship between I and the fixed *in situ* instruments are observed in the cross-spectrum. Cross-spectra obtained at x = 170 m (~50 m offshore in the trough of the bar) between colocated I-η, I-u, and I-v are shown in Figure IV.14. Cross-spectra with u and η show high coherence ($r^2 > 0.7$) at the peak frequency. Peak coherence with v is slightly less ($r^2 \approx 0.32$) because of the nearly normal angle of incidence. Significant coherence ($r^2_{crit} \geq 0.11$ for the 95% significance level) at higher frequencies in cross-spectra with η and u arise because the shape of the waveforms in the respective time series at this location are very similar (Figure IV.6).

There is also significant coherence between I and η at selected low frequencies, 0.015 Hz ($r^2 \approx 0.28$) and 0.038 Hz ($r^2 \approx 0.41$), which correspond to energetic frequencies in η. Similarly, strong coherence exists between I and u, $r^2 \approx 0.52$ and 0.40, at selected low frequencies, 0.025 Hz and 0.05 Hz, respectively, corresponding to energetic frequencies in u, and additionally at very low f ($r^2 \approx 0.24$). Note that the coherent frequencies in the two cross-spectra are not the same, consistent with the cross-shore nodal structure associated with standing infragravity waves, in which are η and u are 90° out of phase and thus have nodes at different offshore distances. Interestingly, significant coherence between I and v ($r^2 \approx 0.63$) occurs only at very low frequency

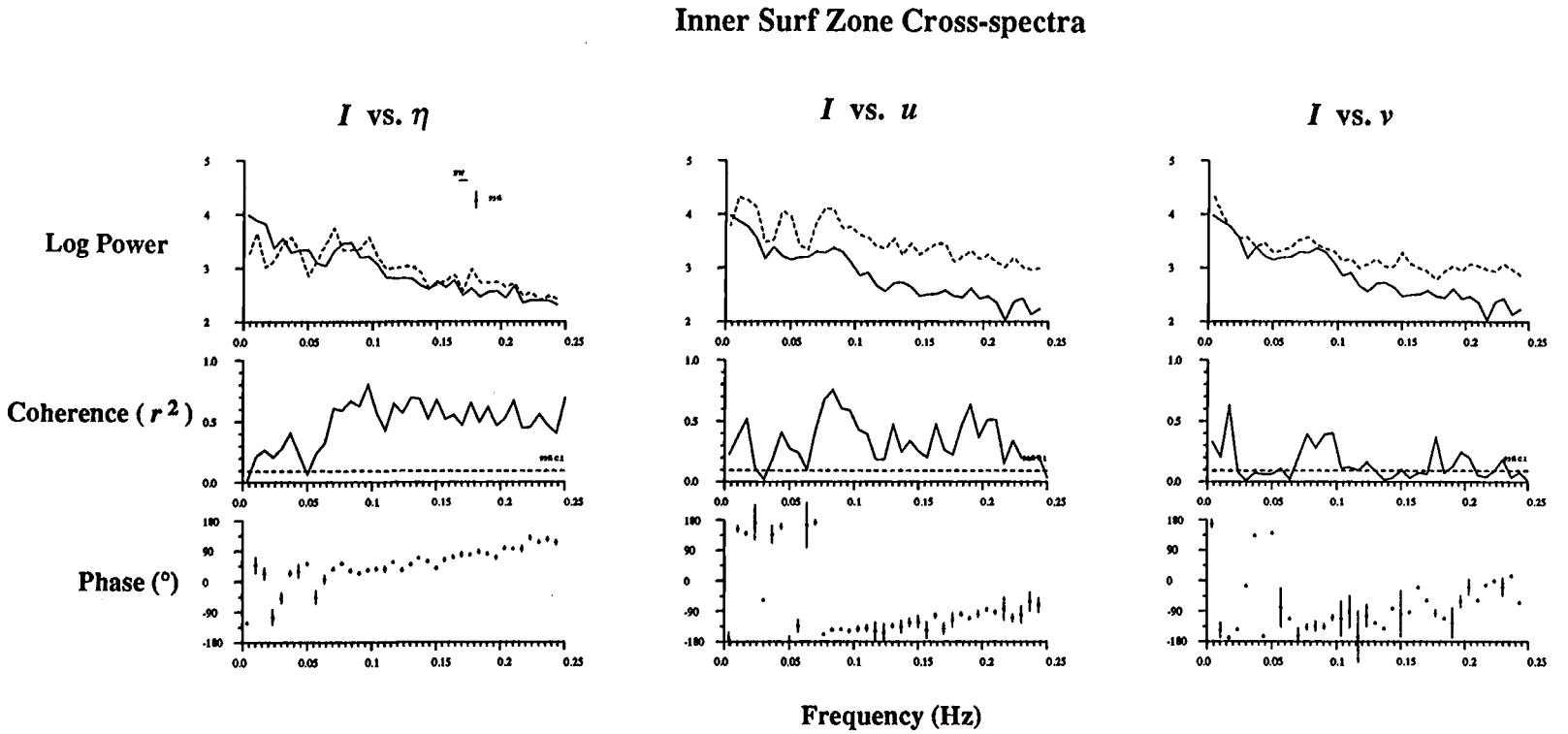

Figure IV.14. Coherence squared spectra (lower panels) between I-η (left panel), I-u (middle panel), and I-v (right panel) from the trough of the bar (x = 170 m). Comparison with h were taken at y = 986 m alongshore, whereas u and v comparisons are made at y = 926 m. The auto power spectra are shown in the top panels (on a log scale) for comparison, with the video spectra indicated with the solid line in all plots. The 95% significance level for 54 d.o.f. (r^2 = 0.11) on zero coherence is shown with the dashed line.

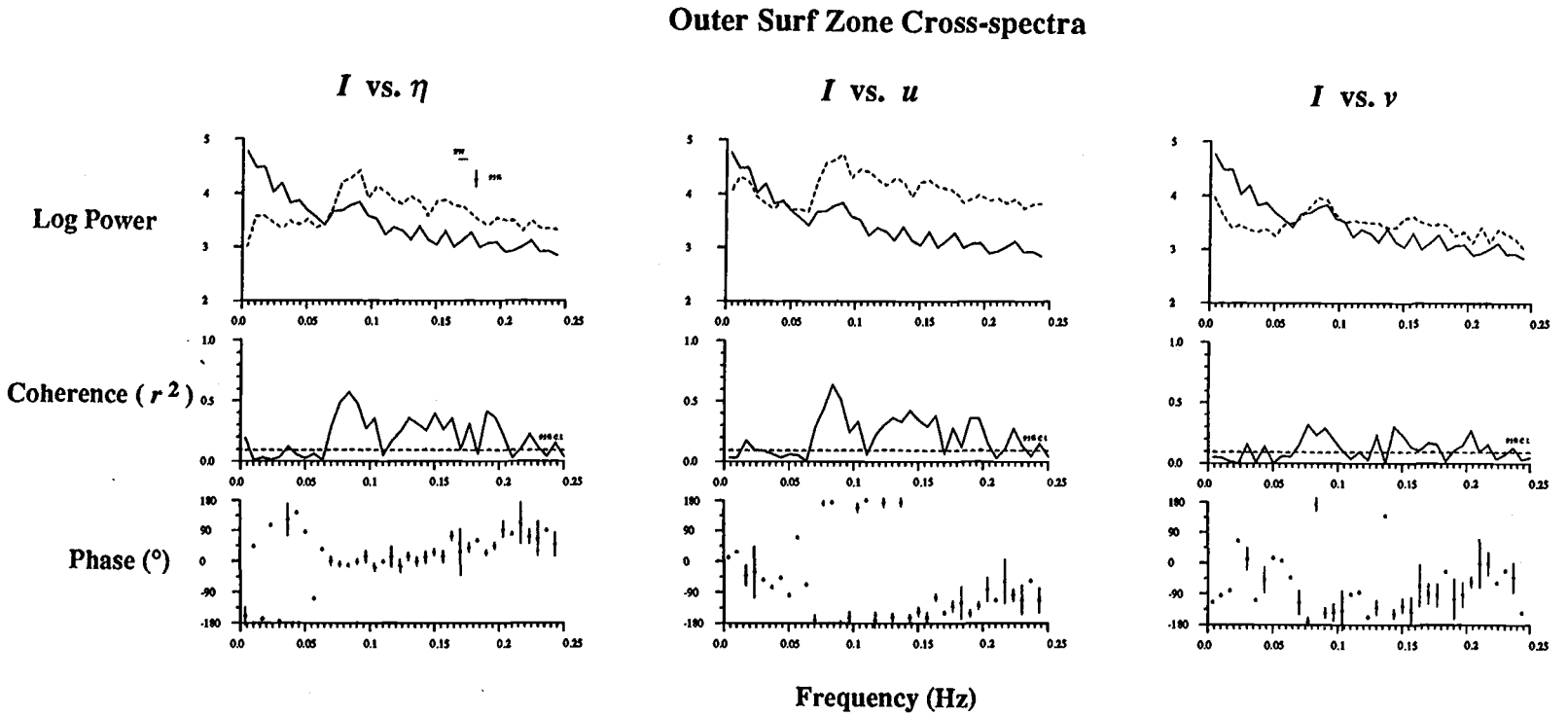

Figure IV.15. Same as Figure IV.14, except for comparison between instruments at $x = 370$ m ($y = 986$ m) approximately 150 m seaward of the bar.

(0.015 Hz), and is most likely derived from energetic shear waves (shown later; Bowen and Holman, 1989; Oltman-Shay, *et al.*, 1989).

Power and coherence spectra for I-η, I-u, and I-v in the offshore region at $x = 370$ m are shown in Figure IV.15. At the peak incident frequency I is coherent ($r^2 > 0.6$) with η and u, and also with v ($r^2 \approx 0.32$). At higher harmonics coherence is less than in the trough due to the predominantly different shapes of the waveforms in the respective time series (Figure IV.7). Strikingly, low frequencies in I are not significantly coherent either u, v, or η, in marked contrast with results from the trough region (Figure IV.14). This result indicates that shoreward progressive group modulations in the breaking wave field, coupled to incident frequencies, are not significantly coherent with the local flow field.

Wavenumber Analysis

The longshore spatial variation in the breaking wave field is investigated with alongshore arrays of I. Figure IV.16 shows an alongshore array of I time series sampled at $x = 500$ m (all in the same camera view) with an alongshore separation of 10 m, beginning at $y = 976$ m and ending at $y = 1206$ m. The time series are stacked vertically with longshore distance increasing northward toward the top of the figure. The arrival of wave groups is seen as large signals which arrive at each sensor with a time lag dependent on the alongshore phase determined by the local wave angle. Large spatial modulations clearly exist in the breaking wave field with time scales on the order of the groups. The first 3 moments of each time series in the array are shown in Figure IV.17 as a function of longshore position (compare with the cross-shore statistics; Figure IV.10). All statistics show very small variation alongshore, indicating spatial homogeneity in the wave field. In fact, all analyzed longshore arrays seaward of the crest show similar results.

Quantifying the spatial dependence on temporal modulations in wave breaking is accomplished with analysis of spatially lagged arrays using high powered spectral estimators (Davis and Regier, 1977; Huntley, *et al.*, 1981; Pawka, 1983; Oltman-Shay

Figure IV.16. An alongshore array of I (for a 120 minute record) sampled at 20 m alongshore intervals at x = 500 m from y = 976 m and extending northward to y = 1206 m. Time series are stacked vertically with increasing longshore distance to the north toward the top, shown with the distance scale on the right hand side of the plot. The vertical axis is non-dimensional image intensity scaled to +/- 3 standard deviations. The occurrence of wave group modulations in breaking wave patterns is clearly seen.

Longshore Array of Intensity Time Series $x = 500$ m
Intensity (non-dim)
Time (secs)
0
1800
3600
5400
7200
Longshore Distance (m)
1000
1100
1200

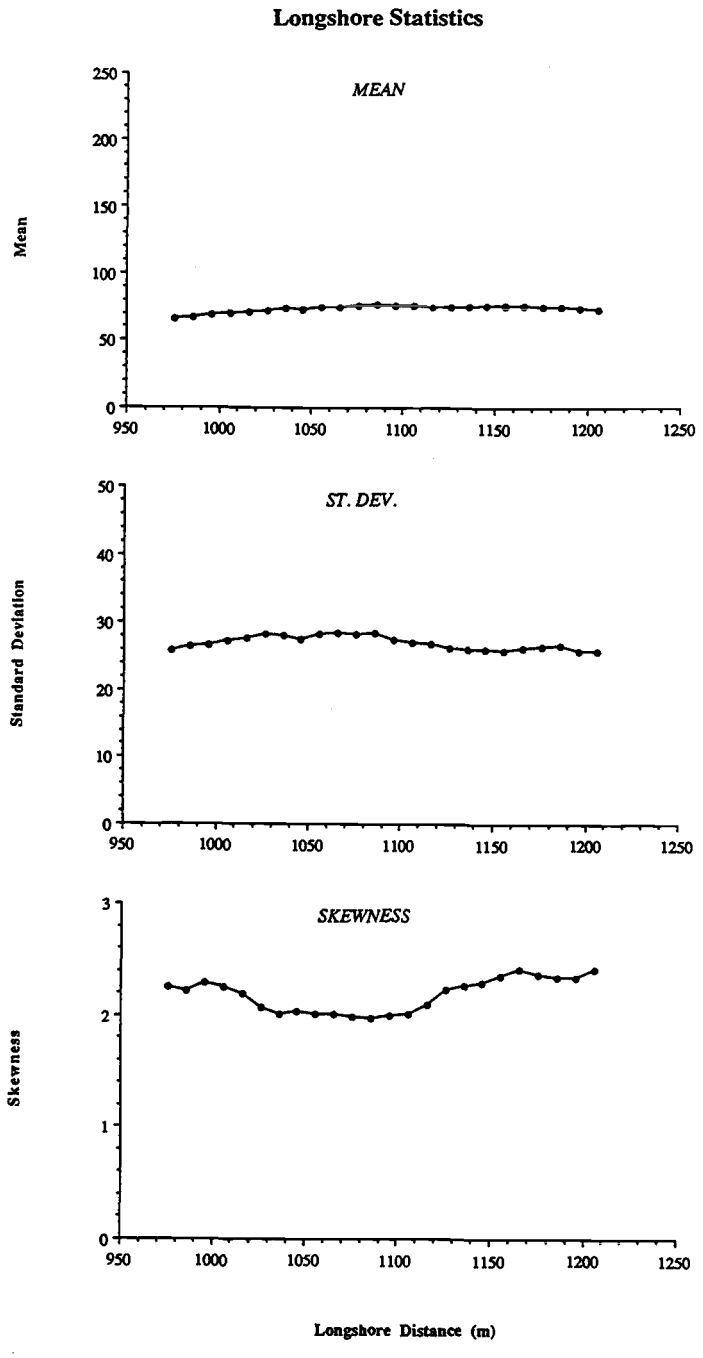

Figure IV.17. Mean, standard deviation, and normalized skewness of I from an alongshore array spanning 230 m sampled at $x = 500$ m corresponding to time series shown in Figure 16. The horizontal axis is longshore distance in meters relative to the FRF coordinate system. Skewness statistics are normalized by the variance to the 3/2 power.

and Guza, 1987). Frequency-alongshore wavenumber (σ-k_y) spectra from I arrays (consisting of 5-7 alongshore locations) are qualitatively compared with u and v arrays in both the trough and offshore regions, as well as with runup elevation time series, R. σ-k_y estimates are computed using the Iterative Maximum Likelihood Estimators (IMLE) of Oltman-Shay and Guza (1987). The IMLE estimator has been widely applied to surf zone data and has been shown to have excellent resolving capabilities for typical incident and low frequency wave motions (Oltman-Shay and Guza, 1987; Oltman-Shay, *et al.*, 1989; Howd, *et al.*, 1991; and others).

Figure IV.18 shows the σ-k_y spectra (54 d.o.f.) from I, u, and v from the alongshore trough array, and from a similarly spaced R array at the shoreline (Figure IV.3). The shaded boxes represent concentrations of variance in σ-k_y space, with darker shades representing higher power (percentages are given in the legend on the figure). The height of the boxes along the vertical axis are determined by the frequency bandwidth in the power spectra. Current meter data were generated from ~4 hour records, and thus have finer frequency resolution than video derived data (from ~2 hour records) with the same d.o.f. The width of the boxes along the horizontal axis are determined by the half-power wavenumber bandwidth of the spectral peaks. The fundamental wavenumber bandwidth is the same for all spectra (0.0004 m^{-1}). Positive wavenumbers indicate waves progressing to the south in the FRF coordinate system. Also shown are approximate theoretical dispersion curves for a plane beach (Eq. IV.1 with $\beta = 0.04$) for the lowest 4 edge waves (without consideration of topographic influences or longshore current modifications; Howd, *et al.*, 1992).

The σ-k_y spectrum for I indicates concentrations of energy within the high mode edge/leaky wave regime (small k_y), very similar to σ-k_y spectra of u and R. Northward and southward propagating infragravity waves are also evident in v. Additionally, I data show concentrations of energy at σ-k_y pairs with celerities too slow (k_y too large) to be gravity waves (a mode zero edge wave has the lowest celerity of any gravity wave).

Figure IV.18. IMLE derived σ-k_y spectra observed in the trough (x = 170 m; Figure 3) for I (upper left), u (lower left), and v (lower right), as well as for similarly spaced shoreline runup (upper right). The vertical axis is frequency (Hz) and the horizontal axis is reciprocal wavelength (m^{-1}). The percent power in each σ-k_y bin is indicated by the relative shading shown by the scale at the bottom of the plot.

Figure IV.19. Same as Figure IV.18, except for I sampled from an alongshore array at x = 370 m and for u and v from the longshore array on the seaward flank of the bar (x = 245 m).

Outer Surf Zone σ-k Spectra

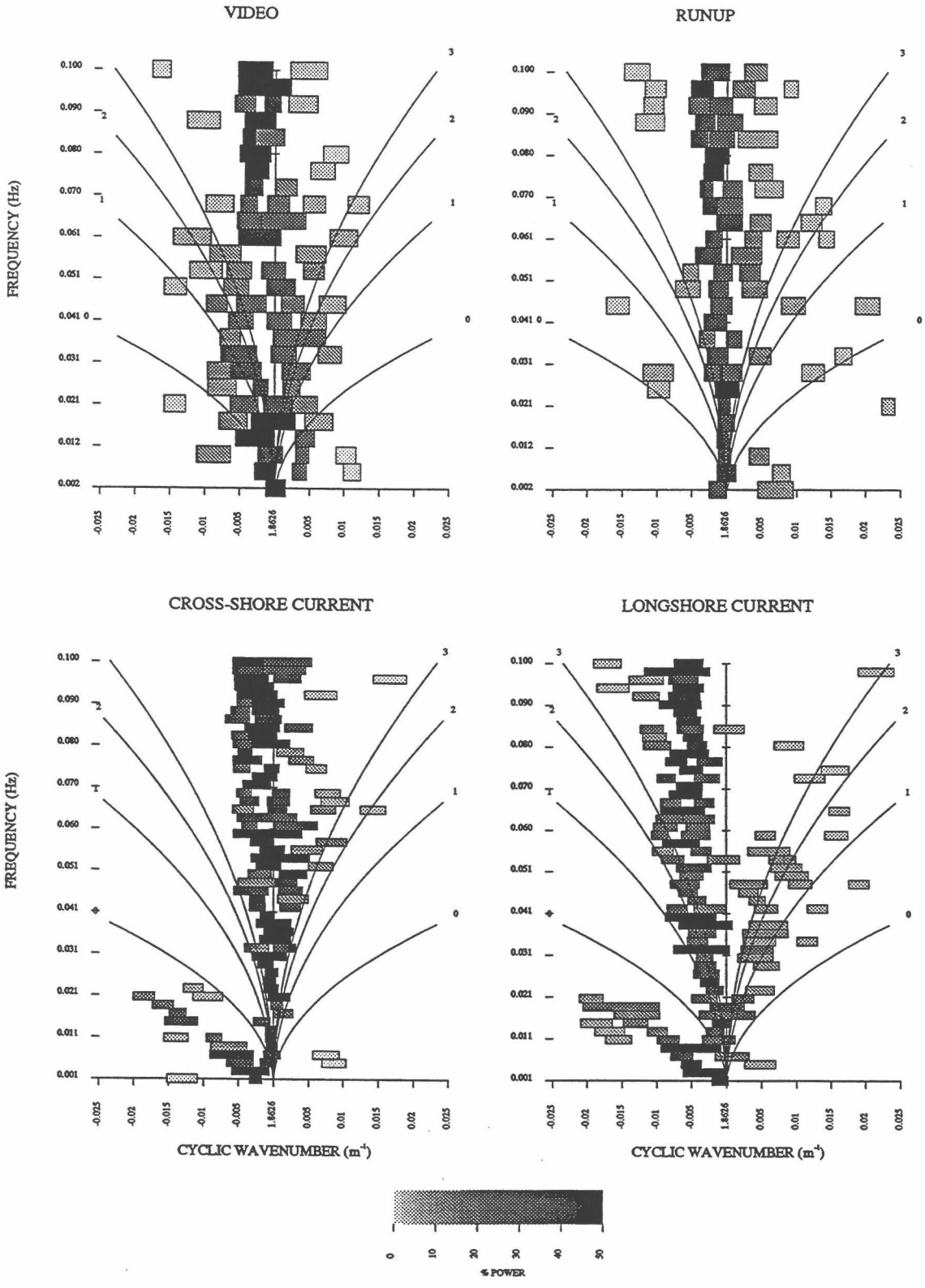

These slowly propagating waves have σ-k_y structure characteristic of shear waves (instabilities of the longshore current) observed previously in analysis of similarly sampled current meter data (Oltman-Shay, *et al.*, 1989; Howd, *et al.*, 1991). Shear waves are also observed clearly in u and v. Since the shear wave signals have negative k_y, the instabilities are progressing to the north in the direction of the strong mean longshore current ($\overline{V} \approx 1.2$ m/s), as with previous observations of shear waves. The shear wave signature is lacking in R, consistent with the rigid lid assumption (Bowen and Holman, 1989), and noted previously in other runup field data (Holman, *et al.*, 1990).

Figure IV.19 shows σ-k_y spectra of I sampled at $x = 370$ m, and u and v from the longshore array on the seaward flank of the bar ($x = 245$ m) and similarly spaced R at the shoreline (recreated from Figure IV.18 for reference). High mode edge and leaky wave energy dominates the gravity wave regime in u, whereas both up and down coast traveling edge waves are evident in v. Shear waves are also observed in both u and v spectra. The σ-k_y spectrum of I give good estimates of the incident wave angle (from k_y), also shown previously by Lippmann and Holman (1991). The video data, however, show little indication of resonant modes, nor any shear waves. In fact, energy distribution in I appears very broad-banded across σ-k_y space. Although the incident waves are predominantly arriving from the south at a steep angle to the normal (with a narrow angular spread; Figure IV.4), energy is spread out over both positive and negative wavenumber throughout the infragravity band, although with some asymmetry to the north (negative k_y, also clearly seen in v).

Cross-spectra of Offshore I and Inshore u, v, η, and R

Figure IV.20 shows coherence spectra between I sampled $x = 370$ m, in the fluctuating region of the surf zone, and η, u, and v in the trough of the bar ($x = 170$ m) and at the shoreline (runup). Significant coherence is observed at the peak incident frequency, indicating that the breaking wave field progressing shoreward has coherent

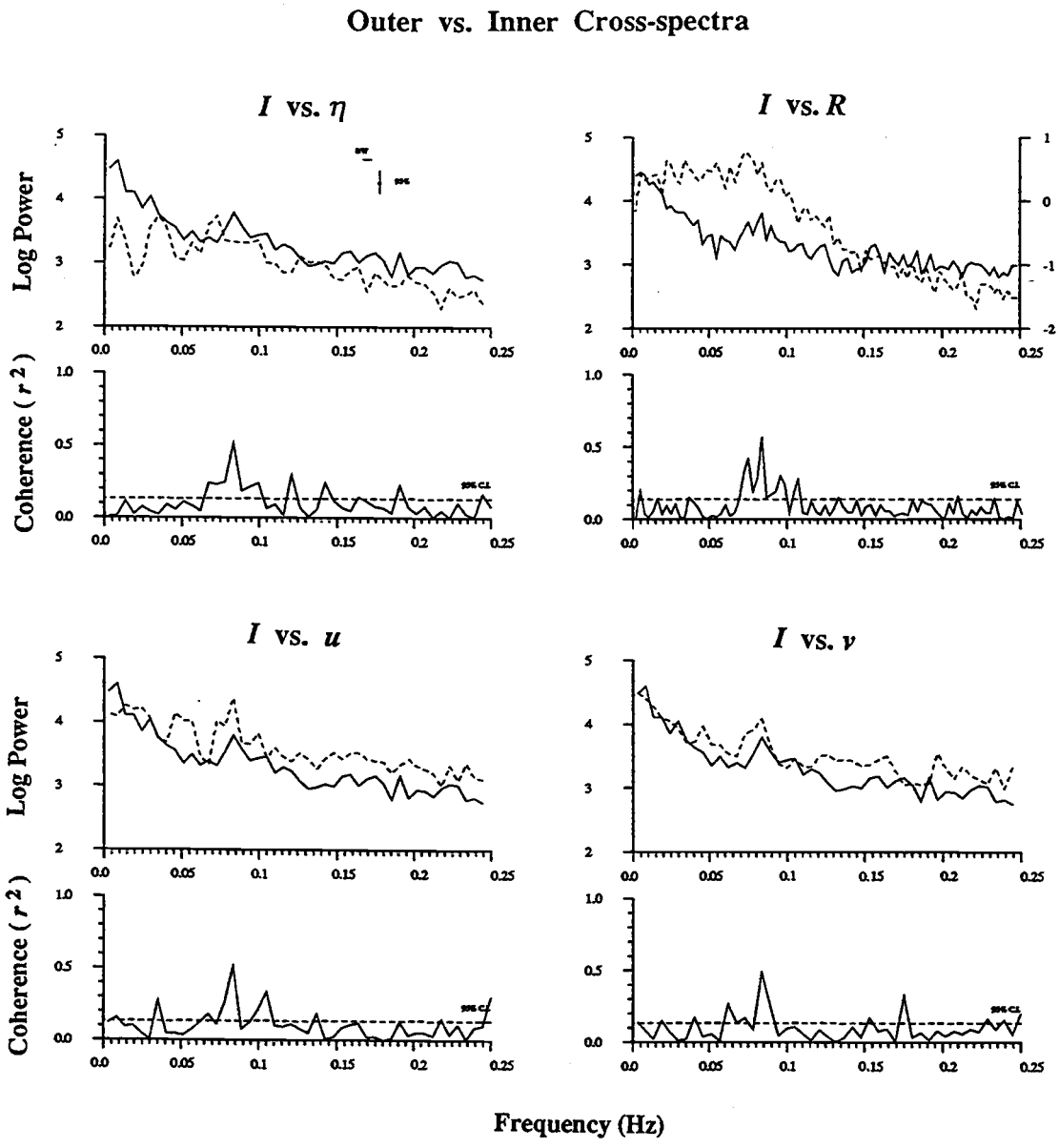

Figure IV.20. Squared coherence (lower panels) between I sampled in the fluctuating region of the surf zone (x = 370 m) and u, v, and η in the trough of the bar (x = 170 m) and R at the shoreline. Power spectra are shown in the upper panels for comparison, with I spectra shown in each plot with the solid line. All spectra are computed for 54 d.o.f. The 95% significant level (r^2 = 0.11) for zero coherence is shown with the dashed lines in the coherence plots.

structure all the way to the shoreline (mentioned earlier, Figure IV.13), a consequence of the waves being very long crested and narrow banded (for more broad banded days the spatial coherence drops off over much smaller distances). Significantly, no coherence is observed in the infragravity band of the spectra. Comparisons with I from a wide range of locations in the outer surf zone and u, v, and η throughout the inner surf zone show similar results, and indicates that coupling between wave groups seaward of the bar and free infragravity waves in the trough are absent in the data.

DISCUSSION

Coupling and Resonance of the System

The data show that low frequency energy in I are coupled to incident wave breaking seaward of the bar crest, and thus represents amplitude modulations associated with wave groups. Group modulations propagate landward at the phase speed of the incident waves, consistent with linear shoaling expectations. The spatial scales of the modulations are also quantified by investigating the longshore phase relationships in the wave breaking distributions, and show both northward and southward propagating modulations despite the unidirectional incident wave field. Thus the scales of incident wave breaking are reasonably approximated with I, and provides a useful parameterization of the temporal and spatial scales of forcing by group modulations, $\mathbf{F}(x,t)$ (Eq. IV.5).

Coupling between time scales of I in the fluctuating region of the surf zone and with both local and remote (in the inner surf zone) infragravity energy is not observed in the data (Figures IV.15 and IV.19). However, in this cross-spectral analysis we have considered only time scales of modulations, whereas (IV.5) indicates that any resonant edge wave response in the surf zone requires not only coupling with time scales but also spatial scales of the forcing, which may not have a single characteristic length scale. In fact, response to broad banded forcing (as in this data; Figure IV.19) will be dependent on the Q (resonance) of the system. In a high Q system (*i.e.*, bell) coherence would be reduced between stochastic forcing and free response, whereas in a low Q system with high damping coefficients, forced waves would tend to dominate and higher coupling might be expected. Field data in recent years show infragravity energy falling along predicted edge wave dispersion curves in σ-k_y space (*e.g.*, Huntley, *et al.*, 1981; Oltman-Shay and Guza, 1987; Howd, *et al.*, 1992), suggesting that resonant response is greatest and that the nearshore is typically a high Q system. Thus forced response in the nearshore currents, such as explored by Shemer, *et al.* (1991) and Fowler and Dalrymple (1990),

may be only secondary to resonant response, a result also reported by Bowen and Ngusaru (1991).

A further complication at the Duck beach is the presence of a prominent sand bar (Figure IV.5). Barred topography has been shown theoretically to substantially influence the behavior of infragravity waves (Kirby, *et al.*, 1981; Symonds and Bowen, 1984). Free wave response may be detuned from the modulating wave field by attraction of nodes or antinodes to the bar crest, preferentially selecting those frequencies which fit resonantly into the scales of the topography. Thus, wave forcing becomes decoupled from the flow field response.

Modulating Break Point Positions

In the surf zone, break point amplitudes are often taken as a linear proportion of the depth

$$H_b = \gamma h_b \tag{IV.12}$$

where H_b is the height (twice the amplitude) of the breaking wave, h_b is the water depth at the break point, and γ is a either a constant or a variable of O(1) (Miche, 1954). For a plane sloping bottom, $h_b = x_b \tan\beta$, breaking wave amplitudes can be expressed in terms of break point positions. Models based on forcing due to modulations in break point amplitudes are distinguished principally by the behavior of γ. In one type (*i.e.*, Foda and Mei, 1981; Schaffer and Svendson, 1988), break point positions are assumed constant, and the group modulations are allowed to progress to the shoreline. Thus, γ in (IV.12) is a temporal function of the amplitude modulation, in which γ is larger for the bigger waves. In the second type (*i.e.*, Symonds, *et al.*, 1982; Symonds and Bowen, 1984; Schaffer, 1990), γ is assumed constant, and break point position is the parameter that fluctuates.

Our data indicates that the initial break points vary over large distances, ranging from far (> 400 m) offshore for the largest waves to near the bar (~100 m offshore) for the smallest waves. Moreover, the group structure is substantially reduced by wave breaking in the inner surf zone, thus restricting group modulations to seaward of the bar. Thus constant γ more accurately describes the data, and is consistent with energy saturation in shallow depths (verified previously with field data; Thornton and Guza, 1982; Sallenger and Holman, 1985).

Advection of Residual Foam by Low Frequency Currents

Cross-shore distributions in mean I (Figure IV.10), the same quantity measured by time exposure images (*i.e.*, Figure IV.2), indicate highest average intensity occurs in the vicinity of the bar crest. Lippmann and Holman (1989a) showed that this was a result of both increased breaking over the bar and residual foam accumulation left behind after the passing of breaking waves. This residual foam can be advected by surface currents. The coherence structure between colocated video and current data in the trough (Figure IV.14), suggests that the low frequency signals in I landward of the bar are derived from currents advecting residual foam on the sea surface away from the bar crest, the source of greatest foam production. The strong shear wave signal (with no surface elevation signal) in the σ-k_y spectra (Figure IV.18) strongly suggests this behavior. The (weak) coherence between I and η at energetic frequencies in η indicates that bores on the crest of long waves have slightly higher intensity than in the wave trough. Although this may indicate wave-current interactions with infragravity waves, phase relationships between I-η and I-v are not easily predicted by any existing theory.

We observe coherence in the trough at low frequencies between I and fixed *in situ* instruments only on days with accumulations of residual foam, usually most heavily localized just landward of the bar crest (Lippmann and Holman, 1989a). Incoherent low frequencies in the trough were reported previously by Lippmann and Holman (1991),

who analyzed data obtained during DELILAH on the previous day (October 12, at ~1600 EST). Infragravity energy at this time was of the same order of magnitude as on the October 13, but with reduced shear wave energy. Residual foam on the 12th was also much less (assessed visually), suggesting that advection of foam by currents is the signal which is detected in video records, and that wave-current interactions only contribute secondarily.

Wave Breaking in the Trough

Recent models predicting longshore current profiles, $V(x)$, have been based on the ensemble distribution of incident wave dissipation, $\langle \varepsilon_b(x) \rangle$ (*e.g.*, Thornton and Guza, 1986; Whitford and Thornton, 1988). Incident wave breaking is assumed to cease shoreward of the bar crest due to increasing depths in the trough. Thus model predictions over barred profiles suggest that longshore currents are strongest on the seaward flank of the bar where maximum incident wave dissipation occurs. However, recent observations of $V(x)$ at Duck suggests that the maximum current often occurs in the trough, in direct conflict with the dissipation models (Whitford and Thornton, 1988; Howd, *et al.*, 1992). Recent efforts to adjust the predicted cross-shore distribution of $V(x)$ have focused on various mixing mechanisms, including longshore current interactions with undertow (Putrevu and Svendsen, 1991), shear wave dynamics (Dodd and Thornton, 1990; Putrevu and Svendsen, 1992), and incident wave dissipation which lags the production of turbulence (*e.g.*, Roelvink and Stive, 1989; Church and Thornton, 1991).

The decay of wave height across a barred profile is well predicted by the model of Thornton and Guza (1983). However, the model assumes implicitly that no time lag exists between the production of turbulent kinetic energy by wave breaking and actual energy dissipation (a point made previously by Roelvink and Stive, 1989). Our observations of wave breaking across the width of the surf zone (Figure IV.8) indicate that, although the initiation of breaking is confined to depths seaward of the bar, wave

breaking does not cease immediately shoreward of the crest, but continues into the trough. If the foam and bubbles on the face of breaking waves and bores (detected with video time series) are related to turbulent kinetic energy, then wave breaking in the trough suggests a possible further mechanism for mixing momentum from the region of highest production of turbulent kinetic energy over the bar crest, into the trough where often the maximum longshore current is observed (*e.g.*, Whitford and Thornton, 1988; Howd, *et al.*, 1992).

CONCLUSIONS

A video based technique is presented which accurately measures the temporal and spatial scales of wave breaking across the width of the surf zone. The technique is based on the gray tone (intensity) contrast between the lighter foam and bubbles created by actively breaking waves and bores, and the darker, surrounding non-breaking water. Thus video records of the surf zone contain visible-band time histories of the spatial scales of wave breaking distributions. Quantification of images is accomplished with an image processing system, in which images are digitized at discrete pixels corresponding to defined field coordinates .

Data were obtained from a very narrow banded ($f_p \approx 0.083$ Hz), unidirectional day ($\alpha_0 \approx 24°$ CW) during the DELILAH experiment. In addition to energetic incident frequencies associated with the actively breaking incident waves, considerable low frequency energy was observed in all video time series, from the outer portions of the surf zone to the trough of the bar. In the outer surf zone (*i.e.*, region of fluctuating surf zone width) wave breaking at incident frequencies is coupled to low frequency energy, indicating that modulations in incident break point amplitudes are associated with wave group time scales. Spatial scales of amplitude modulations are estimated from large alongshore arrays, and indicate that forcing at group (infragravity) frequencies is broad banded across wavenumber-frequency space. Considering the very narrow band day analyzed, the lack of evidence for a preferred length scale associated with the incident wave envelope is striking.

Comparisons with video data are also made with colocated sea surface elevation and bi-directional current measurements. High coherence at the peak incident periods between video and fixed *in situ* instruments is observed, particularly in the inner surf zone where nearly all the waves are breaking. In the trough of the bar, where wave energy is saturated and amplitude modulations are greatly reduced, significant coherence was

observed at selected low frequencies coinciding with peaks in the pressure and velocity records, as well at very low frequency. Wavenumber analysis indicates that these low frequencies are energetic infragravity (standing) waves or shear instabilities of the longshore current. The origin of the signal is derived from advection by currents of residual foam on the sea surface away from the region of maximum foam production (at the bar crest).

Breaking waves are coherent in video records across the entire surf zone due to the clean long-crested, narrow-band swell. In the outer surf zone, where wave amplitudes fluctuate on scales of wave groups, coherence between video and fixed *in situ* instruments at incident frequencies is reduced since not as many waves are breaking. Low frequency oscillations in video records are incoherent with colocated pressure and velocity measurements. Lack of coherence offshore suggests that any direct low frequency break point forced waves are not as strong as the resonant free modes clearly observed by the fixed instruments. Comparisons with inshore (trough) velocities, pressure, and shoreline runup are also uncoupled with group modulations at low frequencies.

These results are derived from cross-spectral analysis in which coherence is an integrated measure of the frequency coupling between the group time scales and infragravity response, without consideration of spatial scales of the forcing. Since the forcing spectra are broad banded across wavenumber-frequency space, observed coupling can be substantially reduced, an observation seen previously in other field data (Huntley and Kim, 1984; Guza, *et al.*, 1984). In fact, as Bowen and Guza (1978) point out, resonant response requires at least some of the spatial scales in the forcing to match the cross-shore structure of infragravity waves. Thus the low coherence observed can be a consequence of the high Q (resonance) of the system, in which free waves dominate the forced response. A further complication is the potential for substantial topographic influence on the infragravity flow field (Kirby, *et al.*, 1981; Symonds and Bowen, 1984).

Finally, we observe the group structure in the wave field to be greatly reduced by breaking in the inner surf zone. All initiation of breaking occurs seaward of the crest, with generally larger waves breaking further offshore and a higher percentage of breaking waves in progressively shallower depths. This suggests that surf zone forcing models which assume a depth dependence on breaking amplitude are more in keeping with the data (*e.g.*, Symonds, *et al.*, 1982). Furthermore, breaking does not cease at the point of minimum depth at the crest, and in fact breaking is widespread in the trough of the bar. This suggests that lateral mixing of momentum across the surf zone, due to the time-lagged dissipation of incident wave energy (*e.g.*, Roelvink and Stive, 1989), could be an important mechanism for modeling longshore currents.

ACKNOWLEDGMENTS

This work was supported by the Office of Naval Research, Coastal Sciences program under grant number N00014-90-J1118. Additional funding for DELILAH was provided by CERC. Chuck Long computed the frequency-direction spectra. The frequency-wavenumber spectra were generated by software developed by Steve Pawka and Joan Oltman-Shay. Runup data were digitized by Christine Valentine. Ed Thornton and Bob Guza provided the surf zone instrumentation for DELILAH. Appreciation is given to the hard working staff of the FRF who provided unparalleled support during the experiment. We wish to thank in particular Bill Birkemeier, Kent Hathaway, Todd Walton, and Todd Holland for aiding in the collection of the video data. The late Paul O'Neill was chief engineer for the OSU group, and without his efforts this work would not have been possible. Over the past few years, Paul was instrumental in the development of all aspects of our video techniques and image analysis. He was a contemporary scientist, creative engineer, and a good friend.

CHAPTER 5

Episodic, Nonstationary Behavior of a Double Bar System at Duck, N.C., U.S.A., 1986-1991

ABSTRACT

The general behavior of the nearshore sand bar system (consisting of 1-2 longshore bars) at the U.S. Army Corps of Engineers Field Research Facility at Duck, N.C., U.S.A., is investigated over a 5 year period. The position of a very dynamic inner bar was sampled on a nearly daily basis using the video methods of Lippmann and Holman (1989a), and on yearly time scales was spatially homogeneous alongshore (over a 400 m length of beach). Monthly statistics of inner bar position suggest that the bar system was temporally nonstationary over the 5 year study period. The presence and location of a second outer bar was estimated from biweekly beach surveys and inferred qualitatively from images of wave breaking patterns. The importance of the existence of this subtle (in terms of bar amplitude) outer bar, is assessed in terms of the response of the overall bar system to the incident wave climate. Episodic transitions between 1 and 2 bar configuration occurs when the timing of extreme wave events (defined as offshore significant wave height exceeding 3 m for more than 6 hours) coincides with a reduced or non-existent outer bar. The influence of extreme storms depends heavily on the offshore profile characteristics and usually results in both immediate alterations to the beach profile and subsequent monthly averaged bar migration patterns. The most dramatic change to the bar system resulted from the succession of two very extreme storms within a 10 day period, at which time a single (only) prominent bar migrated offshore and shortly thereafter became the outer bar as a new bar formed off the beach face. In the previous analysis of Birkemeier (1984), biweekly beach profile data sampled at this same beach (from 1981-1984) shows similar bar crest behavior, and suggests that the transition from 1 to 2 bar configuration at the Duck field site is a natural progression.

INTRODUCTION

Nearshore sand bars are major features of nearly every beach found in nature. They can be very dynamic, particularly during high energy surf zone conditions. Bars may also contain a large volume of sand, thus playing an important role in the overall nearshore sediment budget. They may also provide a natural barrier to direct incident wave attack by dissipating incident wave energy seaward of the beach face. The importance of these ubiquitous topographical features has been acknowledged in the literature for quite some time, yet there is relatively little quantifiable data available to address details of bar behavior over time scales on the order of a few years.

Previous work has focused either on bar genesis, attempting to model bar formation and evolution in terms of equilibrium beach profile conditions (Bowen, 1980; Dally and Dean, 1984; Sallenger, *et al.*, 1985), or on sequential beach states in which the transition between beach morphology is dependent on the previous configuration (Greenwood and Davidson-Arnott, 1979; Short, 1979; Wright and Short, 1984; Goldsmith, *et al.*, 1982; Sunamura, 1988, Lippmann and Holman, 1990). The leading equilibrium models, based on either incident or infragravity wave forcing, are somewhat competing in that their dependence of bar scaling on beach slope is opposite. These models are discussed in terms of field data from a naturally barred beach in Duck, North Carolina, in the companion paper by Holman and Sallenger (1992).

The sequential models have primarily concentrated on the morphologic behavior of a single bar system or the inner most bar of a multiple barred beach, without regard to the potential influence of other offshore perturbations (a notable exception being Goldsmith, *et al.*, 1982, who also considered a persistent and crescentic outer bar system). Distinctions between different morphologic states are predominantly with regard to longshore variability (*i.e.*, linear, crescentic, etc.) and cross-shore bar position (scaling).

Lippmann and Holman (1990; hereinafter referred to as LH90) analyzed a set of daily time exposure images spanning a two year period from Duck. Quantitative analysis using image processing techniques suggested that the dynamic inner bar (of a two bar system) may behave in both an equilibrium and sequential manner. Results show that when incident wave energy is increasing or is maintained at storm conditions, bar morphology responds in an equilibrium manner with incident wave conditions. As incident wave energy decreases or is maintained at low energy conditions, the bar behaves more in a predictable, sequential manner. However, consideration was based solely on the behavior of the first, inner bar, without regard to a second, more offshore outer bar. In addition, the potential for interannual variability could not be addressed, a limitation of only two years of morphologic data.

This paper has two main objectives. The first is to address the influence of a possible outer bar on the behavior of an inner bar. The LH90 data set is extended to five years, with the analysis focusing on the monthly mean cross-shore position of both the prominent inner bar and the more subtle offshore bar. Daily changes in bar position and shape will not be addressed (as in LH90), but rather the general behavior of the mean (monthly averaged over the array) bar position and integrated variability is investigated. Analysis is focussed on bar behavior with regard to temporal stationarity and the presence or absence of the outer bar. The second objective is to determine the response of the bar system to the timing of episodic extreme wave events (defined later) with the existence and amplitude of an outer bar.

The next section describes our field methods and ancillary data used in the study. Our methods for sampling inner bar positions from video recordings of the surf zone and outer bar positions from survey data are then described. Results are presented in the following section, describing the incident wave climate during the 5 year study period, our observations of sand bar positions, and the episodic response of the bar system to extreme wave events. The results are then discussed and summarized.

FIELD METHODS AND DATA COLLECTION

The data were collected from 1 October 1986 through 15 September 1991, at the Army Corps of Engineers Field Research Facility (FRF) located on the Outer Banks of North Carolina, near the town of Duck (Figure V.1a; Birkemeier, *et al.*, 1985). A map of the study area showing the location of the camera in relation to the FRF pier is shown in Figure V.1b. The study area ranges from dune crest to ~450 m offshore, and begins ~180 m north of the FRF pier and extends northward 660 m alongshore.

Previous data has indicated that the beach at Duck is characterized by a persistent, very dynamic inner bar, approximately 30-120 m offshore, and a secondary, lower amplitude bar approximately 300-400 m offshore. The beach foreshore is predominantly steep, $\tan\beta \approx 0.08$ (1:12.5), and the shoreline is very stable, consisting of a mixture of medium quartz sand (mean grain size ≈ 1 mm) and carbonate shell debris (of up to 20%). Offshore, the bottom slope approaches $\tan\beta \approx 0.0061$ (1:164) near the 8 m depth contour, and the median grain size decreases to ~0.1 mm. A more complete description of the beach conditions is contained in Birkemeier, *et al.* (1989).

Video data were collected using a black-and-white television camera mounted on top of a 40 m high tower erected on the dune crest (~44 m above NGVD) 63 m north of the FRF pier (Figure V.1b). This superb vantage point allows both quantitative coverage of a large section of beach (~700 m alongshore) yielding a good representation of surf zone conditions and bar morphology, and a qualitative assessment of the general morphologic characteristics of the bar system well north (several kilometers) of the immediate field site. Video records of 40 minute length were acquired on a nearly daily basis at approximately the same time each day. Time exposures of ten minute duration are created digitally from video tapes of surf zone wave breaking using an image processing system (described in Lippmann and Holman, 1989a; hereinafter LH89). Shoreline and bar positions are determined from conventional and differencing time exposures, respectively.

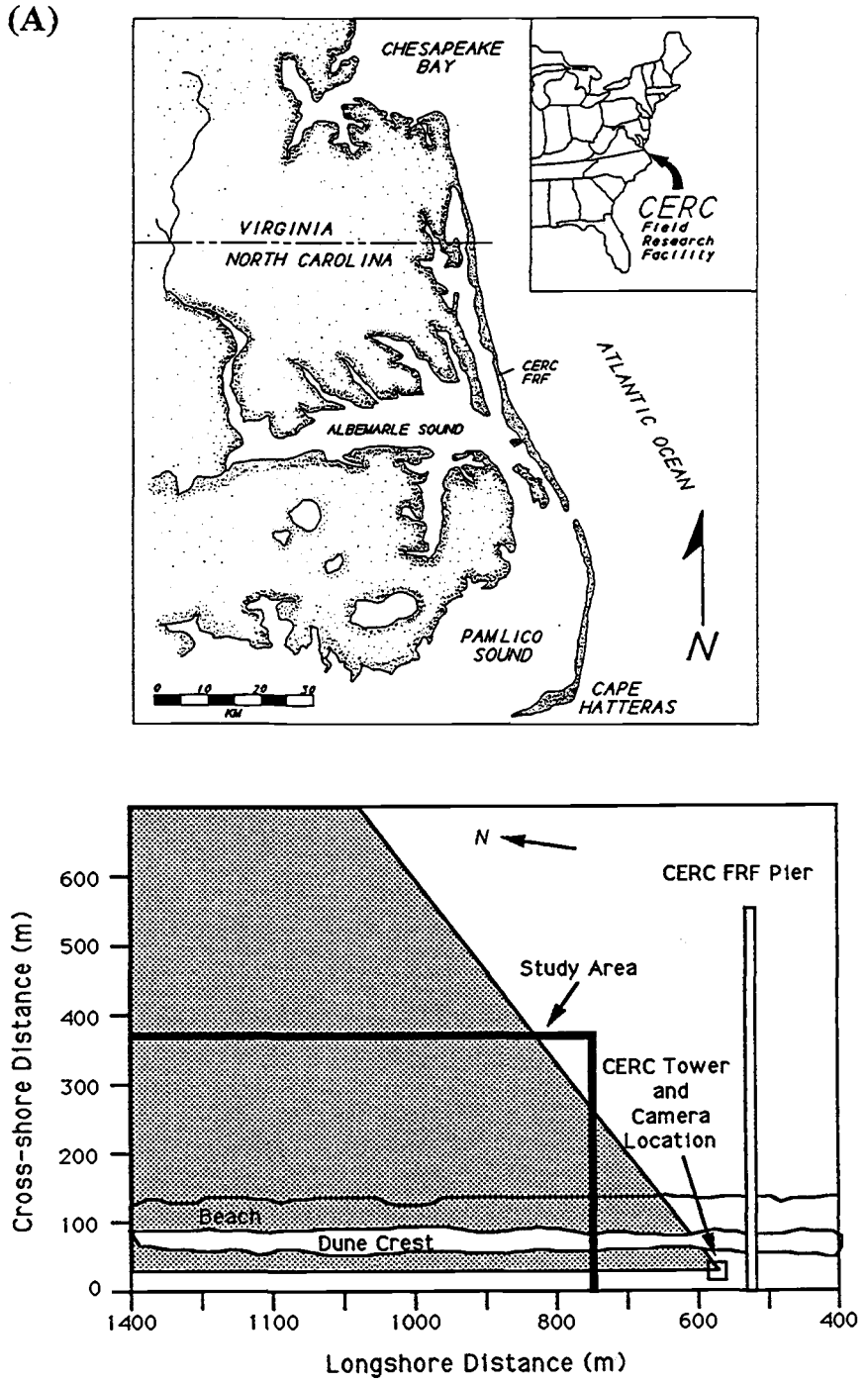

Figure V.1. (A) Geographic location of the FRF field site on the North Carolina coast of the eastern U.S. (B) Map of the field site for the 5 year study. The position of the camera in relation to the FRF pier and the study area is indicated. Longshore and cross-shore distances are relative to the FRF coordinate system. The stippled area indicates the maximum ground coverage in the field of view of the camera.

(Differencing time exposures are generated by subtracting a video frame from the previous frame, and then summing the resulting difference images.) These sampling methods are described more thoroughly in the next section.

Additional data used in this study include beach surveys conducted by the FRF staff as part of their ongoing sampling program. Complete bathymetric surveys of the FRF field site were completed on approximately monthly intervals, while selected profiles were sampled every two weeks at cross-shore transects located 1005 and 1096 m alongshore in the FRF coordinate system (Figure V.1b). Profile data were surveyed with the Coastal Research Amphibious Buggy (CRAB; Birkemeier and Mason, 1984) using a Zeiss total station or a Geodometer automatic tracking system, and will be referred to throughout the paper as CRAB surveys. Vertical elevations in the beach survey plots presented are relative to NGVD, with the mean water level over the 5 year period at +0.17 m. Ancillary wave measurements were obtained from a Waverider buoy located ~6 km offshore. Deep water wave statistics of significant wave height, H_s, and peak incident wave period, T_p, were determined from 20-minute records sampled at 6 hour intervals. Missing wave data were augmented with a wave staff located at the end of the FRF pier (~0.5 km offshore). Tide data were also recorded with a NOAA tide gage at the end of the pier, and were utilized in the determination of geometrical transformation parameters (LH89). The average daily tidal range over the length of the study period was approximately +/- 1 m, with a maximum annual range of +/- 1.25 m.

In the following analysis we define inner and outer bars subjectively in the following manner. Inner bars are defined as having the most pronounced trough-crest (relief) amplitude. Outer bars exist seaward of the most prominent inner bar, and are defined as a perturbation in an otherwise featureless offshore profile. However in the case of a low-tide terrace bar at the shoreline it is not clear that this bar will be the most prominent feature, although it is clearly an inner bar. Therefore in cases when this bar type exists, other bars along the profile are determined to be either inner or outer by

comparing with previously defined inner and outer bars. The determination of bar type is based on available CRAB surveys, as well as inferred from patterns of wave breaking distributions.

METHODS OF SAMPLING BAR POSITIONS

Sampling methods are described in detail in LH89 and LH90, and thus are only summarized here. Images are stored in a 512 x 480 pixel (picture element) array. Each pixel represents the average luminance of the sea surface over the corresponding ground area, and ranges in gray shades from 0 (black) to 255 (white). Time averages of surf zone wave breaking produces intensity patterns that provide an excellent proxy for bar position and shape (provided waves are large enough to break over the shallows of the bar). An example ten minute average (time exposure) is shown in Figure V.2a. The position of the shoreline (visible due to the shore break) and the morphology and position of the inner bar system is clearly revealed.

Image locations are mapped into true ground coordinates using oblique geometrical transformation equations (LH89). Shore normal image intensity profiles are then digitized at known longshore distances. Each profile is sampled at 1 m cross-shore increments and extends from behind the dune crest to approximately 400 m offshore. Such intensity profiles are sampled along 45 cross-shore transects spaced at 15 m intervals alongshore, thus spanning a total beach length of 660 m. The array of image intensity transects sampled from the image in Figure V.2a is plotted in Figure V.2b. In the figure each transect is offset vertically, with increasing longshore distance to the north towards the top (see Figure V.1b). The approximate position of the shoreline and bar crest (shown in the profile at the bottom of the figure) corresponds well with the location of local image intensity maxima along each profile line (labeled in the figure). Note that the profile lines are much shorter closer to the camera, a result of the upper right hand corner of the array not being visible by the camera (Figure V.2a). The unaffected image array area is further reduced in overall beach length when the bar is situated further offshore. In addition, the camera orientation was altered slightly several times during the period (22 geometry

Figure V.2. (A) Example 10 minute time exposure image from 4 December 1988. The average luminance of the sea surface shows concentrations of wave breaking and foam at the shoreline and over an offshore sand bar. (B) Shore normal image intensity transects from the same day showing the position of the shoreline and offshore sand bar. The horizontal axis is cross-shore distance and relative to the FRF coordinate system. The vertical axis is non-dimensional image intensity. Successive profiles alongshore (sampled at 15 m intervals) are offset vertically, with longshore distance more northward toward the top of the figure. Also included in (B) is the beach profile from about the middle of the array ($y = 1097$ m) and the still water level (SWL), showing the surveyed bar and shoreline positions.

Figure V.2. (Continued) (A) Example 10 minute time exposure image from 4 December 1988.

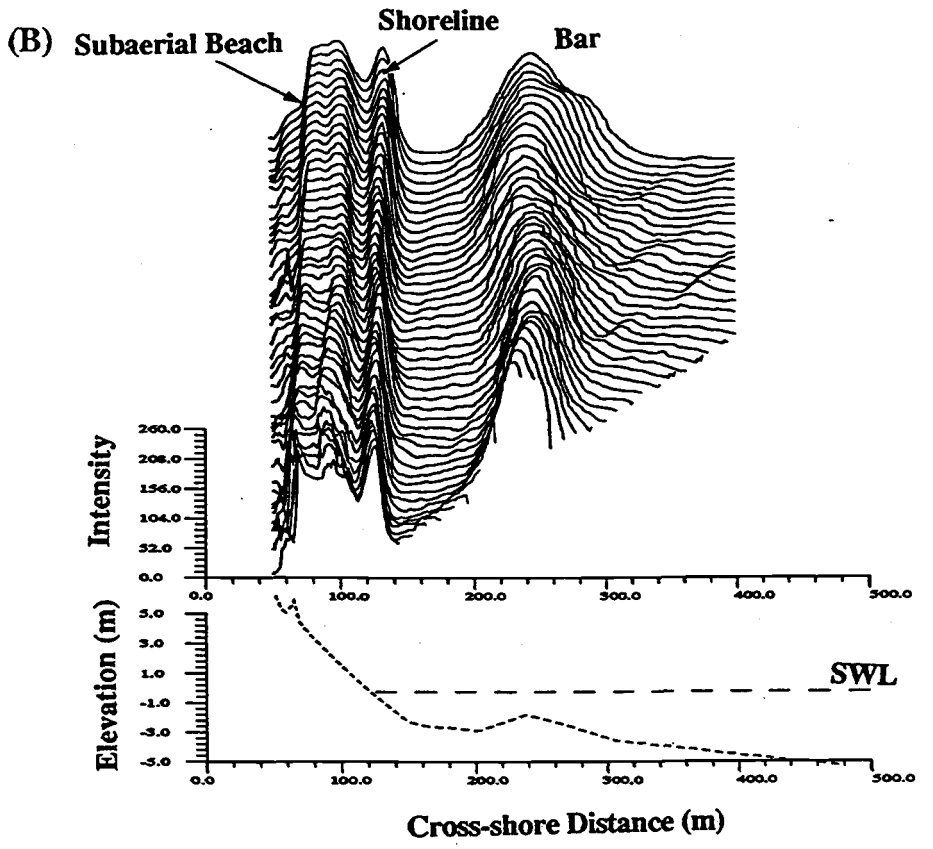

Figure V.2. (Continued) (B) Shore normal image intensity transects from the same day showing the position of the shoreline and offshore sand bar.

changes in all) occasionally reducing the longshore extent of the imaged field site. As a result, the first 260 m of the study area were eliminated from subsequent analysis, resulting in a total longshore range of 400 m.

The position of the shoreline for each sample is determined from conventional time exposure data in the following manner. First, a range along the profile is selected to search for an intensity maximum. For this data the range was set between 90 and 140 m in the FRF coordinate system. The selected data within the defined range are then linearly detrended and low-pass filtered with a 9 point (corresponding to 9 m in the cross-shore) wide Gaussian filter. The shoreline was then determined by the location of the maximum image intensity which exceeds a defined threshold level (set at 15 units above the minimum intensity). Missing values are interpolated in the manner described in LH90. The method was found to be insensitive to the values chosen for the filter width (ranging from 5-9 m) and threshold level (ranging from 5-15).

Estimates of the bar crest location were determined from differencing time exposure data in a similar manner. The minimum value to begin the search for the maximum intensity was determined as the location of the shoreline plus 20 m (low-tide terrace bars less than ~20 m offshore are usually indistinguishable from the shoreline). The maximum cross-shore search limit was set at 350 m. The data were then detrended and then low-pass filtered with a 15 pt (15 m) wide Gaussian filter. Thresholds were set at 3-15 intensity units, and were varied to account for differences in image gain and contrast during particular blocks of data (usually due to adverse weather conditions or relatively less wave breaking). The determination of the offshore maxima is much more difficult than when identifying the shoreline, and much more care was taken to be sure the digitized location was in agreement with available profile data. Data with less than 40% of the alongshore bar crest positions which pass these criteria were eliminated from the analysis. Remaining missing alongshore estimates were interpolated as in LH90.

The criteria were found to work well for most of the data. However difficulties arose for the case of a low-tide terrace feature coexisting with the presence of a second prominent inner bar. During 1989 this was observed, and it was necessary to modify the search criteria slightly. An adjustment was made to account for the 2 bars by applying different sampling criteria to identify first only the close bar (by limiting the offshore extent of the defined range), and then adjusted to choose the second bar (by starting the search further seaward and extending the offshore extent of the defined range). These criteria were then applied separately to the entire data set as a test of our abilities to track the inner bar system accurately, and are referred to as bar sampling methods denoted VM1 and VM2. CRAB survey data was used to confirm our estimates of bar position, and to distinguish shoreline estimates from low amplitude terrace features very close to shore.

Table V.1 summarizes the sampling success over the 5 year period in terms of yearly and total statistics. Summaries are given for shoreline data, as well as for both bar sampling methods. A total of ~85% of all days were sampled with the video recordings. The most notable gap was a 4 month period from 11 May - 2 September 1989 in which the data tapes were damaged. This particular gap was not as severe as might be expected since it occurred during the summer months when wave energy was reduced (described later; Figure V.6) and the bar is typically least active (LH90). Bar position data during this period was based on CRAB surveys. A total of 99% of all shoreline samples and 73% of all bar samples passed the defined sampling criteria.

Outer bar positions were determined from the CRAB surveys. Sample profiles (at longshore distances 1005 and 1097 m in the FRF coordinate system) from near the beginning and end of the study are shown in Figure V.3. The method for determining the crest location from survey data is the same as that used by Birkemeier (1984). Bar positions were visually estimated from profile plots, where the crest was chosen as the point of maximum perturbation from an otherwise featureless profile (see also Bowen and

TABLE V.1. Summary of video sampling success for estimating inner bar and shoreline positions.

Year	Total Days	Samples (%)	Estimates (days)			% Good Estimates			% Total Data		
			Shore	*Bar*[1]	*Bar*[2]	*Shore*	*Bar*[1]	*Bar*[2]	*Shore*	*Bar*[1]	*Bar*[2]
1986	92	89 (92.7)	89	86	83	100.0	96.5	93.0	92.7	93.4	90.2
1987	365	321 (87.9)	320	273	252	99.7	85.0	78.5	87.7	74.8	69.0
1988	366	360 (98.4)	356	274	253	98.9	76.1	70.3	97.3	74.8	69.1
1989	365	218 (59.7)	211	97	115	99.5	44.5	52.8	57.8	26.6	31.5
1990	365	306 (83.8)	301	210	220	98.4	68.6	71.9	82.5	57.5	60.3
1991	258	248 (96.1)	248	181	201	100.0	73.0	81.0	96.1	70.2	77.9
Total	1811	1536 (84.8)	1525	1121	1124	99.3	73.0	73.2	84.2	61.8	62.1

Percentage of good estimates and total data are found by dividing the number of estimates by the number of samples and the number of total days, respectively.

[1]Video sampling method 1 (VM1)
[2]Video sampling method 2 (VM2)

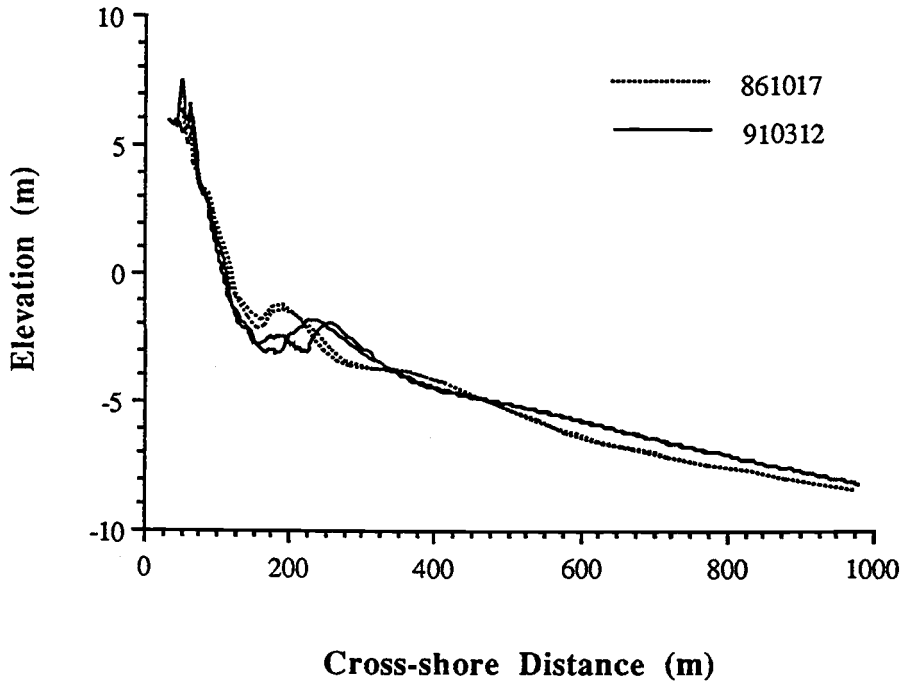

Figure V.3. Example CRAB surveyed beach profiles near the beginning of the study period (dashed line), 17 October 1986, and near the end of the study period (solid line), 12 April 1991. Profiles were sampled from longshore distances 1005 and 1097 m in the FRF coordinate system (Figure V.1). The most notable features are the well defined outer bar in the beginning of the study, and the absence of any offshore feature near the end, as well as significant accretion of sediment in water depths greater than 4 m.

Huntley, 1984). Using this method often resulted in choosing the bar as a slope break in the profile rather than a well defined trough-bar sequence. Qualitative observations of wave breaking offshore (from the videos) during high waves were used to confirm the presence or absence of an outer bar. To illustrate these observational interpretations, two example 10 minute time exposure images generated during similar wave conditions ($H_s \approx$ 2.8 m; $T_p \approx 8$ sec) but having distinctly different offshore characteristics are shown in Figure V.4a (11 October 1986) and 4b (21 April 1991). The time exposure during October 1986 clearly shows the presence of an offshore sand bar, whereas the April 1991 time exposure does not show any breaking offshore, inferring that the outer bar is much deeper than in 1986 or is absent.

Since the outer bar is often rather subtle, it is worth noting that the appropriate measure of a sand bar location is not necessarily the point of minimum depth. Holman and Bowen (1982) treat the sand bar as a perturbation to an otherwise featureless profile, and thus the point of maximum perturbation will always be seaward of the point of minimum depth. This approach has been adopted here. Holman and Bowen also point out that a low-tide terrace can be thought of as a small-amplitude bar, consistent with the definitions of bar types used in LH90 and in this study.

The change in offshore wave breaking patterns in the two examples (Figure V.4) suggests that substantial changes to the beach system occurred during the study period. CRAB surveys from at about the same time on 17 October 1986 and 12 July 1991 (Figure V.3) reveal a two bar system with a well defined outer bar early in the study period, and a one bar system with an essentially featureless offshore profile at the end. The profiles also indicate appreciable sediment deposition in depths greater than 4 m, and a much flatter offshore profile (see also Howd and Birkemeier, in review).

(A)

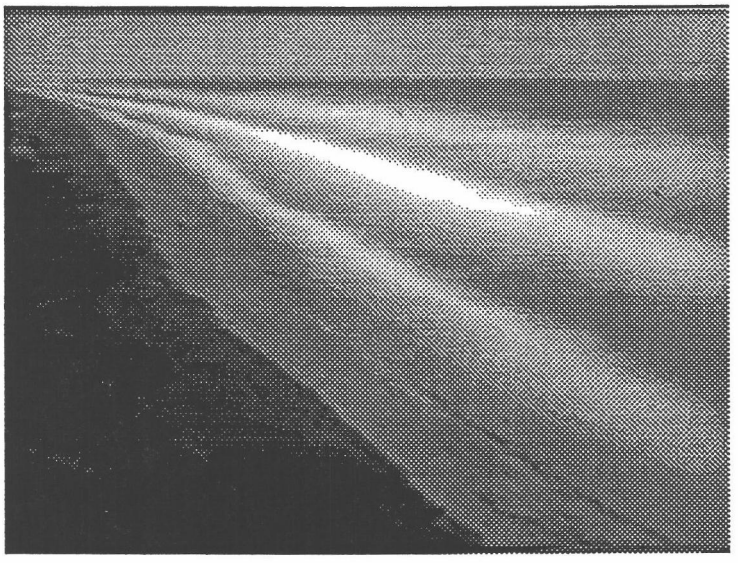

(B)

Figure V.4. Example 10 minute time exposure images from storms (A) near the beginning of the study period, 11 Oct. 1986, and (B) near the end of the study period, 21 April 1991. Average intensity patterns in (A) indicate the presence of an inner bar as well as a second outer bar further offshore, whereas intensity patterns in (B) indicate the presence of only one bar. Note that wave conditions for each storm are similar (Table V.2).

RESULTS

Incident Wave Conditions

Monthly averages of T_p, H_s, and wave power, $P = \frac{1}{8}\rho g H_s^2 Cn$, where ρ is the density of water, g is gravity, and Cn is the group velocity) are calculated for all months during the 5 year study period. Seasonal trends in the general wave climate are clearly shown in the histograms of monthly means and standard deviations (Figure V.5). H_s and P are characterized by higher energy during late fall, winter, and early spring, whereas the average monthly T_p show no mean monthly variations. The time series of monthly averages and standard deviations is shown in Figure V.6. The H_s and P time series both show the seasonal cycle in incident wave energy, with summer months being typically much less energetic than at other times, and substantial interannual variability due to the occurrence of random storms. Large wave events, defined as storms having a maximum H_s greater than 2.0 m, are detailed in CERC's FRF monthly *Preliminary Data Summary's*, and are summarized in Table V.2. Maximum H_s, corresponding T_p, and the duration of the storm (in hours) for which H_s exceeds 2 m are listed. In general, the wave climate along the North Carolina Coast is variable throughout the year, with higher wave conditions dominated by short duration extratropical northeasters (most commonly lasting less than 24 hours), and occasional tropical hurricanes during the late summer and fall.

The dominant features in the time series are the occasional energetic months, usually in late fall and winter (Figure V.6) that are associated with the occurrence of extreme wave events. Extreme wave events are defined as when H_s exceeds 3 m for an extended period of time (greater than 6 hours). Comments in Table V.2 list the duration of the extreme storm waves and the smallest H_s above 3 m recorded (every 6 hours) during the storm. The occurrence of special events (hurricanes) are also indicated. During the 5 year study

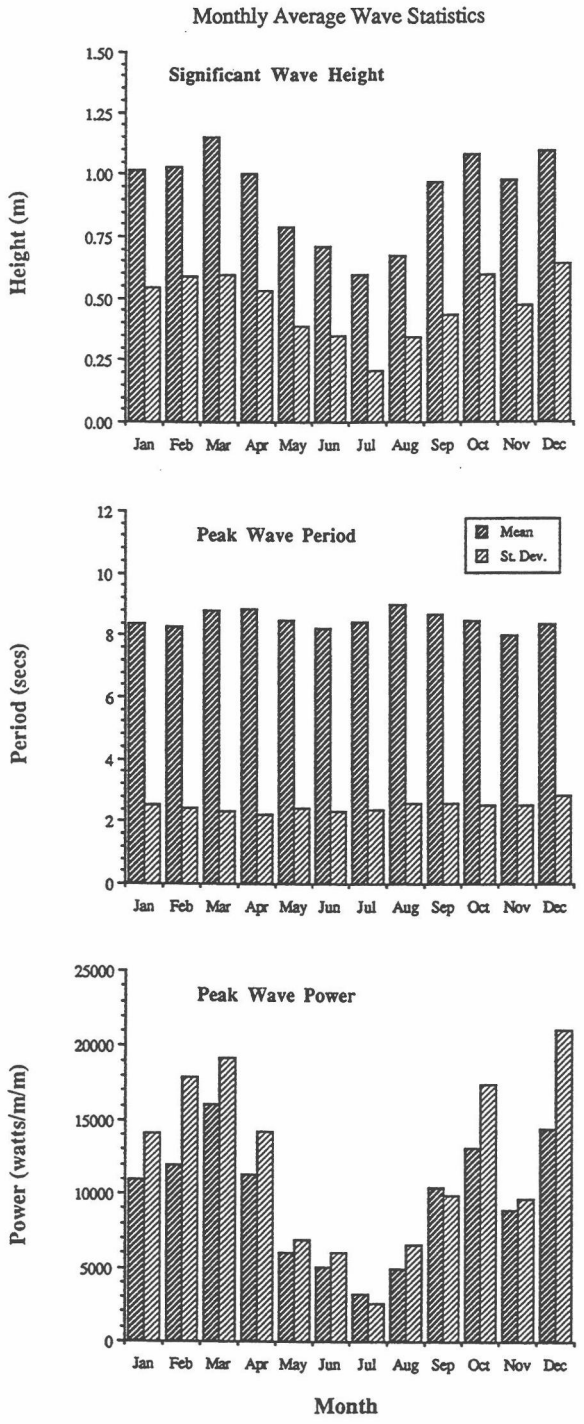

Figure V.5. Histograms of monthly averaged mean and standard deviation offshore incident wave statistics for significant wave height (upper panel), peak wave period (middle panel), and peak linear wave power (lower panel). Although wave period shows no significant monthly differences, wave height and power have characteristic seasonal variations.

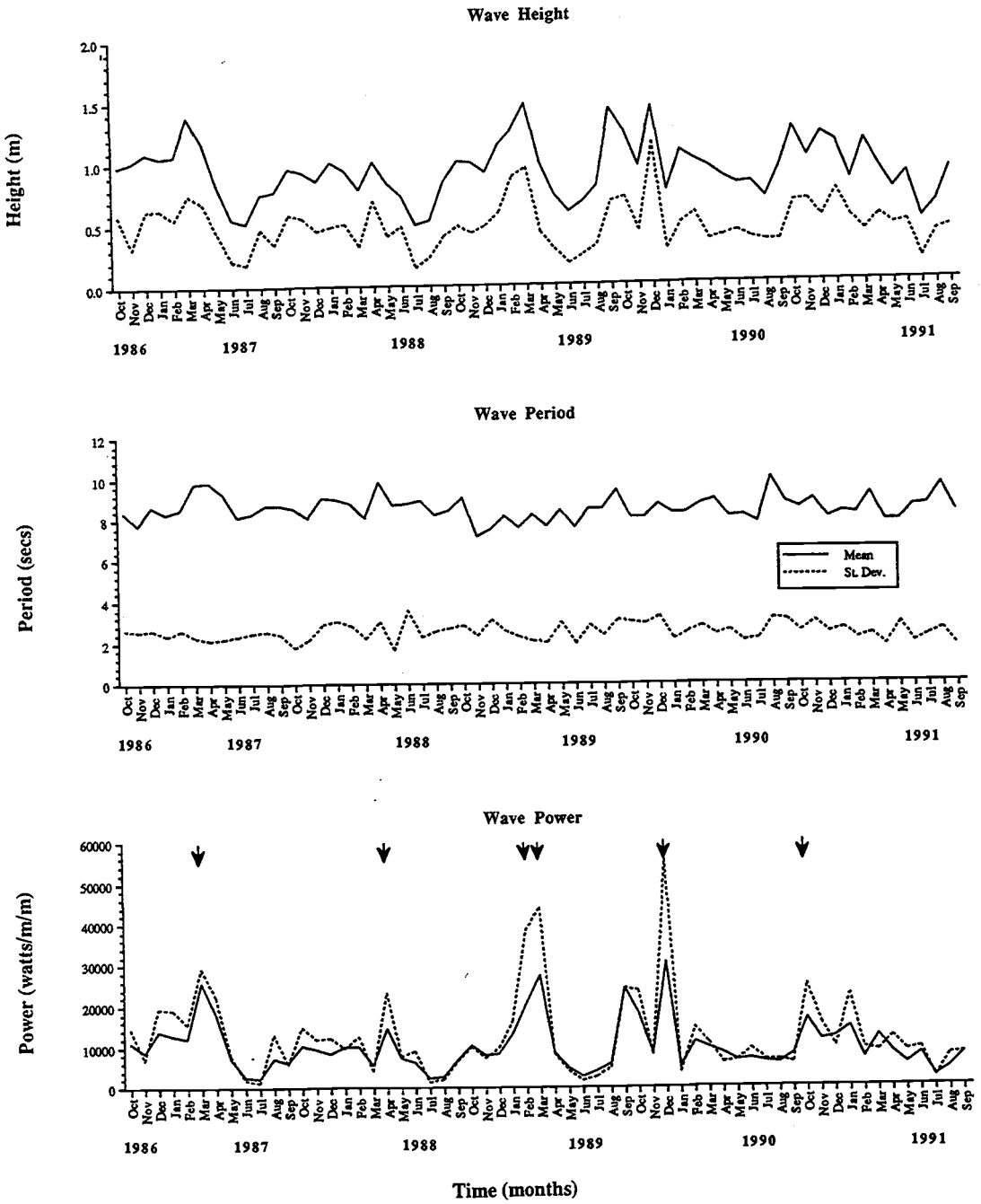

Figure V.6. Time series of average monthly wave statistics for offshore significant wave height (upper panel), peak wave period (middle panel), and peak linear wave power (lower panel). The horizontal axis is time in months. The occurrence of extreme wave events (summarized in Table V.2) are indicated by arrows in the wave power figure.

TABLE 2. Storms during the study period when H_s exceeds 2.0 m.

Year	Month	Days	Max H_s (m)	T_p (secs)	Duration (hrs)	Other
1986	Oct	10-12	2.86	7.24	60	
		19	2.15	11.98	24	
	Nov	14	2.01	6.74	6	
	Dec	01-03	3.13	9.75	48	
		24	2.53	8.83	6	
1987	Jan	01-02	3.47	10.24	18	
		17	2.08	7.32	18	
		22	2.00	7.32	3	
		26-27	2.62	11.14	42	
	Feb	16-18	3.42	8.83	36	
	Mar	10-16	3.36	9.48	146	> 3.0 m H_s for 28 hrs
		23-24	2.93	12.20	28	
		30-31	2.09	10.24	18	
	Apr	25-28	3.14	11.14	84	
	May	04-05	2.26	6.92	12	
	Jun	None				
	Jul	None				
	Aug	14-15	2.60	11.14	30	
	Sep	04-05	2.06	7.11	5	
	Oct	12	2.07	6.74	6	
		13-15	2.78	8.26	60	
	Nov	11-12	2.39	10.67	12	
		27	2.16	7.53	9	
		29	2.30	10.24	10	
	Dec	29-30	2.65	11.64	24	
1988	Jan	08	2.66	7.76	12	
		14	2.49	7.11	12	
	Feb	12	2.25	9.14	7	
		28-29	2.76	8.00	24	
	Mar	11	2.20	6.90	3	
	Apr	08-09	2.80	9.85	30	
		12-14	4.96	10.24	52	> 3.1 m H_s for 18 hrs
		19	2.17	6.92	3	
	May	None				
	Jun	03-04	2.40	7.53	32	
	Jul	None				
	Aug	None				
	Sep	None				
	Oct	04	2.29	6.56	12	
		08	2.07	6.92	6	
	Nov	01	2.41	6.92	4	
		24	2.47	7.30	15	
	Dec	04	2.29	7.31	4	
		15-16	2.34	14.22	26	
1989	Jan	04	2.24	7.11	6	
		23-24	3.08	10.67	36	
	Feb	17-19	2.86	7.53	49	
		23-25	4.09	11.13	52	> 3.3 m H_s for 36 hrs
	Mar	03	2.43	8.53	12	
		07-11	4.22	12.18	108	> 3.7 m H_s for 60 hrs
		23-24	2.44	8.53	32	

TABLE V.5. Continued.

Year	Month	Days	Max H_S (m)	T_p (secs)	Duration (hrs)	Other
	Apr	11	2.08	6.74	12	
	May	None				
	Jun	None				
	Jul	None				
	Aug	None				
	Sep	03-05	2.58	8.26	42	
		06-08	2.44	14.22	60	(Hurricane Gabrielle)
		21-22	2.50	15.06	20	(Hurricane Hugo)
		23-24	2.50	7.53	12	
		27	2.39	7.76	9	
	Oct	25-26	2.60	12.19	36	
	Nov	23	2.32	7.31	9	
	Dec	08-10	3.05	9.85	54	
		13	2.46	9.48	13	
		22	2.31	6.74	10	
		23-25	5.63	11.13	58	> 4.4 m H_S for 24 hrs
1990	Jan	None				
	Feb	05	2.07	7.31	6	
	Mar	06-07	2.50	7.53	16	
		29	2.22	6.92	5	
	Apr	07	2.00	5.69	3	
		18	2.20	6.92	12	
	May	22-23	2.33	6.92	13	
	Jun	12	2.12	6.24	6	
	Jul	None				
	Aug	None				
	Sep	None				
	Oct	12-13	2.44	12.88	19	(Hurricane Lily)
		25-27	5.00	9.85	38	> 3.7 m H_S for 18 hrs
	Nov	10	2.62	9.85	6	
		17-19	2.37	7.76	42	
		30	2.15	6.92	2	
	Dec	08-09	2.08	9.48	15	
1991	Jan	07-09	2.96	10.67	25	
		11-12	2.25	8.83	6	
	Feb	23	2.30	7.53	17	
	Mar	06-07	2.50	7.53	16	
		29	2.22	6.92	5	
	Apr	20-21	2.81	8.83	19	
	May	18-19	2.43	6.92	24	
	Jun	23	2.43	8.26	7	
	Jul	None				
	Aug	18-19	4.83	15.06	8	(Hurricane Bob)
		25	2.19	6.40	5	
	Sep	01-02	2.47	8.00	17	
		20	2.28	7.11	12	

Statistics are from CERC's FRF monthly Preliminary Data Summaries. Extreme storm duration is indicated under the "other" category by the total number of hours H_S exceeds the minimum H_S above 3.0 m. The occurrence of 4 hurricanes are also indicated.

period, a total of 6 extreme wave events were identified. Each is indicated with an arrow on the wave power time series (Figure V.6). As will be shown, important changes (with respect to overall beach response) to the FRF field site often occurred during these storms (also see Howd and Birkemeier, in review). Although the passage of 4 hurricanes during the study period caused extensive damage along portions of the eastern U.S. coastline, they had little impact at the FRF field site. The hurricanes were sometimes very intense, but as a result of not passing directly over the FRF or having a short duration (*i.e.*, Hurricane Bob in August 1991), they were not considered extreme events.

Alongshore Homogeneity

The 5 year data set of bar and shoreline position were first divided into calendar years and tested for longshore homogeneity. The yearly mean and standard deviations at each longshore location for both the shoreline and inner bar crest positions are shown in Figure V.7. Bar statistics are shown for only one sampling method (VM1), since both sampling methods yielded similar results, except for 1989 in which estimates from each method are shown. Mean shoreline positions are given in the FRF coordinate system, whereas mean bar position estimates are for distances offshore relative to the shoreline. The trends in mean shoreline position are simply the result of orientation of the FRF coordinate system with respect to the trend of the beach. This trend is removed from bar position estimates since distances are computed relative to the shoreline mean.

The bar means and standard deviations from each year are approximately linear and parallel to shore, indicating longshore homogeneity over the length of the array (400 m). However, inter-annual variability is clearly evident, particularly during 1989 as both the means and standard deviations alongshore were significantly different. The 1989 data reveal the presence of two inner bars, one much closer to the shoreline and the other anomalously further offshore. The mean shoreline position is also displaced seaward

Figure V.7. Means (left panels) and standard deviations (right panels) for estimated shoreline (lower panels) and bar (upper panels) positions for each calendar year. Estimates are from video derived data only. Two estimates are shown for 1989 bar positions, one for each bar sampling method (VM1 and VM2, described in the text). Longshore distance and mean shoreline positions are relative to the FRF coordinate system, whereas mean bar positions are relative to the shoreline. Longshore bar statistics are approximately straight and parallel to the shoreline, indicating that the data is reasonably homogeneous over the 400 m array length, although substantial interannual variability is evident.

Yearly Alongshore Averages

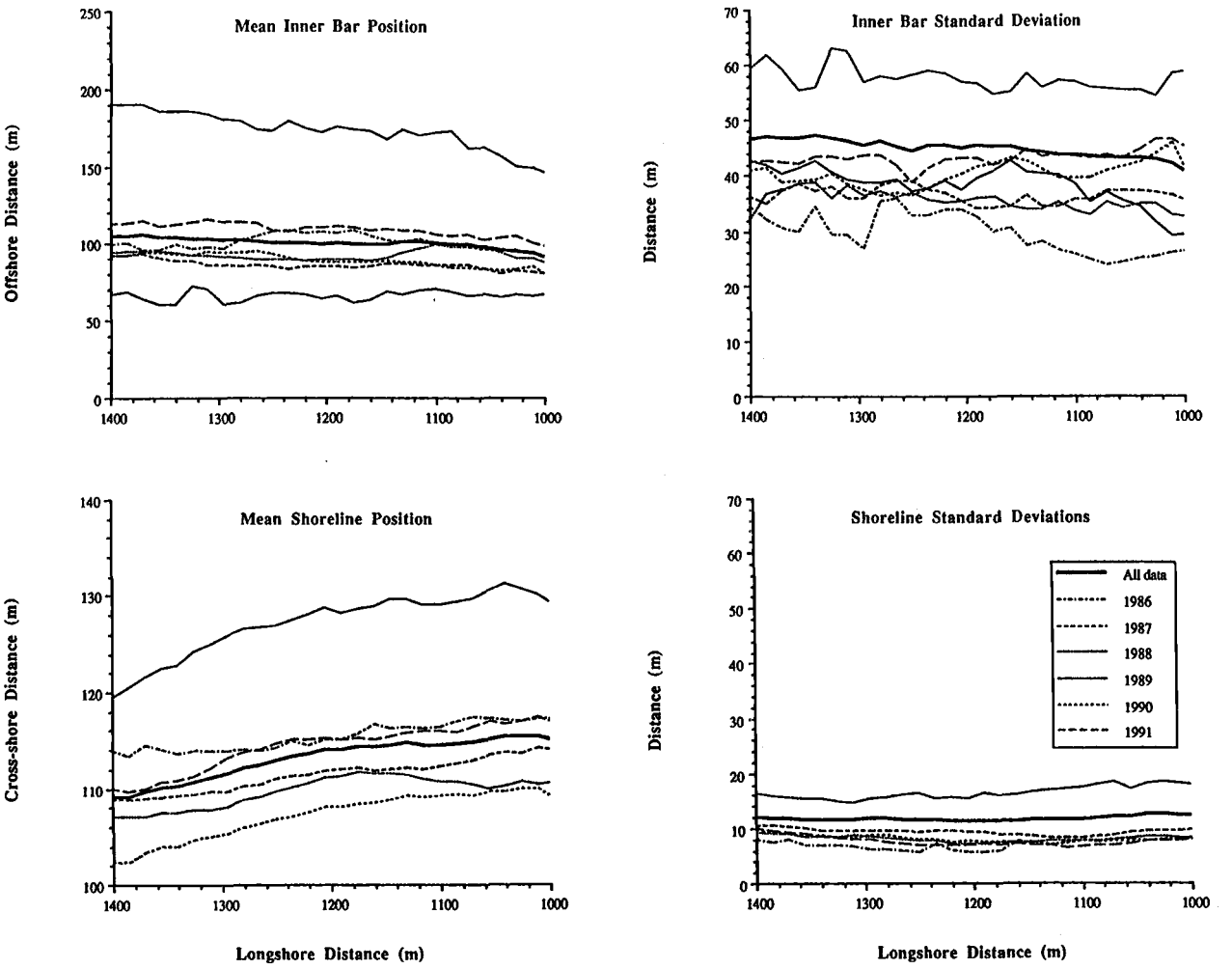

~15-20 m. The episodic, non-stationary behavior suggested by the substantial interannual variability is investigated more closely by examining the behavior of the bar system on a shorter time scale.

Temporal Stationarity

Means and standard deviations for both bar and shoreline estimates are spatially averaged over the length of the array and temporally averaged for each calendar month (Figure V.8). The 4 month gap in the video record in 1989 is supplemented with available CRAB surveys (no standard deviations are plotted for these data due to the small number of available profiles). Outer bar positions throughout the study are estimated from CRAB surveys. For comparison the P time series is shown in the lower panel (recreated from Figure V.6), and the occurrence of extreme wave events are again shown with arrows in each panel.

The mean monthly bar position is shown in the upper panel of Figure V.8. Both video bar sampling methods (VM1 and VM2) are plotted for comparison. Each sampling method tracks the same inner bar for the first two years, follows two separate inner bars from March-December 1989, and again identifies the same bar during 1990-91. The divergence in 1989 is due to an offshore migration of the prominent first bar and the generation of a new terrace-like bar near the beach face. An outer bar is observed for the first 17 months of the record, and then becomes indistinguishable in CRAB surveys and is qualitatively not observed in the videos (from a lack of offshore wave breaking patterns). The outer bar is again defined in January 1990, essentially the continuation of a previously defined prominent inner bar. The distinction between inner and outer bars is made by utilizing available CRAB surveys, and determined in the manner described earlier.

Figure V.8. Time series of average monthly mean (upper panel) and standard deviations (middle panel) for bar and shoreline estimates. Data source is indicated in the legend of the top graph. The horizontal axis is time in months, and the vertical axis for the means is cross-shore distance relative to the FRF coordinate system. Lines are connected only where bars are temporally continuous. The occurrence of extreme storms is indicated by the arrows in all panels. The average monthly wave power time series (recreated from Figure V.6) is shown in the lower panel for comparison.

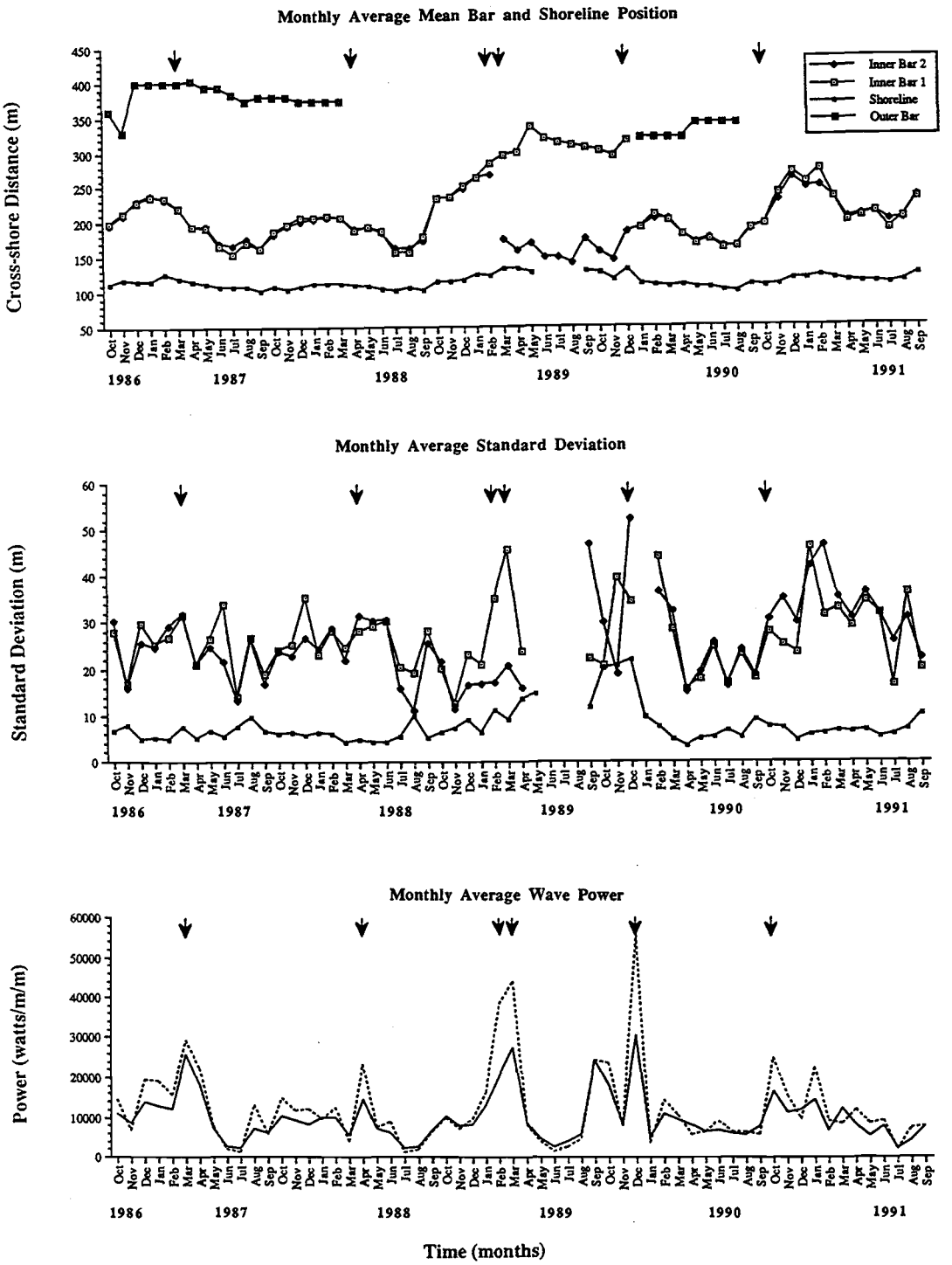
Monthly Average Mean Bar and Shoreline Position
Cross-shore Distance (m)
Inner Bar 2
Inner Bar 1
Shoreline
Outer Bar
Monthly Average Standard Deviation
Standard Deviation (m)
Monthly Average Wave Power
Power (watts/m/m)
1986
1987
1988
1989
1990
1991
Time (months)

Monthly standard deviations are shown in the middle panel of Figure V.8, and provides a means of assessing gross inner bar variability in relation to the presence or absence of an outer bar. The data clearly show an increased variability in monthly averaged standard deviations after April 1988 and again after October 1990, both times approximately coinciding with the disappearance of the outer bar. In general, inner bar variability is higher when the outer bar is absent.

The influence of the outer bar on inner bar behavior is investigated further by computing means of the monthly averages of bar position and standard deviation during periods when the outer bar exists, and then normalizing all the data in the respective time series by these monthly means. The monthly averaged mean statistics when the outer bar is present is shown in Figure V.9. The mean bar (upper panel) and shoreline positions (middle panel) clearly show a seasonal cross-shore sediment cycle. The mean standard deviations are shown in the lower panel and show no identifiable monthly or seasonal trends. It is interesting to note that the shoreline position appears to move seaward during the higher energy months (Figure V.5), indicating that the beach width actually increases on a monthly averaged basis during energetic months. Additionally there appears to be a slight phase lag of approximately one-two months in the beach width extremes and the offshore bar position extremes. This result is discussed briefly in the next section.

The monthly averaged mean and standard deviation time series (Figure V.8) were then normalized by the monthly mean statistics when the outer bar is present. The resulting normalized time series are shown in Figure V.10, along with the monthly averaged P time series (lower panel). The coincidence of the outer bar is indicated with the open bars across the top of each panel. The normalized means (upper panel) clearly show the bifurcation of the inner bars during 1989. Also evident is an apparent gradual increase in monthly mean bar position immediately following the disappearance of the outer bar. The normalized standard deviations (middle panel) also show similar behavior,

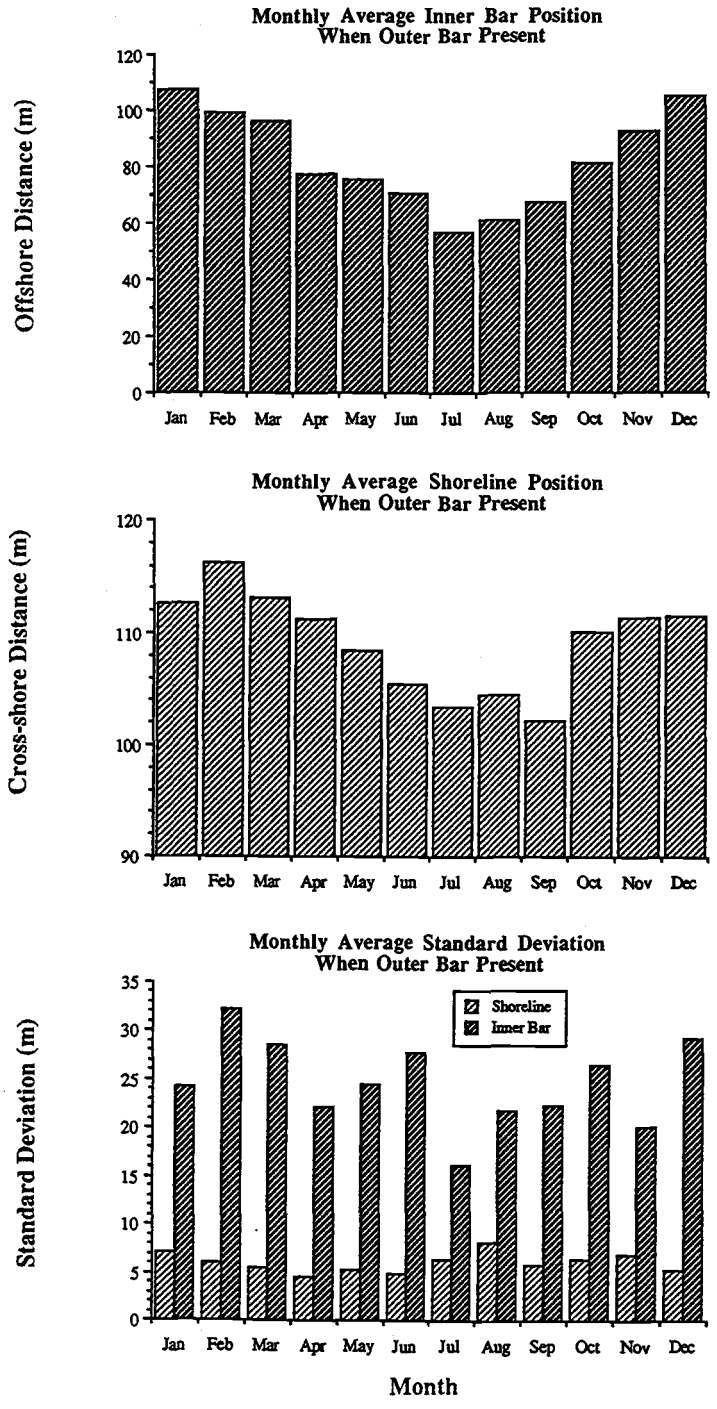

Figure V.9. Average inner bar (upper panel) and shoreline (middle panel) positions for each calendar month when an outer bar is present. Shoreline distances are relative to the FRF coordinate system, whereas bar positions are distances offshore relative to the shoreline. Average bar and shoreline standard deviations are shown in the lower panel.

Figure V.10. Time series of inner bar positions normalized by monthly averages computed when the outer bar exists (from Figure V.9). Normalized monthly inner bar position (upper panel) and standard deviations (middle panel) are plotted for each sampling method (VM1 and VM2). The open boxes along the top of each graph indicate times when the outer bar exists. The monthly average wave power time series (recreated from Figure V.6) is shown in the lower panel for comparison.

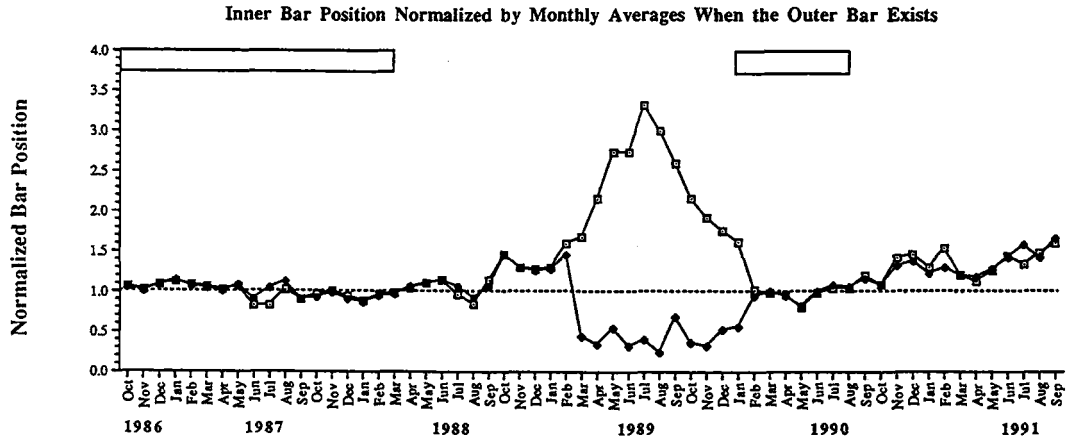
Inner Bar Position Normalized by Monthly Averages When the Outer Bar Exists
Normalized Bar Position
4.0
3.5
3.0
2.5
2.0
1.5
1.0
0.5
0.0
1986
1987
1988
1989
1990
1991

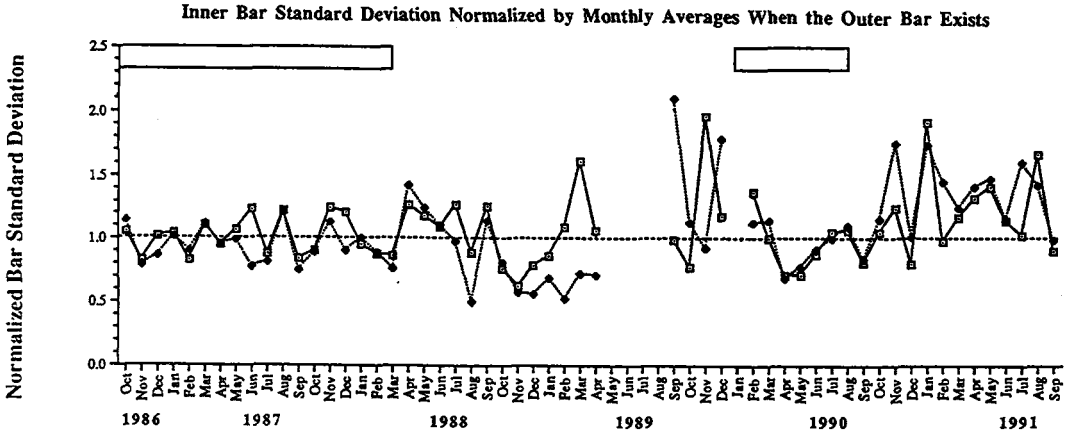
Inner Bar Standard Deviation Normalized by Monthly Averages When the Outer Bar Exists
Normalized Bar Standard Deviation
2.5
2.0
1.5
1.0
0.5
0.0
1986
1987
1988
1989
1990
1991

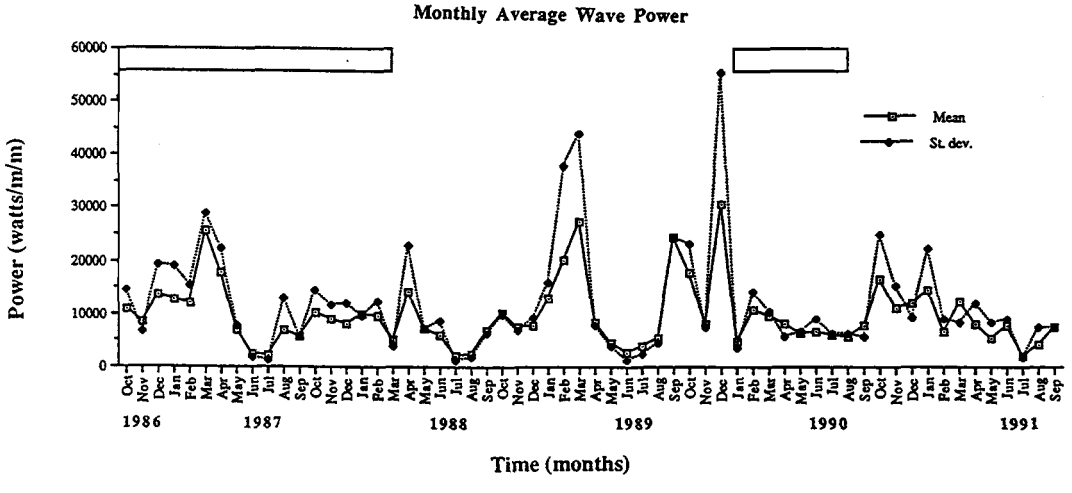
Monthly Average Wave Power
Power (watts/m/m)
60000
50000
40000
30000
20000
10000
0
Mean
St. dev.
1986
1987
1988
1989
1990
1991
Time (months)

with increased variability following the disappearance of the outer bar. Interestingly, the behavior of the inner bar immediately following the disappearance of the outer bar was remarkably similar in 1988 and 1990.

Episodic Response of the Bar System

In this section the episodic behavior observed in Figures V.8 and V.10 is addressed by focusing on specific events in which the overall character of the bar system was significantly altered. Major changes are observed primarily as transitions between one and two bar configurations. In general transitional behavior occurs under the influence of extreme storms, and depends on the initial barred configuration. Offshore profile behavior associated with individual extreme storms (Figure V.11) are presented next.

During the first extreme storm (March, 1987) daily time exposure images (which also measure alongshore morphologic variability; LH90) indicate that the inner bar surprisingly migrated onshore and was distinctly not linear. CRAB surveys from before and after the storm showed that the outer bar became more pronounced, essentially developing a better defined bar-trough sequence (Figure V.11a). (Longshore rhythmicity of the outer profile was not addressed.) The offshore slope did not noticeably change although some evidence of profile activity can be seen at depths greater than 4 m. Surprisingly, overall bar variability was not significantly modified by this intense storm lasting over 6 days (Figure V.10).

However, the next extreme storm (April 1988) significantly altered the offshore profile. CRAB surveys taken shortly after the storm show the offshore profile to be entirely smoothed, clearly showing the lack of any offshore perturbations (Figure V.11b). The absence of offshore wave breaking during these high waves confirms a relatively smooth offshore topography over the length of the study area. Following the storm the monthly mean bar position was observed to gradually migrate seaward further

Figure V.11. Beach profile response to extreme wave events observed during the study period (A) March, 1987, (B) April, 1988, (C) February-March, 1989, (E) October, 1990, and (F) the behavior of the offshore profile during the winter or 1990-1991. The data show selected profiles from longshore distances 1005 and 1096 m (when available) before (dotted lines) and after (solid lines) the storms. The dates of the surveys are labeled in each panel. In addition, three profiles associated with observed trisectional bars (Figure V.12) on 7 December 1989 are shown in (D), with the longshore locations of the surveys shown in the legend.

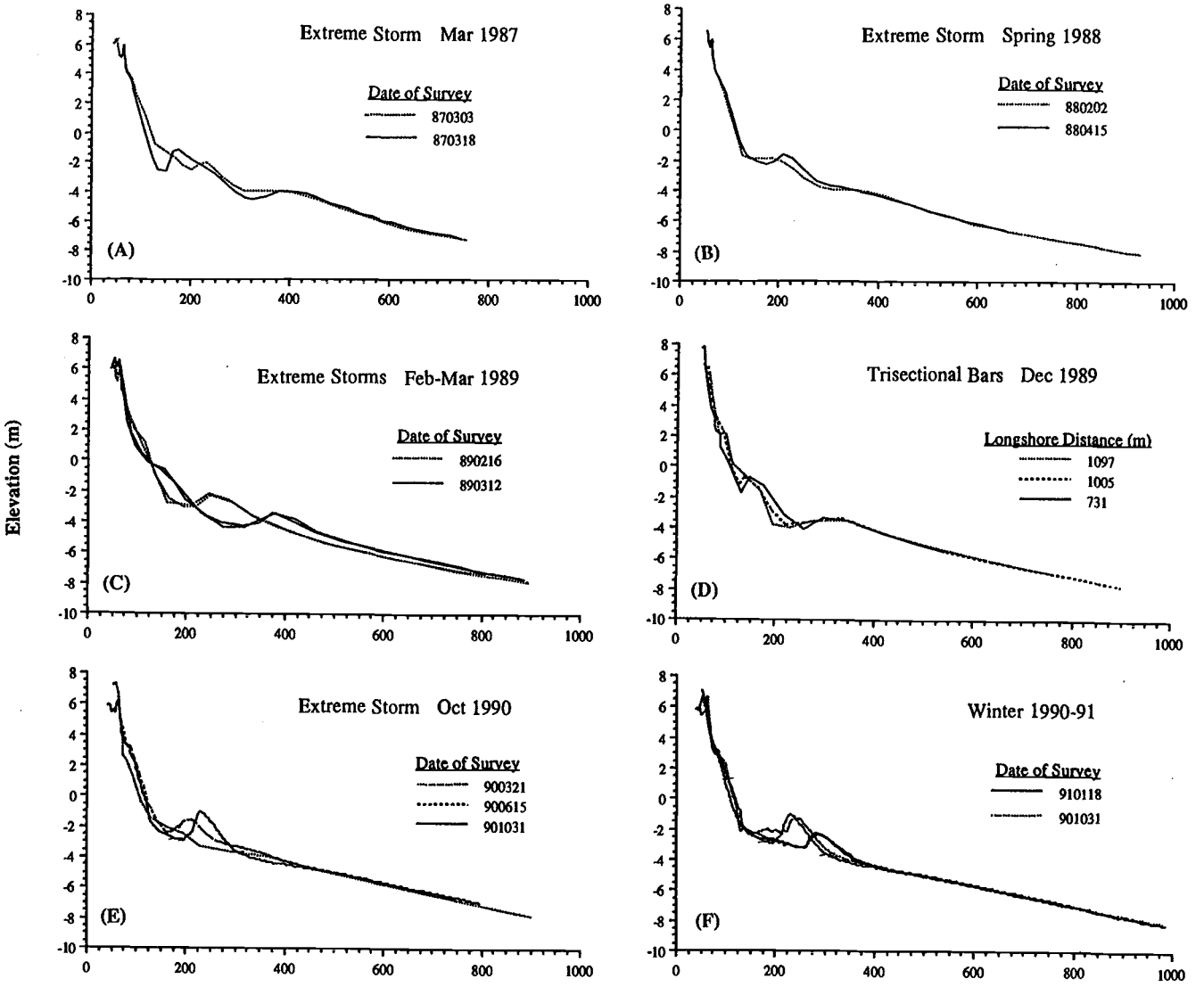
Extreme Storm Mar 1987
Date of Survey
870303
870318
(A)
Extreme Storm Spring 1988
Date of Survey
880202
880415
(B)
Extreme Storms Feb-Mar 1989
Date of Survey
890216
890312
(C)
Trisectional Bars Dec 1989
Longshore Distance (m)
1097
1005
731
(D)
Extreme Storm Oct 1990
Date of Survey
900321
900615
901031
(E)
Winter 1990-91
Date of Survey
910118
901031
(F)
Elevation (m)
Cross-shore Distance (m)

than observed during the preceding two years (Figure V.8). The disappearance of the outer bar apparently had important consequences to the behavior to the overall beach system under the more energetic wave climate in the following fall (Table V.2).

The timing of the next extreme event (February 1989) coincided with the absence of any outer bar, and resulted in further offshore migration of the single prominent bar as well as overtopping of the dune crest. Fortuitously a second, even more energetic extreme storm occurred approximately 10 days later (March 1989), at which time the prominent inner bar migrated yet further offshore and a new bar formed off the beach face (Figure V.8). CRAB surveys also reveal substantial effects from this storm beyond a water depth of 6 m (Figure V.11c).

The most significant change to the beach observed during the sequence of these closely spaced extreme storms was the formation of a new terrace-like bar near the shoreline. This new bar is observed in the video time exposure data to be consistent with "ridge and runnel" or "low-tide terrace" bars with incident wave scaling ($O(10^1$ m); see Wright and Short, 1984; LH90). The CRAB surveys clearly reveal this new distinct perturbation (Figure V.11c), and infers that the bar formed from sediment off the beach face (although this is not proven). This bar caused the previously discussed difficulty in uniquely identifying the same bar continuously through time. When wave height was too small to break over the more prominent seaward bar, the beach system appeared to consist of an incident scaled bar against the shoreline. Under a variable wave climate, the offshore bar is alternately revealed (under larger waves) and undetected (under smaller waves), making it appear to unrealistically migrate hundreds of meters in the cross-shore on a very short time scale, on the order of 1-2 days. This apparent "jumping" between different bars was successfully handled in the manner described earlier.

Over the next 6 months of lower waves (Table V.2; Figure V.6) the predominant bar migrated slowly shoreward and was reduced in amplitude (Figure V.8). The inner bar

near the shoreline remained in approximately the same cross-shore position. Although the passage of Hurricanes Gabrielle and Hugo in September 1989 had some effect on the innermost part of the profile, they did little to alter the overall configuration of the two bar system despite prolonged duration, particularly during Gabrielle waves (Table V.2). In fact, the relatively numerous moderate storms during the fall months did not greatly alter the monthly mean positions of either bar.

However, during the passage of the next extreme storm (December 1989) the inner bar at the shoreline migrated rapidly offshore to become the most prominent bar, and the previous prominent bar was reduced in amplitude to become more characteristic of previously observed outer bars (Figure V.8). This configuration of the bar system was similar to that observed during the first two years of the study period. Over the next 6 months the bar system retained this configuration, although the outer bar gradually decreased in amplitude and eventually became undetectable in CRAB surveys (Figure V.11e).

The last observed extreme wave event in October 1990 completely smoothed the offshore beach profile and removed any indication of an outer bar within 700 m of the shoreline (Figure V.11e). The offshore slope flattened and the profile was affected beyond water depths of 6 m. The single bar migrated offshore to a similar position as that observed in the winter of 1989 (~150 m offshore; Figure V.8). However, by November the bar had moved even further offshore and continued to migrate seaward (Figure V.8; Figure V.11f), remarkably similar to the behavior in early 1989. However, unlike the previous year, a second extreme storm immediately following did not occur. Instead, under the influence of the smaller storms and generally lower waves of the following spring and summer, the prominent single bar slowly migrated landward.

It is interesting to note that during the period of November-December 1989 the inner most bar appeared to be very similar in morphology to the "trisectional" bars observed by

Lester (1980; see also Birkemeier, *et al.*, 1985; Kroon, 1991; Howd and Birkemeier, in review). These bars are characterized by having a single shore attachment point at the proximal end, and then diverge at an angle away from the shoreline as the bar extends alongshore to the south. Figure V.12 clearly shows this bar behavior. Example CRAB surveys at three longshore distances spanning ~360 m also shows the southerly seaward trend of the bar (Figure V.11d). These bars appeared to have a shoreline attachment point just north of the study area, clearly seen in the video data. A separate bar originating much further to the north, appeared to form a somewhat continuous link with the now outer bar at the distal end. The significance of these bars in the transition of the beach system is not well understood. A detailed study of the topographical response to the wave climate (including incident wave angles and mean currents, for example), could provide insight into the formation and migrational behavior of these bars, and their role on the overall configuration of the beach system.

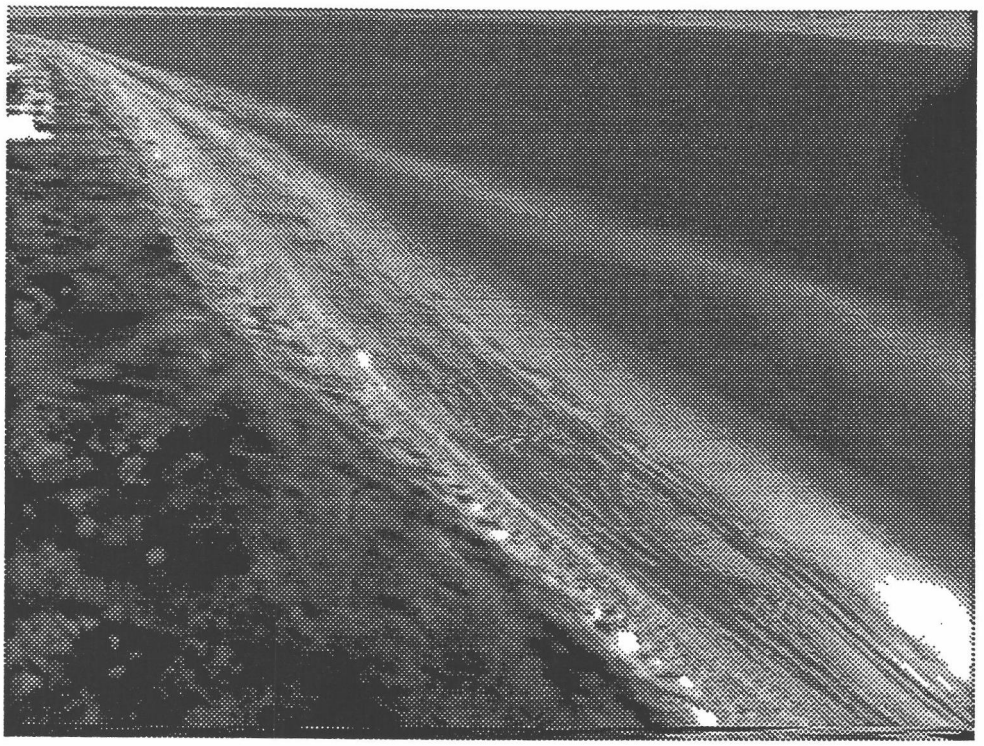

Figure V.12. Ten minute time exposure from 7 December 1989 showing the tri-sectional bars observed in the data. The bar has a shoreline attachment point in the upper part of the image (toward the north), and extends offshore at a angle away from the shoreline towards the south.

DISCUSSION

Previous concepts of seasonal patterns in cross-shore sediment transport were predicated on the general observation that during higher energy winter months sand is removed from the beach face (thereby narrowing the subaerial beach width) and deposited offshore in sand bars. During lower energy conditions (characteristic of summer months) sand transport is predominantly landward, resulting in sand migration from offshore to the beach face (widening the subaerial beach) and a smooth beach profile without offshore sand bars. Observations have confirmed the seasonal cycle in bar migration, represented by temporal changes in the mean offshore distance to the bar crest (*i.e.*, LH90). Although outer bars are not observed to migrate seasonally in the on-offshore direction, profile data indicate that the outer bar is generally reduced in amplitude during prolonged periods of low waves.

In contrast, field observations presented herein and in LH90 (among others) indicate that offshore sand bars do not completely go away during low energy months. In fact, we observe bars at all times throughout the year as either well defined trough-bar sequences or small amplitude low-tide terraces. Birkemeier (pers. comm, 1991) also has reported that only once in over ten years of profile data collection at the FRF has the offshore bathymetry been void of any perturbations, suggesting that the natural beach configuration of the FRF field site consists of one or more longshore sand bars.

Surprisingly, the beach width is observed to increase during higher energy months of fall, winter, and spring, and to narrow during lower energy months typical of summer conditions (although with a phase lag of 1-2 months). This could be an affect of the FRF pier interrupting the natural sediment transport. Miller, *et al.* (1984) show that, in fact, the pier does have a substantial influence on the sediment behavior, most pronounced in the vicinity of the pier pilings. Further from the pier the effect is reduced. A second

possibility is from the development of a low-tide terrace bar. Erosion in the upper reaches of the foreshore with deposition in the lower swash zone can produce an apparent reduction in total subaerial beach volume. This observation is the subject of ongoing research (Birkemeier, 1992, pers. comm.).

It should be noted that our definition of extreme storms is based empirically on observations of the incident wave climate during the study period. The criteria set as H_s exceeding 3 m is not necessarily the only choice. The 6 hour minimum criteria is simply chosen so as to exclude lesser energetic storms (on an integrated wave power basis) which have little or no affect on monthly averaged wave statistics. Choosing different criteria would result in a different relationship between defined extreme storms, initial profile configuration, and the response of the bar system. The criteria used in this study separate those storms which had the most profound affect on the overall bar system, and in hindsight serves our purpose well.

The absence of a perturbation in the offshore profile appears to play a key role in the behavior of the prominent inner bar, evident in the months just following extreme storms when the prominent bar usually migrates offshore. As suggested by Dally and Dean (1984), sand bars will move seaward under high waves (towards a dissipation maximum) provided that the duration of the storm is sufficient to allow the bar form to respond. They also imply that the lack of field evidence is due to the rapid rise and decline of typical storms (lasting 1-2 days) which prevents significant offshore migration, and in fact during this study even very large wave events of short duration (*i.e.*, Hurricane Bob in August 1991) did not alter the major characteristics of the offshore profile.

Bar response to incident wave forcing depends on the saturation condition. During storms when large waves are breaking over an existing outer bar, the wave field in the inner surf zone is saturated (*i.e.*, increasing H_s does not change wave height locally inside the break point), and the incident wave dissipation distribution over the bar does not

respond to increasing incident energy (Thornton and Guza, 1983; Lippmann and Holman, 1989; Holman and Sallenger, this volume). However, in the absence of an outer profile perturbation, dissipation distributions over a prominent (inner) bar are not limited seaward by saturation. Unfortunately, no scaling for bar position and shape are predicted by these models. On the other hand, infragravity waves (with much longer periods than incident waves) have length scales which match typical large scale morphologic features, have been linked to the formation and maintenance of the nearshore bars at Duck (Sallenger and Holman, 1987). Furthermore, infragravity waves are not limited in amplitude by breaking, and thus can dominate sea surface elevation and velocity spectra in the inner surf zone during storms (*e.g.*, Thornton and Guza, 1982), an important observation since this is when sediment movement is greatest and the largest changes to the beach system occur. Comparisons of the leading (and sometimes competing) models of bar generation are discussed further in the companion paper (Holman and Sallenger, this volume).

Temporal variations in the overall bar system are characterized by rapid transition between one and two bar configurations. These transitions result in marked interannual variability, and indicate that the bar system is nonstationary over the 5 year study. Profile response to wave forcing also depends on the presence or absence of an outer bar. During periods when the outer bar is present, the inner bar behaves in a regular (*i.e.*, seasonal), predictable manner. When the outer bar is absent the inner bar is not as well behaved. Additionally, the presence of sand bars has a significant influence on the incident wave field (and also on infragravity waves; Kirby, *et al.*, 1981), shown clearly by observed wave breaking patterns in videos (LH89) and wave height distributions in the surf zone (Thornton and Guza, 1983). This feed back mechanism between the topography and the wave field, coupled with the sensitivity of the bar system response to the initial bathymetry, suggests that the bar system has characteristics of a nonlinear dynamical system.

Similar behavior of the two bar system at the FRF has also been observed previously by Birkemeier (1984). Using similar biweekly beach profile surveys they tracked the crest position of both the inner and outer bars over a 3.5 year period (from February 1981 through July 1984). That data indicate that during the winter immediately following the disappearance of the outer bar (in March 1981), the predominant inner bar moved offshore and a new bar formed off the beach face (Figure V.13), very similar to our observations in March 1989 (Figure V.8). The following year, in the more energetic fall and winter months, both the new bar and the prominent seaward bar migrated seaward to their previously observed locations, also similar to our observations in December 1989 (Figure V.8). This apparent repeatable behavior suggests that the transition from 1-2 bar configuration may be a characteristic low frequency cycle of the Duck beach system.

The occurrence of the tri-sectional bars (mentioned earlier and seen previously by Lester, 1980) may also play some role in the transitional behavior of the system. Although it is not clear from the data, longshore migrating oblique bars could account for apparent transitions between one and two bar configuration, an observation well documented on the Dutch coast (see Kroon, 1991). We do not understand this behavior well enough to comment on further implications of these oblique bars.

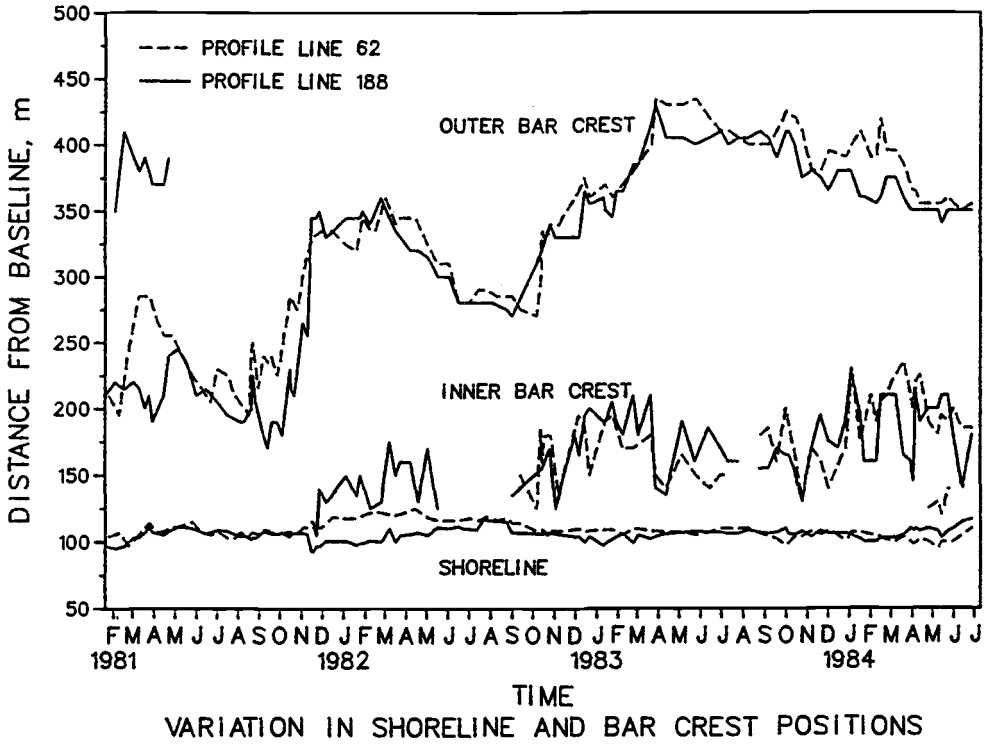

Figure V.13. Variations in shoreline and bar crest positions estimated from beach profiles, February 1981 through July 1984 (from Birkemeier, 1984). The behavior of the bar system is similar as that observed in this study (Figure V.8).

CONCLUSIONS

The behavior of a naturally occurring sand bar system consisting of 1-2 longshore bars is observed over a 5 year period. The data are collected at the Army Corps of Engineers Field Research Facility (FRF), in Duck, N.C., USA. The inner bar is sampled using the video time exposure methods of Lippmann and Holman (1989a), and allows for a quantitative time series evaluation of bar shape and distance from the shoreline on a daily basis (provided waves are large enough to break over the shallows of the crest) over a 400 m length of beach. Biweekly beach profile surveys are used to identify the approximate position of any outer bars and to fill in extended gaps in the video record. A working definition of inner and outer bars is used in which bars are considered inner if they are located equal to or landward of the most prominent bar (in terms of crest-trough amplitude), and where outer bars are any significant profile perturbations seaward of the most prominent bar.

Yearly averages of inner bar statistics (means and standard deviations) for each alongshore location are computed to assess homogeneity and stationarity. Yearly statistics show the prominent inner bars are homogeneous over the length of the array. However, substantial interannual variability in the cross-shore means and standard deviations imply that overall bar behavior is nonstationary over the 5 year study period. Short-term bar behavior is addressed from the time series of bar position analyzed on a monthly-averaged basis, in which the daily mean bar position statistics are computed first over the length of the array (400 m) and secondly on a monthly time scale.

The time series of monthly averaged statistics reveals episodic transitions between one and two bar configurations, and is shown to contribute significantly to the nonstationary behavior of the bar system. Associated with these transitions is the timing of extreme wave events (defined here as when offshore significant wave height exceeds 3

m for over 6 consecutive hours) with the presence or absence of any outer bar. The influence of extreme waves (without consideration of directional distribution) depends heavily on the offshore profile characteristics, and usually results in both immediate alterations of bar configuration and subsequent monthly averaged migration patterns. In general, without the presence of an outer bar, the inner bar is observed to migrate further seaward (under typical storm events) than when a well defined outer bar exists.

Characteristic responses under extreme storms include smoothing and flattening of the offshore profile and slope, with substantial sediment deposition at depths greater than 4 m. During four of the six observed extreme storms the outer profile was significantly altered and the inner bar underwent extensive seaward migration. Interestingly, on one occasion when the outer bar was well defined the offshore profile was only altered slightly, and the outer bar amplitude became more pronounced, suggesting that the amplitude of the outer bar has a decisive influence on the response of the beach profile.

The most dramatic change to the bar system resulted from the succession of two very extreme storms within a 10 day period, at which time a single (only) prominent bar migrated offshore and shortly thereafter became the outer bar as a new bar formed off the beach face. Previous data from this beach system (Birkemeier, 1984) are also consistent with observations in this study, and suggest that the transition from 1 to 2 bar configuration is characteristic of the Duck field site.

ACKNOWLEDGEMENTS

The video data were collected by the dedicated FRF staff under the guidance of Bill Birkemeier. The survey and wave data were also collected by the FRF as part of their ongoing data collection program. Without their conscientious efforts this work would not have been possible. Special appreciation is extended to Zach del Nero, who spent many hours creatively digitizing time exposure images, gathering wave statistics, and generally aiding in the processing of the data. This paper benefited from insightful discussions with Bill Birkemeier, Peter Howd, and Todd Holland and from comments by the reviewers. Funding for this project was provided by the Office of Naval Research, Coastal Sciences Program, under contract N00014-90-J1118, and by the U.S. Army Corps of Engineers, Coastal Engineering Research Center under the Barrier Island Sedimentation work unit.

GENERAL CONCLUSIONS

This work focuses on the direct forcing of infragravity motions by the spatial distribution (gradient) of the time variation in incident wave break point amplitudes. Theoretical forcing mechanisms are suggested, and estimates are made of the spatial and temporal scales of incident wave break point positions, a first order proxy of the forcing.

A theoretical forcing mechanism for driving resonant, longshore progressive wave motions at low frequencies (edge waves) is derived from the momentum balance equations. The non-linear forcing is provided by the unbalanced gradient in radiation stress induced by two discrete interacting incident waves (in both frequency and direction, and thus longshore wavenumber), and includes consideration of the longshore contributions in momentum flux. The strength of this mechanism is found to be comparable to offshore forcing proposed by Gallagher (1971), who intentionally excluded forcing due to breaking phenomena. Thus, the surf zone component of the forcing can not be neglected, and under the right conditions can actually dominate. The total forcing, including both offshore and surf zone contributions, introduces structure into the infragravity band of the forcing spectra, and with restrictions introduced by discrete resonances of the system, provides a frequency selection mechanism necessary for generation of nearshore sand bars. Growth rates are predicted and found to be quite rapid, much faster than other model predictions (Foda and Mei, 1981), although the stochastic nature of real ocean waves (non-resonant forcing) will reduce these rates.

The time and space scales of wave breaking are investigated using a new video based technique. The technique relies on the visual contrast difference between the lighter foam and bubbles of actively breaking waves and bores, and the darker non-breaking surrounding water. Raw data is in the form of video tapes of the surf zone. Digital data is obtained and quantified using an image processing system during real time play back of the tapes. Image intensity is digitized (by an image processor) at 2-10

Hz at known ground locations. Time series are sampled at numerous known locations simultaneously, from outside the maximum break point, across the forcing region, well into the saturated inner surf zone. Large arrays span several hundred meters in both the cross-shore and longshore directions.

The field data were collected as part of the DELILAH nearshore processes experiment at the U.S. Army Corps of Engineers Field Research Facility located on the Outer Banks of N. C., near the village of Duck, in October 1990. Video time series data were obtained with two cameras, each looking over a different region of the surf zone. Other measurements include shoreline runup (digitized from video tapes), a cross-shore array of co-located current meters and bottom mounted pressure sensors, and two longshore arrays of current meters located in the trough and on the seaward flank of the bar.

Image intensity time series accurately measure the spatial and temporal relationship (*i.e.*, phase and coherence) of wave breaking processes over potentially large areas of interest. Time domain analysis of individual breaking wave statistics are accomplished and presented in terms of phase speeds and wave angles. At incident scales, principal results indicate that the important breaking processes, in terms of temporal and spatial phase, can be quantified. The analysis of this part of the research follows two lines. The first focuses on the time series of image intensity at points corresponding to known surf zone locations, and comparisons with sea surface elevation. Celerity spectra of video and pressure data from a single location show similar results. Wavenumber spectra at the peak frequency from two longshore arrays of intensity time series compares favorably with similarly spaced current meter data. Mean values of phase speeds and wave angles are consistent with first order shoaling theory.

The time and space scales of wave breaking modulations are estimated and compared with the free infragravity wave response across the surf zone. Large arrays of

image intensity span several hundred meters in both the cross-shore and alongshore directions. At low frequencies, breaking wave distributions seaward of the bar crest are associated with wave groups progressing landward at the phase speed of the incident waves. Analysis of longshore length scales indicate group forcing to be broad-banded across frequency-wavenumber space. Interestingly, no coherence was found between group forcing and the infragravity free wave response, suggestion that the nearshore is a high Q (resonant system).

Furthermore, we observe the group structure in the wave field to be greatly reduced by breaking in the inner surf zone. All initiation of breaking occurs seaward of the crest, with generally larger waves breaking further offshore and a higher percentage of breaking waves in progressively shallower depths. This suggests that surf zone forcing models which assume a depth dependence on breaking amplitude are more in keeping with the data. Furthermore, breaking does not cease at the point of minimum depth at the crest, and in fact is widespread in the trough of the bar. This suggests that lateral mixing of momentum across the surf zone, due to the time-lagged dissipation of incident wave energy, could be important in modeling longshore currents.

The final chapter of the thesis deals with the behavior of large scale sand bar evolution, and is a continued investigation of the long time series of bar position at the Duck beach analyzed by Lippmann and Holman (1990). The influence of a possible outer bar on the behavior of a very dynamic inner bar is examined. The data set of Lippmann and Holman (1990) is extended to five years, with the analysis focusing on the monthly mean cross-shore position of both the prominent inner bar and the more subtle offshore bar. Daily changes in bar position and shape are not addressed (as in Lippmann and Holman, 1990), but rather the general behavior of the monthly averaged bar position and integrated variability is investigated. Analysis is focused on temporal stationarity and with regard to the presence or absence of an outer bar. Episodic transitions between 1 and 2 bar configuration occurs when the timing of extreme wave

events coincides with a reduced or non-existent outer bar. The influence of extreme storms depends heavily on the profile characteristics and usually results in both immediate alterations to the beach profile and subsequent monthly averaged bar migration patterns. Previous results from similar analysis by Birkemeier (1984) suggest that the transition from 1 to 2 bar configuration at the Duck field site is a natural progression.

REFERENCES

Abramowitz, M. and I. A. Stegun, Handbook of Mathematical Functions, Dover Publications, Inc., New York, 1046 pp., 1965.

Bagnold, R. A., Mechanics of Marine Sedimentation, in The Sea, M. N. Hill (ed.), Wiley-Interscience, New York, 507-582, 1963.

Bendat, J. S. and A. G. Piersol, Random data analysis and measurement procedures, 2nd ed., Wiley-Interscience, New York, pp. 118-140, 1986.

Birkemeier, W. A., C. Mason, The CRAB: A unique nearshore surveying vehicle, *J. Surv. Eng.*, 110(1), 1-7, 1984.

Birkemeier, W. A., Time scales of nearshore profile change, in *Proceedings of the 19th Conference on Coastal Engineering*, American Society of Civil Engineers, New York, 1507-1521, 1985.

Birkemeier, W. A., H. C. Miller, S. D. Wilhelm, A. E. DeWall, and C. S. Gorbics, User's guide to CERC's Field Research Facility, Instruction Report-85-1, Coastal Eng. Res. Cent., Field Res. Facil., U. S. Army Eng. Waterw. Exp. Sta., Vicksburg, Miss., 1985.

Birkemeier, W. A., C. F. Baron, M. W. Leffler, H. C. Miller, J. B. Strider, and K. K. Hathaway, SUPERDUCK nearshore processes experiment: Data summary, *Miscellaneous reports, Coastal Engineering Research Center, Field Research Facility*, U.S. Army Eng. Waterways Experiment Station, Vicksburg, Miss., 1989

Birkemeier, W. A., DELILAH nearshore processes experiment: Data summary, *miscellaneous reports*, Coastal Eng. Res. Cent., Field Res. Facil., U. S. Army Eng. Waterw. Exp. Sta., Vicksburg, Miss., 1991.

Bowen, A. J., D. L. Inman and V. P. Simmons, Wave 'set-down' and set-up, *J. Geophys. Res.*, 73, 2569-2577, 1968.

Bowen, A. J. and D. L. Inman, Edge waves and Crescentic bars, *J. Geophys. Res.*, 76, 8662-8671, 1971.

Bowen, A. J., and R. T. Guza, Edge waves and surf beat, *J. Geophys. Res.*, 83, 1913-1920, 1978.

Bowen, A. J., Simple models of nearshore sedimentation: Beach profiles and longshore bars, in Coastline of Canada, Littoral Processes and Shore Morphology, *Geol. Surv. Can. Pap., 80-10*, 1-11, 1980.

Bowen, A. J., and D. A. Huntley, Waves, long waves and nearshore morphology, *Mar. Geol.*, 60, pp. 1-13, 1984.

Bowen, A. J., and R. A. Holman, Instabilities of the mean longshore current 1. Theory, *J. Geophys. Res.*, 94(C12), 18023-18030, 1989.

Bowen, A. J., and A. S. Ngusaru, Longshore currents on a multi-barred beach, Abstract O31E-6, *Trans. Amer. Geophys. Union*, 72(44), 253, 1991.

Church, J. C., and E. B. Thornton, Modeling strong longshore currents, Abstract O31E-5, *Trans. Amer. Geophys. Union*, 72(44), 253, 1991.

Dally, W. R., and Dean, R. G., Suspended sediment transport and beach profile evolution, *J. Waterw., Port, Coast., and Ocean Eng.*, 110, pp. 15-33, 1984.

Davis, R. E., and L. Regier, Methods for estimating directional wave spectra from multi-element arrays, *J. Mar. Res.*, 35, 453-477, 1977.

Dodd, N., and E. B. Thornton, Growth and energetics of shear waves in the nearshore, *J. Geophys. Res.*, 95, 16,075-16,083, 1990.

Dodd, N., J. M. Oltman-Shay, and E. B. Thornton, Shear Instabilities in the longshore current: A comparison of observation and theory, *J. Phys. Oceanogra.*, 22, 62-82, 1992.

Dhyr-Nielsen, M., and T. Sorensen, Sand transport phenomena on coasts with bars, in *Proceedings of the 12th International Conference on Coastal Engineering*, American Society of Civil Engineers, New York, 855-866, 1970.

Eckart, C., Surface waves on water of variable depth, *Wave Rep. 100*, Scripps Inst. of Oceanogra., Univ. of Calif., La Jolla, 1951.

Elgar, S., and R. T. Guza, Observations of bispectra of shoaling surface gravity waves, *J. Fluid Mech.*, 161, 425-448, 1985a.

Elgar, S., and R. T. Guza, Shoaling gravity waves: comparisons between field observations, linear theory, and a nonlinear model, *J. Fluid Mech.*, 158, 47-70, 1985b.

Elgar, S, and R. T. Guza, Statistics of bicoherence, *IEEE Transactions on Acoustics, Speech, and Signal Processing*, 36(10), 1667-1668, 1988.

Elgar, S., T. H. C. Herbers, M. Okihiro, J. M. Oltman-Shay, and R. T. Guza, Observations of infragravity waves, *J. Geophys. Res.*, in press, 1992.

Foda, M. A. and C. C. Mei, Nonlinear excitation of long-trapped waves by a group of short swells, *J. Fluid Mech.*, 111, 319-345, 1981.

Fowler, R. E., and R. A. Dalrymple, Wave group forced nearshore circulation, in *Proceedings of the 22nd International Conference on Coastal Engineering*, American Society of Civil Engineers, New York, 1-14, 1990.

Gallagher, B., Generation of surf beat by nonlinear wave interactions, *J. Fluid Mech.*, 49, 1-20, 1971.

Goldsmith, V., D. Bowman, and K. Kiley, Sequential Stage development of crescentic bars: Hohaterim beach, Southeastern Mediterranean, *J. Sed. Petrol.*, 52, pp. 233-249, 1982.

Greenwood, B., and R. G. D. Davidson-Arnott, Marine bars and nearshore sedimentary processes, Kouchibouguac Bay, New Brunswick, Canada, in Nearshore Sediment Dynamics and Sedimentation, John Wiley, New York, 123-150, 1979.

Guza, R. T. and E. B. Thornton, Swash oscillations on a natural beach, *J. Geophys. Res.*, 87(C1), 483-491, 1982.

Guza, R. T., E. B. Thornton, and R. A. Holman, Swash on steep and shallow beaches, *Proceedings of the 19th International Conference on Coastal Engineering*, American Society of Civil Engineers, New York, 708-723, 1984.

Guza, R. T., and E. B. Thornton, Observations of surf beat, *J. Geophys. Res.*, 90, 3161-3172, 1985.

Haines, J. W., and A. J. Bowen, Phase-locking of modes in the nearshore: Field evidence, in *Proceedings of the 21st International Conference on Coastal Engineering*, American Society of Civil Engineers, New York, 1522-1534, 1988

Harris, F. J., On the use of windows for harmonic analysis with the discrete Fourier transform, *Proceedings of the IEEE*, 66(1), 51-83, 1978.

Hasselmann, K., On the non-linear energy transfer in a gravity-wave spectrum. 1. General theory, *J. Fluid Mech.*, 12, 481-500, 1962.

Haubrich, R., Earth noises, 5 to 500 millicycles per second, 1, *J. Geophys. Res.*, 70, 1415-1427, 1965.

Herbers, T. H. C., and R. T. Guza, Wind-wave nonlinearity observed at the sea floor. Part 1: Forced-wave energy, *J. Phys. Oceanogra.*, 21, 1740-1761, 1991.

Herbers, T. H. C., and R. T. Guza, Wind-wave nonlinearity observed at the sea floor. Part II: wavenumbers and third-order statistics, *J. Phys. Oceanogra.*, 22, pp. 489-504, 1992.

Holland, K. T., and R. A. Holman, The distribution of swash maxima, *J. Geophys. Res.*, in press, 1992.

Holman, R. A., Infragravity energy in the surf zone, *J. Geophys. Res.*, 86(C7), 6442-6450, 1981.

Holman, R. A. and A. J. Bowen, Bars, bumps, and holes: Models for the generation of complex beach topography, *J. Geophys. Res.*, 87(C1), 457-468, 1982.

Holman, R. A., and A. J. Bowen, Longshore structure of infragravity wave motions, *J. Geophys. Res.*, 89(C4), 6446-6452, 1984.

Holman, R. A., and A. H. Sallenger, Setup and swash on a natural beach, *J. Geophys. Res.*, 90(C1), 945-953, 1985.

Holman, R. A., P. A. Howd, J. M. Oltman-Shay, and P. D. Komar, Observations of swash expression of far infragravity wave motions, in *Proceedings of the 22nd International Conference on Coastal Engineering*, American Society of Civil Engineers, New York, 1242-1253, 1990.

Holman, R. A. and A. H. Sallenger, Sand bar generation: A discussion of the Duck experiment series, *J. Coastal Res., Special Issue*, in press, 1992.

Howd, P. A., J. M. Oltman-Shay, and R. A. Holman, Wave variance partitioning in the trough of a barred beach, *J. Geophys. Res.*, 96, 12781-12795, 1991.

Howd, P. A., A. J. Bowen, and R. A. Holman, Edge waves in the presence of strong longshore currents, *J. Geophys. Res.*, 97(C7), 11357-11371, 1992.

Howd, P. A., and W. A. Birkemeier, Long term measurements of beach and nearshore profiles. 1. Envelop and time scales of change, *Coastal Eng.*, in review.

Huntley, D. A., Long period waves on a natural beach, *J. Geophys. Res..*, 8, 6441-6449, 1976.

Huntley, D. A., R. T. Guza, and E. B. Thornton, Field observations of surf beats. 1. Progressive edge waves, *J. Geophys. Res.*, 86(C7), 6451-6466, 1981.

Huntley, D. A., and C. S. Kim, Is surf beat forced or free?, in *Proceedings of the 19th International Conference on Coastal Engineering*, American Society of Civil Engineers, New York, 77-92, 1984.

Huntley, D. A., Evidence for phase coupling between edge wave modes, *J. Geophys. Res.*, 93(C10), 12393-12408, 1988.

Katoh, K., Analysis of edge waves by means of empirical eigenfunctions, *Report of the Port and Harbor Institute*, 20, 3-51, 1981.

Kim, Y. C., and E. J. Powers, Digital bispectral analysis and its applications to nonlinear wave interactions, *IEEE Trans. Plasma Sci.*, PS-7(2), 120-131, 1979.

Kirby, J. T., R. A. Dalrymple, and P. L.-F. Liu, Modification of edge waves by barred beach topography, *Coastal Engineering*, 5, 35-49, 1981.

Komar, P. D., and D. L. Inman, Longshore sand transport on beaches, *J. Geophys. Res.*, 75, 5514-5527, 1970.

Komar, P. D., Littoral sediment transport, in Handbook of Coastal and Ocean Engineering, John B. Herbich (ed.), 2, 681-714, 1991.

Kroon, A., Three dimensional morphological changes of a nearshore bar system along the Dutch coast near Egmond Aan Zee, In *Proceedings of the Skagen Symposium, Journal of Coastal Research, Special Issue No. 9*, CERF, 430-451, 1991.

Lester, M. E., Aerial investigation of longshore bars along the Outer Banks of North Carolina, U.S. Army Corps of Engineers, Coastal Engineering Research Center, Fort Belvoir, Va., unpublished, 1980.

Lippmann, T. C., and R. A. Holman, Quantification of sand bar morphology: A video technique based on wave dissipation, *J. Geophys. Res.*, 94, 995-1011, 1989a.

Lippmann, T. C., and R. A. Holman, Quantitative estimation of incident wave dissipation from observations of surf zone wave breaking, Abstract O11D-10, *Trans. Amer. Geophys. Union*, 71(73), 1355, 1989b.

Lippmann, T. C., and R. A. Holman, Phase speed and angle of breaking waves measured with video techniques, in *Proceedings of Coastal Sediments '91 Specialty Conference*, American Society of Civil Engineers, New York, 542-556, 1991.

Lippmann, T. C. and R. A. Holman, The spatial and temporal variability of sand bar morphology, *J. Geophys. Res.*, 95(C7), 11575-11590, 1990.

List, J. H., Wave groupiness as a source of nearshore long waves, in *Proceedings of the 20th Conference on Coastal Engineering*, American Society of Civil Engineers, New York, 497-511, 1987.

List, J. H., Wave groupiness variations in the nearshore, *Coastal Eng.*, 15, 475-496, 1991.

List, J. H., A model for the generation of two-dimensional surf beat, *J. Geophys. Res.*, 97(C7), 5623-5635, 1992.

Long, C. E., and J. M. Oltman-Shay, Directional characteristics of waves in shallow water, Technical Report CERC-91-, Coastal Eng. Res. Cent., Field Res. Facil., U. S. Army Eng. Waterw. Exp. Sta., Vicksburg, Miss., 1991.

Longuet-Higgins, M. S. and R. W. Stewart, Radiation stresses and mass transport in gravity waves, with application to 'surf beats', J. *Fluid Mech.*, 13, 481-504, 1962.

Longuet-Higgins, M. S. and R. W. Stewart, Radiation stresses in water waves: A physical discussion, with applications, *Deep Sea Res.*, 11, 529-562, 1964.

Mei, C. C., The applied dynamics of ocean surface waves, John Wiley, pp. , 1983.

Miche, R., Mouvements ondulatoires des mers en profondeur constante ou decroissante, Univ. Calif. at Berkeley, Wave Res. Lab., *Ser. 3*, Issue 363, 1954.

Miller, H. C, W. A. Birkemeier, and A. E. DeWall, Effects of CERC research pier on nearshore processes, in *Proceedings of the International Conference on Coastal Structures '83*, American Society of Civil Engineers, New York, 765-782, 1983.

Munk, W. H., Surf beats, *Eos Trans. AGU*, 30, 849-854, 1949.

Okihiro, M., R. T. Guza, and R. J. Seymour, Bound infragravity waves, *J. Geophys. Res.*, 97(C7), 11473-11469, 1992.

Olbers, D. J., and K. Herterich, The spectral energy transfer from surface waves to internal waves, *J. Fluid Mech.*, 92, 349-379, 1979.

Oltman-Shay, J. M., and R. T. Guza, A data-adaptive ocean wave directional-spectrum estimator for pitch and roll type measurements, *J. Phys. Oceanogra.*, 14,1800-1810, 1984.

Oltman-Shay, J. M., and R. T. Guza, Infragravity edge wave observations on two California beaches, *J. Phys. Oceanogra.*, 17(5), 644-663, 1987.

Oltman-Shay, J. M., P. A. Howd, and W. A. Birkemeier, Instabilities of the mean longshore current, 1. Field observations, *J. Geophys. Res.*, 94(C12), 18031-18042, 1989.

Pawka, S. S., Island shadows in wave directional spectra, *J. Geophys. Res.*, 88, 2579-2591, 1983.

Phillips, O. M., The Dynamics of the Upper Ocean, 2nd Ed., Cambridge Univ. Press., pp. 336, 1977.

Priesendorfer, R. W., F. W. Zwiers, and T. P. Barnett, Foundations of principal component selection rules, *SIO Rep. 81-4*, Scripps Inst. of Oceanogra., La Jolla, Calif., 200 pp., 1981.

Putrevu, U., and I. A. Svendsen, Nearshore mixing due to the interaction of the undertow and longshore currents, Abstract O31E-9, *Trans. Amer. Geophys. Union*, 72(44), 253-254, 1991.

Putrevu, U., and I. A. Svendsen, Shear instability of longshore currents: A numerical study, *J. Geophys. Res.*, 97(C5), 7283-7303, 1992.

Roelvink, J. A., and M. J. F. Stive, Bar-generating cross-shore flow mechanisms on a beach, *J. Geophys. Res.*, 94(C4), 4785-4800, 1989.

Sallenger, A. H., R. A. Holman, and W. A. Birkemeier, Storm induced response of a nearshore bar system, *Mar. Geol.*, 64, 237-257, 1985.

Sallenger, A. H., and R. A. Holman, Wave energy saturation on a natural beach of variable slope, *J. Geophys. Res.*, 90(C6), 11939-11944, 1985.

Sallenger, A. H., and R. A. Holman, Infragravity waves over a natural barred profile, *J. Geophys. Res.*, 92(C9), 9531-9540, 1987.

Schaffer, H. A. and I. Svendsen, Surf beat generation on a mild-slope beach, in *Proceedings of the 21st International Conference on Coastal Engineering*, American Society of Civil Engineers, New York, 1058-1072, 1988.

Schaffer, H. A., Infragravity water waves induced by short-wave groups, *Ph.D. Thesis*, Instit. of Hydro. and Hydraulic Eng., Tech. U. of Denmark, Lyngby, 167 pp., 1990.

Shemer, L., N. Dodd, and E. B. Thornton, Slow-time modulation of finite-depth nonlinear water waves: Relation to longshore current oscillations, *J. Geophys. Res.*, 96(C4), 7105-7113, 1991.

Short, A. D., Three-dimensional beach stage model, *J. Geol.*, 87, 553-571, 1979.

Stoker, J. J., Surface waves in water of variable depth, *Quarterly of Applied Mathematics*, 5(1), 1-54, 1947.

Suhayda, J. N., Standing waves on beaches, *J. Geophys. Res.*, 79(21), 3065-3071, 1974.

Sunamura, T., Beach morphologies and their change, in *Nearshore Dynamics and coastal Processes: Theory, Measurement, and Predictive Models*, Horikawa, K. (ed.), University of Tokyo Press, Tokyo, 136-152, 1988.

Symonds, G., D. A. Huntley, and A. J. Bowen, Two-dimensional surf beat: long wave generation by a time-varying breakpoint, *J. Geophys. Res.*, 87, 492-498, 1982.

Symonds, G., and A. J. Bowen, Interactions of nearshore bars with incoming wave groups, *J. Geophys. Res.*, 89, 1953-1959, 1984.

Thornton, E. B., and R. T. Guza, Energy saturation and phase speeds measured on a natural beach, *J. Geophys. Res.*, 87(C12), 9499-9508, 1982.

Thornton, E. B., and R. T. Guza, Transformation of wave height distribution, *J. Geophys. Res.*, 88, 5925-5938, 1983.

Thornton, E. B., and R. T. Guza, Surf zone currents and random waves: Field data and models, *J. Phys. Oceanogra.*, 16, 1165-1178, 1986.

Tucker, M. J., Surf beats: Sea waves of 1 to 5 minute period, *Proc. R. Soc. A*, 202, 565-573, 1950.

Ursell, F., Edge waves on a sloping beach, *Proc. Royal Soc. A*, 214, 79-97, 1952.

Wallace, J. M., and R. E. Dickinson, Empirical orthogonal representation of time series in the frequency domain. Part I: Theoretical considerations, *J. Applied Meteor.*, 11(6), 887-892, 1972.

Watson, K. M., B. J. West, and B. I. Cohen, Coupling of surface and internal gravity waves: a mode coupling model, *J. Fluid Mech.*, 77, 105-208, 1976.

Whitford, D. J., and E. B. Thornton, Longshore current forcing at a barred beach, in *Proceedings of the 21st International Conference on Coastal Engineering*, American Society of Civil Engineers, New York, 77-90, 1988.

Wright, L. D., and A. D. Short, Morphodynamic variability of surf zones and beaches: A synthesis, *Mar. Geol.*, 56, 93-118, 1984.

APPENDIX

APPENDIX A:

DERIVATION OF THE OSCILLATING BREAKER POSITIONS

In this section we derive Eq. II.37, which defines the position of the oscillating breaker line through time and space. Take two waves approaching the beach at an angle, α_1 and α_2. Their sea surface displacement is given by the linear superposition of the two waves,

$$\eta = a_1 \cos(k_1 x + l_1 y - \sigma_1 t) + a_2 \cos(k_2 x + l_2 y - \sigma_2 t + \theta) \tag{A1}$$

where k_i and l_i are the cross-shore and alongshore components of the incident wave wavenumber vector, $\mathbf{k}$, such that $k_i = \mathbf{k}\cos\alpha_i$ and $l_i = \mathbf{k}\sin\alpha_i$, and θ is the phase relationship (fixed) of the two waves. We assume that $a_1 >> a_2$ (as in Eq. II.30), so that a_1 and a_2 are approximately constant near the break point region. We also assume that the primary wave, with amplitude a_1, breaks at its crest, hence

$$\eta|_{\text{breaking}} = a_1 + a_2 \cos(k_2 x + l_2 y - \sigma_2 t + \theta) \tag{A2}$$

We further assume that at breaking (II.29) holds so that

$$\frac{\gamma\beta x_b}{2} = a_1 + a_2 \cos(k_2 x_b + l_2 y - \sigma_2 t + \theta) \tag{A3}$$

If we follow the primary wave down the beach the longshore phase velocity is constant and given by

$$l_1 y - \sigma_1 t = \phi \tag{A4}$$

Substituting (A4) into (A1) yields

$$\eta = a_1 \cos(k_1 x + \phi) + a_2 \cos(k_2 x + (l_2 - l_1)y - (\sigma_2 - \sigma_1)t + \theta + \phi) \tag{A5}$$

after adding and subtracting ϕ in the cosine argument of the second wave term. Waves now break when $(k_1 x + \phi) = 0, 2\pi, \ldots$, hence the break point along the beach is given by

$$\frac{\gamma\beta x_b}{2} = a_1 + a_2 \cos\left((k_2 - k_1)x_b + (l_2 - l_1)y - (\sigma_2 - \sigma_1)t + \theta\right) \tag{A6}$$

Clearly the breaker amplitude varies from

$$a_1 + a_2 \le \eta|_{\text{breaking}} \le a_1 - a_2 \tag{A7}$$

This low frequency oscillation has mean value a_1, hence the mean breaker position, $\overline{x_b}$, is given by

$$a_1 = \frac{\gamma\beta\overline{x_b}}{2} \tag{A8}$$

Putting (A8) into (A6) and solving for $\overline{x_b}$ yields an expression for the oscillating breakpoint position

$$x_b = \overline{x_b} + x'_b \cos\left((k_2 - k_1)x_b - \psi_e + \theta\right) \tag{A9}$$

where $(l_2 - l_1)y - (\sigma_2 - \sigma_1)t = -k_e y + \sigma_e t = -\psi_e$ and $x'_b = 2a_2/\gamma\beta$. Eq. A9 is a transcendental function in which $x_b = f(x_b)$. If we expand (A9) in a Taylor series, it can be readily shown that x_b can be written as a fundamental, $\cos(f(x_b))$, plus harmonics, $\cos(mf(x_b) + \nu)$, where $m > 0$ is an integer and ν is the phase relationship of the harmonics to the primary. Thus to lowest order (A9) can be written

$$x_b = \overline{x_b} + x'_b \cos\left(\overline{(k_2 - k_1)x_b} - \psi_e + \theta\right) \tag{A10}$$

Incorporating θ into the first term in the argument of (A10) and substituting $x'_b = \delta\overline{X_b}$, the lowest order expression for the position of the oscillating breaker position is given by

$$x_b = \overline{x_b}\left(1 + \delta\cos\left(\frac{1}{2}\overline{X_e} + \psi_e\right)\right) \tag{A11}$$

which is Eq. II.37 in the main text.